Nonlinear Optics
of Metallic Photonic Crystal Slabs
and Planar Metamaterials

Zur Erlangung des akademischen Grades eines
Doktors der Naturwissenschaften
von der Fakultät für Physik der
Universität Karlsruhe (TH)

genehmigte

Dissertation

von

Diplom-Physiker Matthias W. Klein
aus Mainz

Publications

Parts of this thesis have already been published:

<u>In scientific journals:</u>

- M. W. Klein, M. Wegener, N. Feth, and S. Linden, *Experiments on second- and third-harmonic generation from magnetic metamaterials*, invited paper, Opt. Ex. (Focus Serial on *Frontiers of Nonlinear Optics*), submitted (2007).

- S. Linden, C. Enkrich, G. Dolling, M. W. Klein, J. F. Zhou, T. Koschny, C. M. Soukoulis, S. Burger, F. Schmidt, and M. Wegener, *Photonic metamaterials: Magnetism at optical frequencies*, invited paper, IEEE J. Sel. Top. Quant. Electr. **12**, 1097 (2006).

- M. W. Klein, C. Enkrich, M. Wegener, and S. Linden, *Second-harmonic generation from magnetic metamaterials*, Science **313**, 502 (2006).

- M. W. Klein, C. Enkrich, M. Wegener, C. M. Soukoulis, and S. Linden, *Single-slit split-ring resonators at optical frequencies: Limits of size scaling*, Opt. Lett. **31**, 1259 (2006).

- M. W. Klein, T. Tritschler, M. Wegener, and S. Linden, *Lineshape of harmonic generation by metallic nanoparticles and metallic photonic crystal slabs*, Phys. Rev. B **72**, 115113 (2005).

<u>At conferences (only own presentations):</u>

- M. W. Klein, C. Enkrich, M. Wegener, J. Förstner, J. V. Moloney, W. Hoyer, T. Stroucken, T. Meier, S. W. Koch, and S. Linden, *Optical experiments on second-harmonic generation with metamaterials composed of split-ring resonators*, talk TuC5, Photonic Metamaterials: From Random to Periodic (OSA Topical Meeting), Grand Bahama Island, The Bahamas, June 5-8, 2006.

- M. W. Klein, C. Enkrich, M. Wegener, J. Förstner, J. V. Moloney, W. Hoyer, T. Stroucken, T. Meier, S. W. Koch, and S. Linden, *Optical experiments on second-harmonic generation with metamaterials composed of split-ring resonators*, talk QThE3, Quantum Electronics and Laser Science Conference (QELS), Long Beach, USA, May 21-26, 2006.

- M. W. Klein, C. Enrich, M. Wegener, J. Förstner, J. V. Moloney, W. Hoyer, T. Stroucken, T. Meier, S. W. Koch, and S. Linden, *Nonlinear-optical response of meta-materials: Experimental demonstration of second-harmonic generation*, talk Q 25.4, Spring Meeting of the Deutsche Physikalische Gesellschaft, Frankfurt, Germany, March 13-17, 2006.

- M. W. Klein, T. Tritschler, S. Linden, and M. Wegener, *Nonlinear-optical experiments on waveguide-plasmon polaritons using 5-fs laser pulses*, talk QMK1, Quantum Electronics and Laser Science Conference (QELS), Baltimore, USA, May 22-27, 2005.

- M. W. Klein, T. Tritschler, S. Linden, and M. Wegener, *Nonlinear-optical experiments on waveguide-plasmon polaritons using 5-fs laser pulses*, talk HL 49.1, Spring Meeting of the Deutsche Physikalische Gesellschaft, Berlin, Germany, March 4-9, 2005.

Additional work on other topics has been published:

In scientific journals:

- M. Decker, M. W. Klein, M. Wegener, and S. Linden, *Circular dichroism of planar chiral magnetic metamaterials*, Opt. Lett., in press (2007).

- D. Nau, A. Schönhardt, C. Bauer, A. Christ, T. Zentgraf, J. Kuhl, M. W. Klein, and H. Giessen, *Correlation effects in disordered metallic photonic crystal slabs*, Phys. Rev. Lett., in press (2007).

- T. Tritschler, K. D. Hof, M. W. Klein, and M. Wegener, *Variation of the carrier-envelope phase of few-cycle laser pulses owing to the Gouy phase: A solid-state-based measurement*, Opt. Lett. **30**, 753 (2005).

At conferences (only own presentations):

- T. Tritschler, K. D. Hof, M. W. Klein, and M. Wegener, *Variation of the carrier-envelope phase of few-cycle laser pulses due to the Gouy phase*, poster JThE116, Conference on Lasers and Electro-Optics (CLEO), Baltimore, USA, May 22-27, 2005.

Contents

Zusammenfassung

Die Wechselwirkung von Licht mit Licht, die über die alltäglichen Effekte der linearen Optik hinausgeht, wird als nichtlineare Optik bezeichnet und ist seit der Erfindung des Lasers im Jahr 1960 experimentell zugänglich. Seitdem wird dieses Phänomen mit grundlagenphysikalischer Bedeutung unter verschiedensten Bedingungen untersucht. Der Laser hat außerdem das Gebiet der Optik um die Photonik erweitert, also die Wissenschaft und Anwendung von Photonen mit gezielten Eigenschaften. Die Photonik ist kürzlich von Wissenschaftlern und Politikern gleichermaßen zu einer der Schlüsseltechnologien des 21. Jahrhunderts ausgerufen worden. Die vorliegende Arbeit untersucht nichtlineare optische Effekte für zwei bestimmte Materialien, die zu den sogenannten photonischen Kristallen und photonischen Metamaterialien gehören. In diesen Forschungsgebieten wurden in den letzten Jahren bahnbrechende Erfolge erzielt, wie die Herstellung von Materialien mit einer optischen Bandlücke oder Magnetismus bei optischen Frequenzen. Diese Fortschritte sind unter anderem durch den Einsatz von Methoden aus der Nanotechnologie erreicht worden.

Konkret werden in der vorliegenden Arbeit nichtlineare optische Eigenschaften von lithographisch hergestellten metallischen Nanostrukturen, nämlich von eindimensionalen plasmonischen Kristallen und photonischen Metamaterialien, sowohl experimentell als auch theoretisch untersucht. Bei diesen beiden Materialien wechselwirkt das starke elektromagnetische Feld eines fokussierten Laser-Lichtstrahls mit bestimmten metallischen Nanostrukturen und verursacht so eine optische Frequenzverdopplung (abgekürzt SHG) und -verdreifachung (THG).

Zu allen Experimenten wurden entsprechende Proben aus strukturierten Goldpartikeln mit Hilfe der Elektronenstrahl-Lithographie hergestellt, wobei eine Polymer-Maske erzeugt wird, durch die Gold aufgedampft wird. Das Aufbringen dünner Schichten aus Metall oder dielektrischen Materialien wurde mit Elektronenstrahl-Verdampfen durchgeführt.

Bei einem eindimensionalen plasmonischen Kristall (MPCS) führt die periodische Anordnung von dünnen Drähten auf einem Schichtwellenleiter zur Kopplung einer photonischen Resonanz an eine elektronische Resonanz. Die photonische Resonanz tritt auf, da aufgrund der Gitterkonstante der Drähte nur Licht einer bestimmten Wellenlänge an die Wellenleitermode gekoppelt werden kann. Wie bei Photonischen Kristallen üblich, muss deshalb die Gitterkonstante die gleiche Größenordnung wie die Wellenlänge besitzen (etwa 1 µm oder kleiner). Die elektronische Resonanz stammt vom Partikelplasmon, einer kollektiven Schwingung der Leitungsband-Elektronen in jeder metallischen Nanostruktur. Diese Schwingung wird durch das Lichtfeld und die Rückstellkraft angetrieben, welche durch die auf den Metalloberflächen auftretenden Oberflächenladungen entsteht. Bei einem MPCS

sind diese beiden Resonanzen gekoppelt, da die jeweiligen Feldverteilungen sich räumlich überlappen. Daher ist dieses System ideal geeignet für die Untersuchung einer starken Kopplung zweier Resonanzen mit optischen Methoden.

Um nichtlineare optische Effekte interpretieren zu können, muss man üblicherweise zuerst die linearen optischen Eigenschaften eines Systems verstanden haben. Für MPCSs treten in gemessenen Extinktionsspektren (Extinktion=Absorption+Streuung) üblicherweise ein „anti-crossing" und sogenannte Fano-Linienformen auf. Wir konnten zeigen, dass diese beiden Beobachtungen sehr gut durch das von uns entwickeltes Modell beschrieben werden können, das auf zwei gekoppelten Lorentz-Oszillatoren basiert. Unser einfaches, klassisches Modell übertrifft sogar frühere Modelle, die auf phänomenologischen Parametern oder einer von der Quantenmechanik inspirierten Beschreibung basieren. Beim Erweitern unseres Modells auf die nichtlineare Optik konnten wir den Bereich der „moderaten Kopplung" identifizieren, in welchem entsprechende THG-Spektren Informationen über die zu Grunde liegende Quelle der optischen Nichtlinearität liefern. Des Weiteren zeigen die nichtlinearen Spektren, die für die Anregung mit zwei zeitversetzten Pulsen berechnet wurden, eine Schwebung in den spektralen Mischprodukten der zwei in linearer Optik auftretenden Moden, jedoch keine Schwebung in den dritten Harmonischen dieser Moden.

Für entsprechende Experimente zur THG-Untersuchung unserer MPCS-Proben werden Laserimpulse von 5 Femtosekunden Dauer (aus einem Titan-Saphir-Oszillator) und ein Interferometer verwendet. Unsere Experimente gehen über bisherige Arbeiten dadurch hinaus, dass wir eine verbesserte Zeitauflösung erreichen und zusätzlich das interferometrische THG-Signal spektral auflösen. Die Spektren zeigen ein unterschiedliches Verhalten der verschiedenen spektralen Komponenten bezüglich der Zeitverzögerung. Einige spektrale Komponenten weisen eine Schwebung auf, andere nicht, was in Einklang steht mit unserer Theorie. Des Weiteren hängen die Abfallzeiten der Einhüllenden stark von der spektralen Komponente ab. Die gemessenen Spektren stimmen qualitativ sehr gut mit den Voraussagen unseres einfachen theoretischen Modells überein. Der Vergleich ermöglicht uns, die Schwingung des Partikelplasmons als Hauptquelle der Nichtlinearität zu identifizieren.

Für den allgemeinen Fall von Ansammlungen von Nanopartikeln konnten wir ein historisches Missverständnis aufklären: Wir zeigten analytisch und numerisch, dass der Vergleich von zeitaufgelösten Femtosekunden SHG- oder THG-Experimenten in Kombination mit Extinktionsmessungen es nicht erlaubt, die homogenen und inhomogenen Beiträge zur Linienbreite zu unterscheiden, was im krassen Gegensatz zur Behauptung einer früheren Arbeit steht. Wir haben diesen Widerspruch eindeutig auf einen Rechenfehler in dieser früheren Arbeit zurückgeführt. Als Ergebnis kann die Plasmon-Zerfallzeit, die mit der homogenen Linienbreite zusammenhängt, nicht aus dem Vergleich von linear-optischen und SHG- oder THG-Daten bestimmt werden.

Der zweite Teil dieser Arbeit bezieht sich auf photonische Metamaterialien, welche ebenso künstliche optische Materialien sind, die jedoch aus reagierenden Bausteinen („Atomen") bestehen, die kleiner sind als die relevanten Wellenlängen. Ein Durchbruch in dem jungen Gebiet der photonischen Metamaterialien ist die kürzliche Demonstration von Materialien mit einer bei optischen Frequenzen schwingenden Magnetisierung und sogar von Materialien mit einem negativen Brechungsindex. Das bekannteste „Atom", das in diesem

Gebiet gerne diskutiert wird, ist der Schlitz-Ring-Resonator (SRR), der vereinfacht als ein kleiner LC-Schwingkreis angesehen werden kann, wobei der Ring eine Spule mit einer Windung und der Schlitz im Ring einen Kondensator darstellt. Einfallendes Licht kann oszillierende Ströme anregen, die in diesem Ring fließen. Die Ströme entsprechen der grundlegenden LC-Mode oder höheren Moden. Einige spezielle Moden eines SRRs besitzen bekanntlich magnetische Dipolmomente. Daher sind Metamaterialien ideal geeignet für Studien mit Materialien, die möglicherweise auf die Magnetfeld-Komponente des Lichts reagieren.

Dies ist besonders interessant in der nichtlinearen Optik, in der das Magnetfeld durch den magnetischen Anteil der Lorentz-Kraft ins Spiel kommen kann. Wenn ein SRR mit Licht angeregt wird, kann das lokale Magnetfeld im SRR oder nahe außerhalb in eine völlig andere Richtung zeigen als das Magnetfeld der anregenden Lichtwelle. Darauf beruhend erklärten wir, dass eine SHG-Abstrahlung, die auf dem magnetischen Anteil der Lorentzkraft basiert und in der Vorwärtsrichtung detektiert wird, in Metamaterialien prinzipiell möglich ist. Dagegen ist diese Abstrahlung für viele natürliche Materialien aufgrund der Richtung dieser Kraft bekanntlich ausgeschlossen. Diese neue Möglichkeit war die Motivation für unsere nichtlinearen optischen Untersuchungen an Metamaterialien.

Unsere Experimente zur SHG und THG stellen die erste systematische Studie der nichtlinearen Optik von Metamaterialien überhaupt dar. Dazu verwendeten wir die optischen Pulse von 170 fs Dauer eines optisch-parametrischen Oszillators, um die nichtlinearen Signale von unterschiedlichen, planar angeordneten SRRs zu vergleichen, die mit verschiedenen Moden (Resonanzen) assoziiert sind. Diese SRRs wurden mit senkrecht auf die Proben einfallendem Licht der festen Wellenlänge von 1.5 µm angeregt. Die bei weitem stärksten SHG- und THG-Signale werden für diejenigen Resonanzen beobachtet, die die größten magnetischen Dipolmomente besitzen. Bei geringer Verstimmung der Resonanz (d.h. für eine Probe mit leicht anderen Parametern als eine resonante Probe) sowie bei nichtresonanter Anregung nehmen die Signale wie erwartet ab. Zusätzlich zeigen andere photonische Metamaterialien ohne magnetische Dipolmomente, die als resonante „Kontrollproben" dienen, kein messbares SHG-Signal und ein sehr geringes THG-Signal.

Um den Charakter der nichtlinearen Signale genauer zu untersuchen, die wir für unsere Metamaterial-Proben aus resonanten SRRs erhielten, wurden auch SHG-Experimente mit schräg einfallendem Anregungslicht durchgeführt. Wir beobachten ein komplexes Verhalten des SHG-Signals für ansteigenden Einfallswinkel (bezogen auf die Normalenrichtung der Probenoberfläche). Das stärkste Signal wird immer noch für die Resonanz mit größtem magnetischen Dipolmoment und senkrechtem Einfall erhalten, aber auch das mit zunehmendem Winkel monoton abnehmende Signal dieser Probe ist größer als das Signal der anderen untersuchten Proben mit kleineren magnetischen Dipolmomenten. Diese Proben wiederum zeigen ein nicht-monotones Verhalten des SHG-Signals für zunehmenden Einfallswinkel. Kleine Asymmetrien des SHG-Signals bezüglich der Verkippung der Probe in die eine oder entgegengesetzte Richtung werden beobachtet. Diese Asymmetrien müssen auf geringe Abweichungen von der Spiegelsymmetrie unserer hergestellten SRRs zurückgeführt werden.

Die linearen optischen Transmissionsspektren der SRR-Proben wurden mit entsprechenden numerischen Simulationen sehr gut reproduziert. Für diese Simulationen verwendeten wir ein kommerzielles Softwarepaket, das wir auf den Fall von Metamaterialien anpassten.

Eine Finite-Elemente-Methode wurde benutzt, um die räumlich aufgelösten elektromagnetischen Felder in und um die SRRs herum für die lineare Optik zu berechnen. Die Finiten Elemente wurden so gewählt und die Randbedingungen so programmiert, dass Simulationen für senkrechten und schrägen Einfall möglich und einfach handhabbar gemacht wurden.

Leider sind wir aktuell nicht in der Lage, die Ergebnisse unserer nichtlinearen optischen Experimente mit einer vollständigen mikroskopischen nichtlinearen Theorie für photonische Metamaterialien zu vergleichen. Aufgrund unserer experimentellen Bedingungen kann man erwarten, dass Quanteneffekte der Metallelektronen keine Rolle spielen. Daher kann man annehmen, dass eine klassische Beschreibung der Nichtlinearitäten des Elektronen-Plasmas ein adäquater Startpunkt ist: Man muss das Newtonsche Gesetz für Metallelektronen, also mit einem elektrischen und magnetischen Anteil der Lorentzkraft, selbstkonsistent mit den Maxwell-Gleichungen für die metallische Nanostruktur lösen. Eine entsprechende Theorie wurde in den mit uns kooperierenden Arbeitsgruppen von S. W. Koch und J. V. Moloney formuliert und ist in dieser Arbeit wiedergegeben. Dieselben Arbeitsgruppen untersuchen aktuell auch entsprechende numerische („finite-difference time-domain") Simulationen mit SRR-Metamaterialien, jedoch sind aufgrund von Problemen mit der Stabilität und Konvergenz bisher keine belastbaren Ergebnisse erzielbar gewesen. In dieser Theorie ist der magnetische Anteil der Lorentzkraft eine Größe, die im Volumen des Metalls auftritt. Im Gegensatz dazu stammt eine SHG-Abstrahlung, die auf den elektrischen Anteil des Lichts zurückzuführen ist, ausschließlich von der Oberfläche des Metalls, da die Ladungsdichte in erster Störungsordnung im Metallvolumen konstant ist. Speziell diese Oberflächenbeiträge sind bei numerischen Auswertungen kritisch.

Daher entwickelten wir für die beschriebene Theorie eine Näherung, die einfache Abschätzungen ermöglicht. In der von uns eingeführten „Angetriebener-Dipol-Näherung" (DDA) werden die Kräfte, die auf die Leitungselektronen innerhalb jedes einzelnen SRRs wirken, zu einer Nettokraft addiert und die Elektronen zu einer einzelnen beweglichen Ladung zusammengefasst, auf die dann die Nettokraft wirkt. Die Anwendung dieser Näherung und die Annahme, dass ausschließlich der magnetische Anteil der Lorentzkraft als Nichtlinearität wirkt, ermöglichen uns, numerische Daten aus linearen optischen Simulationen wiederzuverwenden. Entsprechende Ergebnisse sind konsistent zu unseren experimentellen SHG-Daten für senkrechten Einfall. Das ist jedoch noch kein Beweis dafür, dass diese Annahmen tatsächlich den dominanten Beitrag beschreiben. Deswegen verglichen wir die zusätzlichen experimentellen SHG-Daten aus unseren winkelaufgelösten Untersuchungen mit Ergebnissen einer analogen Rechnung für schräge SHG-Abstrahlung. Hier führt die DDA zu einer Zweideutigkeit, d.h. zu zwei verschiedenen Ergebnissen. Keines der beiden Ergebnisse passt jedoch vollständig zu den Experimenten, woraus wir schließen können, dass mindestens eine unserer beiden Annahmen für die Theorie, die auf dem magnetischen Anteil der Lorentzkraft und der DDA beruht, für schrägen Einfall zu hinterfragen ist. Folglich ist zukünftig auf dem Gebiet der nichtlinearen optischen Metamaterialien vor allem mehr theoretische Arbeit nötig. Solche Theorien können anhand der experimentellen Daten der vorliegenden Arbeit umfassend überprüft werden.

Eine der Hauptideen innerhalb des sich entwickelnden Gebiets der photonischen Metamaterialien ist, künstliche, maßgeschneiderte optische Materialien zu entwerfen und herzu-

stellen, welche lineare und/oder nichtlineare optische Eigenschaften besitzen, die bei natürlichen Substanzen nicht auftreten. Bezüglich der nichtlinearen Optik ist ein offensichtliches Ziel, die effektiven nichtlinearen optischen Koeffizienten um Größenordnungen zu steigern. Für sehr dünne Filme übertreffen die in dieser Arbeit vorgestellten Metamaterialien mit magnetischen Dipolen bereits übliche SHG-Materialien um mehrere Zehnerpotenzen bezüglich der Konversionseffizienz. Selbstverständlich liegt eine der zukünftigen Herausforderungen darin, diesen Erfolg auf größere und vor allem dickere Metamaterial-Strukturen auszudehnen, um für Anwendungen bedeutsam zu werden. Solche dreidimensionalen (anstatt planaren) photonischen Metamaterialien befinden sich heute noch in den Anfängen. In diesem Zusammenhang müssen außerdem die dann auftretenden Probleme der Absorption und Phasenanpassung gelöst werden.

Chapter 1

Introduction

With the invention of the laser in the year 1960 [1], the field of optics has expanded into the field of photonics: Intense coherent radiation consisting of photons with defined properties has become available as a tool in laboratories and beyond. Soon thereafter, the first experiments on optical Second-Harmonic Generation (SHG) have been realized [2], forming the first experiments in which light intentionally interacts with light (photons). This has been the beginning of the field of nonlinear optics. In the following decades, various nonlinear-optical effects have been investigated, including wavelength conversion, optical harmonic generation, intensity-dependent material parameters as the refractive index, nonlinear quantum-optical effects and many more [3–5].

All these nonlinear effects generally require a certain material which mediates the interaction of light with light. To understand the physical processes leading to nonlinear phenomena in such nonlinear-optical materials is of fundamental scientific importance. For semiconductors, metals, and gases illuminated with intense light, often quantum-mechanical effects are responsible for nonlinearities, but in many cases the reasons can be found in classical physics, for example, in anharmonicities of potentials or relativistic effects [6]. Thus, investigating materials with methods such as optical Second- and Third-Harmonic Generation (THG) gives insights into basic physical processes and relations.

Knowing the mechanisms of the nonlinearities also promises applications based on tailored nonlinear effects. Here, the interaction of light with light is ambiguous: For example, in optical data transmission, on one hand, one wants to suppress nonlinear processes to avoid cross-talk and information loss, but, on the other hand, in order to manipulate light (with light), strong nonlinearities of materials are desired for active elements such as the proposed all-optical switches [7]. Optical telecommunication networks, providing the enormous worldwide information transfer today, are only one recognized application of photonics. In analogy to electronic data processing, which has lead to the development of a vast semiconductor industry in the past century, photonics has been declared one of the key technologies of the 21$^{\text{st}}$ century by scientific and political quarters [8, 9].

In this thesis, we investigate the fundamental nonlinear-optical effects of nanostructures which are based on metallic constituents. At first sight, in optics, metals seem to be suitable for mirrors but impractical for the use in transmissive media because of losses associated

with the finite metal conductivity. However, metals are also connected to strong local field enhancements and to high nonlinearities which are orders of magnitude larger than those of typical dielectrics, rendering metals highly interesting for our studies. Even more, for metallic particles with sizes on the sub-micrometer scale, specific plasmonic resonances appear, and provide additional field enhancements [10]. The character of these resonances and their corresponding optical response, importantly, can be tailored by carefully designing the metallic particles in terms of shape, size, type of metal, and dielectric environment. We study such tailored material structures, which are fabricated on the nanometer scale by methods known from the fast-growing field of nanotechnology.

In particular, we investigate the nonlinear-optical properties of Metallic Photonic Crystal Slabs (MPCSs) and photonic Metamaterials. The former material belongs to a subclass of Photonic Crystals (PCs) [11, 12], which are artificial materials possessing a photonic band structure due to Bragg scattering. During the last two decades, the field of Photonic Crystals has proposed and/or realized optical materials with various unprecedented properties such as band-gap materials, high-Q microcavities, and enhanced phase-matching for nonlinear frequency conversion. Beyond these fundamental aspects, corresponding applications (such as PC-based optical fibers) have been developed. Metallic Photonic Crystal Slabs, consisting of a slab waveguide and a periodic array of metallic nanowires, combine the idea of Photonic Crystals with the outstanding optical properties of metallic nanoparticles. For MPCSs, we investigate the femtosecond dynamics of physical processes underlying their nonlinear-optical response by time-resolved THG experiments with ultrashort laser pulses.

Photonic Metamaterials [13], in turn, are an even newer class of artificial optical materials. They consist of responsive building blocks ("atoms") smaller than relevant wavelengths of light and have opened the door to the realization of materials with previously inconceivable optical properties. For example, photonic Metamaterials have proven (in the year 2004) the possibility of magnetism at optical frequencies [14]. With this aspect, many standard textbooks of optics would have to be rewritten, because they usually assume a relative permeability of unity for electromagnetic waves in media. A negative index of refraction and the idea of a "perfect lens" beating the diffraction limit are only two more of the numerous aspects forming the motivation in this fascinating field. As to the nonlinear optics in photonic Metamaterials, several effects (e.g., SHG in a negative-index material) have been discussed only theoretically, always assuming given nonlinearity coefficients. We present the first experiments on the nonlinear optics of photonic Metamaterials. In particular, we study and compare SHG and THG from magnetic and non-magnetic photonic Metamaterials.

All experiments presented in this thesis are compared to corresponding calculations. For a theoretical description, it is often helpful to apply an approximation: It can, on one hand, help to clarify which are the essential mechanisms that, taken alone, can well explain experimental results, and on the other hand, an approximation is sometimes necessary to get a grip on a quantitative evaluation of a complex system at all. For MPCSs, we develop a simple model of two coupled Lorentz oscillators, which turns out to describe the observed linear- and nonlinear-optical effects extremely well. For photonic Metamaterials, we apply a finite-element method to describe the linear optics numerically. For their nonlinear optics, an analytical microscopic theory, which explains a nonlinear mechanism and has been

developed by our collaborating groups of S. W. Koch and J. V. Moloney, is reproduced in this thesis. Additionally, we develop an approximation in which the response of a nanoscale building block is contracted to a point charge, allowing to estimate the nonlinear-response from the known linear fields. This model is consistent with a part of the experiments.

In the year 1959, R. P. Feynman said, "there is plenty of room at the bottom," implying that there is much to be discovered and employed from what the world at the nanoscale offers. This is definitely true for the field of nanophotonics as well, promising the feasibility of materials with linear- and nonlinear-optical properties tailored at will.

Outline of this thesis

In chapter 2, we review the fundamentals of linear and nonlinear optics, focussing on metals at the nanoscale. Additionally, we introduce Metallic Photonic Crystal Slabs and photonic Metamaterials, especially so-called Split-Ring Resonators (SRRs), and give an overview of the current states of the research fields. Chapter 3 is devoted to the description of the experimental methods for the fabrication and linear- and nonlinear-optical characterization. In chapter 4, we explain details of our numerical finite-element calculations, since the reliability of corresponding results critically depends on specific factors.

The following chapters report our experimental and theoretical findings. In chapter 5, we start by clarifying a historical mistake, from which we conclude that we do not want to consider plasmonic decay times in detail later. For MPCSs, we develop a simple model and derive its linear-optical and THG response theoretically in chapter 6. Corresponding experiments are presented in chapter 7. The parameters discussed in these chapters are chosen to be comparable and the results are displayed in the same format.

Chapters 8 and 9 describe the theory and experiments, respectively, for our photonic Metamaterials. In the theory chapter, we discuss the detailed results of our linear-optical numerical calculations. We then repeat the analytical nonlinear theory based on the electric and magnetic part of the Lorentz force as a source of nonlinearity. Thereafter, we explain our Driven-Dipole Approximation (DDA) and its analytical conclusions. The theory chapter for Metamaterials finishes with our presentation of the nonlinear results of our calculations based on the magnetic part of the Lorentz force and on the application of the DDA. Most of our experiments presented in chapter 9 are performed with two principal samples consisting of SRRs. Their linear-optical, SHG, and THG properties are discussed for normal-incidence illumination and partially also for oblique-incidence illumination. Along the way, we discuss results from several control samples. Finally, we conclude in chapter 10.

Chapter 2

Principles of nanoscale optics

With the ability to structure materials on the scale of the wavelengths of visible light and smaller, the field of nanoscale optics has emerged and developed during the last decades. In this chapter, we introduce and describe properties of materials used in nanoscale optics, restricted to aspects which are relevant within the framework of this thesis.

We start by introducing the basic quantities and relations of linear optics (section 2.1) and nonlinear optics (section 2.2). The materials with key properties for this work are metals, thus we address their optics in section 2.3. The remaining parts of this chapter are dedicated to introduce the concepts and basic properties of the two classes of optical materials which are investigated in this thesis: Metallic Photonic Crystal Slabs (section 2.4) and photonic Metamaterials (section 2.5).

2.1 Linear optics

2.1.1 Maxwell equations, linear wave equation, Fresnel formulas

All electromagnetic effects are governed by the Maxwell equations [15]. In SI units, they read

$$\nabla \cdot \boldsymbol{D} = \rho \,, \tag{2.1a}$$

$$\nabla \cdot \boldsymbol{B} = 0 \,, \tag{2.1b}$$

$$\nabla \times \boldsymbol{E} = -\frac{\partial \boldsymbol{B}}{\partial t} \,, \tag{2.1c}$$

$$\nabla \times \boldsymbol{H} = +\frac{\partial \boldsymbol{D}}{\partial t} + \boldsymbol{j} \,. \tag{2.1d}$$

The electric charge density ρ and the electric current density $\boldsymbol{j}$ are related by the charge conservation law

$$\nabla \cdot \boldsymbol{j} + \frac{\partial \rho}{\partial t} = 0 \,. \tag{2.2}$$

Inside a medium, the electric field $\boldsymbol{E}$ and the electric displacement $\boldsymbol{D}$ are related via the polarization $\boldsymbol{P}$,

$$\boldsymbol{D} = \varepsilon_0 \boldsymbol{E} + \boldsymbol{P} \,, \tag{2.3}$$

5

while the magnetic field $\boldsymbol{H}$ and the magnetic induction[1] $\boldsymbol{B}$ are related via the magnetization $\boldsymbol{M}$,

$$\boldsymbol{B} = \mu_0(\boldsymbol{H} + \boldsymbol{M})\,. \tag{2.4}$$

Here, ε_0 and μ_0 are the vacuum permittivity and permeability, respectively.[2]

In linear optics, the polarization is simply proportional to the electric field

$$\boldsymbol{P} = \varepsilon_0\chi\boldsymbol{E}\,, \tag{2.5}$$

where χ is the linear susceptibility of the medium.[3] Alternatively, the medium is described by the relative permittivity $\varepsilon = 1 + \chi$ for which

$$\boldsymbol{D} = \varepsilon_0\varepsilon\boldsymbol{E} \tag{2.6}$$

holds. The medium is additionally described by its relative permeability μ with

$$\boldsymbol{B} = \mu_0\mu\boldsymbol{H}\,. \tag{2.7}$$

In general, ε and μ can be tensors, however, we will consider only isotropic media for which ε and μ are scalars. For natural substances and optical frequencies, one exclusively finds $\mu = 1$. In section 2.5, we will briefly address the effect that photonic Metamaterials, being composite materials, can possess an effective relative permeability $\mu_{\mathrm{eff}} \neq 1$. However, this aspect has no relevance for all other parts of this thesis, where we will take the point of view of the constituent, natural materials with $\mu = 1$.

Taking these simplifications together with the Maxwell equations, one can derive the wave equation for linear optics

$$\nabla \times \nabla \times \boldsymbol{E} + \frac{\varepsilon}{c_0^2}\frac{\partial^2}{\partial t^2}\boldsymbol{E} = 0\,, \tag{2.8}$$

where $c_0 = 1/\sqrt{\varepsilon_0\,\mu_0} \approx 3{\times}10^8$ m/s is the vacuum speed of light. Here, we additionally assumed that no free charges or currents appear ($\rho = 0$, $\boldsymbol{j} = 0$). This also holds whenever metals are described by their permittivity (see section 2.3). We will only deviate from this assumption when initially deriving optical properties of metals in section 2.3 and 8.2.

By introducing the traditional refractive index

$$n = \sqrt{\varepsilon}\,, \tag{2.9}$$

and the speed of light $c = c_0/n$ in a corresponding medium, Eq. (2.8) can be simplified to

$$\nabla \times \nabla \times \boldsymbol{E} + \frac{1}{c^2}\frac{\partial^2}{\partial t^2}\boldsymbol{E} = 0\,. \tag{2.10}$$

One simple solution of Eq. (2.10) is a plane wave

$$\boldsymbol{E}(\boldsymbol{r}, t) = \hat{\boldsymbol{E}}_0\cos(\boldsymbol{k} \cdot \boldsymbol{r} - \omega_0 t)\,, \tag{2.11}$$

---

[1]To comply with general use, we will often use the term "magnetic field" also for $\boldsymbol{B}$.
[2]$\varepsilon_0 = 8.8542{\times}10^{-12}$ A s /(V m) and $\mu_0 = 4\pi{\times}10^{-7}$ V s /(A m)
[3]Equation (2.5) holds for an instantaneous response. Dispersive media are treated in section 2.1.2.

with the wave vector $\boldsymbol{k}$ pointing in the direction of propagation. Equation (2.11) is a solution of Eq. (2.10) if $\boldsymbol{k} \cdot \hat{\boldsymbol{E}}_0 = 0$ and $\omega_0 = c|\boldsymbol{k}|$. The direction of the amplitude $\hat{\boldsymbol{E}}_0$ is called the polarization of the electromagnetic wave.[4] We will give values for light frequencies ω_0 with corresponding numbers in units of terahertz (THz), or alternatively photon energies $\hbar\omega_0$ in electron-volts (eV), or state the vacuum wavelength $2\pi c_0/\omega_0$ in micrometers (µm). Finally, the intensity of the wave is defined as

$$ I = \frac{1}{2} \sqrt{\frac{\varepsilon_0}{\mu_0}} \, n \hat{\boldsymbol{E}}_0^2 \, . \tag{2.12} $$

Considering an interface between two media in the absence of free charges and currents, the Maxwell equations (2.1) state which field components are continuous across this interface: the tangential parts of the electric field, $\boldsymbol{E}_\parallel$, and magnetic field, $\boldsymbol{H}_\parallel$, as well as the normal components of the electric displacement, $\boldsymbol{D}_\perp$, and the magnetic induction, $\boldsymbol{B}_\perp$.

As a consequence, a plane wave incident onto a flat interface between two media with refractive indices n_1 and n_2 is partially reflected and partially transmitted (refracted). The angle of incidence[5] α_1 of the incident wave determines the propagation direction of the reflected wave, $-\alpha_1$, and the angle α_2 into which the refracted wave travels, according to Snell's law

$$ n_1 \sin\alpha_1 = n_2 \sin\alpha_2 \, . \tag{2.13} $$

For the electric field amplitude $\hat{\boldsymbol{E}} = \hat{\boldsymbol{E}}_\mathrm{P} + \hat{\boldsymbol{E}}_\mathrm{S}$ one must independently consider the component $\hat{\boldsymbol{E}}_\mathrm{P} = \hat{E}_\mathrm{P} \boldsymbol{e}_\mathrm{P}$ parallel to the plane which is spanned by the propagation direction and the surface normal, and the component $\hat{\boldsymbol{E}}_\mathrm{S} = \hat{E}_\mathrm{S} \boldsymbol{e}_\mathrm{S}$ perpendicular to this plane ($|\boldsymbol{e}_\mathrm{P}| = |\boldsymbol{e}_\mathrm{S}| = 1$). If only one component is nonzero, we speak of P-polarization in the former and S-polarization in the latter case. The magnitudes of the field components are described by the Fresnel formulas [15]

$$ \frac{\hat{E}_\mathrm{R,S}}{\hat{E}_\mathrm{I,S}} = -\frac{\sin(\alpha_1 - \alpha_2)}{\sin(\alpha_1 + \alpha_2)} \, , \tag{2.14a} $$

$$ \frac{\hat{E}_\mathrm{T,S}}{\hat{E}_\mathrm{I,S}} = 1 - \frac{\sin(\alpha_1 - \alpha_2)}{\sin(\alpha_1 + \alpha_2)} \, , \tag{2.14b} $$

$$ \frac{\hat{E}_\mathrm{R,P}}{\hat{E}_\mathrm{I,P}} = -\frac{\tan(\alpha_1 - \alpha_2)}{\tan(\alpha_1 + \alpha_2)} \, , \tag{2.14c} $$

$$ \frac{\hat{E}_\mathrm{T,P}}{\hat{E}_\mathrm{I,P}} = \left(1 - \frac{\tan(\alpha_1 - \alpha_2)}{\tan(\alpha_1 + \alpha_2)} \right) \frac{\cos\alpha_1}{\cos\alpha_2} \, . \tag{2.14d} $$

Here, the indices I, R, and T correspond to the incident, reflected, and transmitted (refracted) waves, respectively.

---

[4]In this thesis, the term "polarization" is used to describe both the density of electric dipoles, $\boldsymbol{P}$, and the direction of the electric field of an electromagnetic plane wave, $\hat{\boldsymbol{E}}_0$, in agreement with general use.

[5]the angle between the propagation direction and the interface normal

2.1.2 Frequency domain

In the Maxwell equations (2.1) above, we have described the electromagnetic fields as (space and) time-dependent quantities. It is often advantageous to express equations in terms of fields which depend on frequency rather than on time. When the electric field oscillates harmonically with a specific frequency $\omega_0 > 0$, we can write

$$\boldsymbol{E}(\boldsymbol{r}, t) = \text{Re}\left[\hat{\boldsymbol{E}}(\boldsymbol{r})\, \mathrm{e}^{-\mathrm{i}\omega_0 t}\right]. \tag{2.15}$$

We will often be lax and only write

$$\boldsymbol{E}(\boldsymbol{r}, t) = \hat{\boldsymbol{E}}(\boldsymbol{r})\, \mathrm{e}^{-\mathrm{i}\omega_0 t} \tag{2.16}$$

and keep in mind that only the real part of the expression is physically relevant. In general, the amplitude $\hat{\boldsymbol{E}}$ can be complex-valued.

In the general non-harmonic case, and again using the "lax" formulation, the electric field can be expressed as

$$\boldsymbol{E}(\boldsymbol{r}, t) = \int_0^\infty \mathrm{d}\omega\, \mathrm{e}^{-\mathrm{i}\omega t}\, \tilde{\boldsymbol{E}}(\boldsymbol{r}, \omega). \tag{2.17}$$

Here and in the following we disregard negative frequencies. As a consequence, we can relate a field $\boldsymbol{E}(t) = \hat{\boldsymbol{E}}_0 \cos(\omega_0 t)$ with $\tilde{\boldsymbol{E}}(\omega) = \hat{\boldsymbol{E}}_0 \delta(\omega - \omega_0)$, where δ is the Dirac function.

Using Eq. (2.17) in the Maxwell equations (2.1), one can simplify all time derivatives, and the wave equation (2.8) becomes

$$\nabla \times \nabla \times \tilde{\boldsymbol{E}}(\boldsymbol{r}, \omega) - \frac{\omega^2}{c_0^2}\varepsilon(\boldsymbol{r}, \omega)\tilde{\boldsymbol{E}}(\boldsymbol{r}, \omega) = 0. \tag{2.18}$$

We anticipate that the permittivities of the different materials distributed in space can depend on the light frequency, or wavelength.

2.2 Perturbative nonlinear optics

The previous section applies to linear media for which Eq. (2.5) holds. One step more generally, the polarization $\boldsymbol{P}$ can be a nonlinear function of the electric field $\boldsymbol{E}$,

$$\boldsymbol{P}/\varepsilon_0 = \chi\boldsymbol{E} + \chi^{(2)} : \boldsymbol{E}\boldsymbol{E} + \chi^{(3)} : \boldsymbol{E}\boldsymbol{E}\boldsymbol{E} + \dots, \tag{2.19}$$

where : denotes the product of the nonlinear susceptibility tensor $\chi^{(2,3,\dots)}$ with the vector fields [3]. The nonlinear susceptibilities depend on the microscopic structure of a medium and the nonlinear physical processes taking place on this scale.

For the Taylor expansion (2.19) to be meaningful, the summands should become successively smaller in magnitude, which holds in the regime called perturbative nonlinear optics. For the contrary case, [6] and [16] describe examples of the regime of extreme nonlinear optics. Since the metal used for the samples to be described later interacts strongly with

electromagnetic radiation, we are confined to moderate electric field strengths and to perturbative nonlinear optics. Hence, the nonlinearities we investigate cause only small alterations to the dominant linear-optical phenomena.

If we split the general polarization (2.19) into its linear and its nonlinear part

$$\boldsymbol{P} = \varepsilon_0 \chi \boldsymbol{E} + \boldsymbol{P}_{\mathrm{NL}}(\boldsymbol{E}) \,, \tag{2.20}$$

we can write the nonlinear-optical wave equation as

$$\nabla \times \nabla \times \boldsymbol{E} + \frac{\varepsilon}{c_0^2} \frac{\partial^2}{\partial t^2} \boldsymbol{E} = -\mu_0 \frac{\partial^2}{\partial t^2} \boldsymbol{P}_{\mathrm{NL}} \,. \tag{2.21}$$

Equation (2.21) allows to outline the procedure of describing nonlinear optics successively according to the order of perturbation:

(i) The linear optics is described by (2.21) with $\boldsymbol{P}_{\mathrm{NL}}$ set to zero.

(ii) Using the linear electric field to determine $\boldsymbol{P}_{\mathrm{NL}}$ of certain polynomial order, the right-hand side of the wave equation (2.21) describes the *source* of a nonlinear electric field.

(iii) The generated nonlinear electric field *propagates* self-consistently according to the left-hand side of Eq. (2.21).

(iv) The self-consistent linear and nonlinear fields can potentially be used recursively to determine fields of higher perturbative order.

Even more generally, the nonlinear source on the right-hand side of Eq. (2.21) does not have to be related to an electric-dipole polarization, but can be the result of any particular microscopic physical process.

2.2.1 Second- and Third-Harmonic Generation

Starting in linear optics with an electric field $E^{(1)}$ (omitting vectors temporarily), the second-order susceptibility $\chi^{(2)}$ causes, in conjunction with the wave equation, a second-order contribution to the electric field, $E^{(2)}$. As an example, we choose a light pulse with Gaussian temporal envelope (pulse length $\propto \tau$) and carrier frequency ω_0,

$$E^{(1)}(t) = \hat{E}_0 \, \mathrm{e}^{-(t/\tau)^2} \cos(\omega_0 t) \,. \tag{2.22}$$

Neglecting propagation, the second-order field becomes

$$\begin{aligned}
E^{(2)}(t) &\propto \chi^{(2)} \hat{E}_0^2 \, \mathrm{e}^{-2(t/\tau)^2} \cos^2(\omega_0 t) \\
&= \chi^{(2)} \hat{E}_0^2 \, \mathrm{e}^{-2(t/\tau)^2} \frac{1}{2} \left(1 + \cos(2\omega_0 t) \right) \,.
\end{aligned} \tag{2.23}$$

The contribution with carrier frequency $2\omega_0$ is called Second-Harmonic Generation (SHG). The constant term in the brackets is called optical rectification and will mostly be ignored

in this thesis. Furthermore, one can note from Eq. (2.23) that the generated SHG pulse is shorter than the original pulse by a factor $\sqrt{2}$.

Second-Harmonic Generation is not possible for all materials. In a centrosymmetric medium, when changing the coordinate system such that $r \rightarrow -r$, all vector quantities must also change sign, e.g., for the linear electric field vector $\boldsymbol{E}^{(1)} \rightarrow -\boldsymbol{E}^{(1)}$. However, the second-order polarization cannot change sign since

$$\frac{\boldsymbol{P}^{(2)}}{\varepsilon_0} = \chi^{(2)} : \boldsymbol{E}^{(1)} \boldsymbol{E}^{(1)} \rightarrow \chi^{(2)} : \left(-\boldsymbol{E}^{(1)}\right)\left(-\boldsymbol{E}^{(1)}\right) = +\chi^{(2)} : \boldsymbol{E}^{(1)} \boldsymbol{E}^{(1)} = +\frac{\boldsymbol{P}^{(2)}}{\varepsilon_0} ,$$

(2.24)

so the inversion symmetry is only fulfilled if $\boldsymbol{P}^{(2)} = 0$. In conclusion, SHG requires a medium without centrosymmetry. An example for such a medium is a planar array of Split-Ring Resonators (see section 2.5.1).

The Metallic Photonic Crystal Slabs introduced in section 2.4 are centrosymmetric, so the lowest possible order for nonlinear optics is a third-order process, connected with $\chi^{(3)}$. Following the above example with the Gaussian pulse, the third-order electric field is

$$
\begin{aligned}
E^{(3)}(t) \quad &\propto \quad \chi^{(3)} \hat{E}_0^3 \, \mathrm{e}^{-3(t/\tau)^2} \, \cos^3(\omega_0 t) \\
&= \quad \chi^{(3)} \hat{E}_0^3 \, \mathrm{e}^{-3(t/\tau)^2} \frac{1}{4} \left(3\cos(\omega_0 t) + \cos(3\omega_0 t)\right) .
\end{aligned}
$$

(2.25)

The contribution with carrier frequency $3\omega_0$ is called Third-Harmonic Generation (THG), the term with carrier frequency ω_0 is attributed to self-phase modulation which will be ignored henceforth. The resulting pulses are shorter than the original pulse by a factor $\sqrt{3}$.

THG can appear in all media as a $\chi^{(3)}$-process. We note in passing that for non-centrosymmetric media, THG can additionally arise due to a two-step, cascaded $\chi^{(2)}$-process [3] with a third-order source term $\chi^{(2)} : \boldsymbol{E}^{(2)} \boldsymbol{E}^{(1)}$.

From the above equations, and using Eq. (2.12), it follows that the SHG intensity $I^{(2)}$ is proportional to the square of the linear intensity $I^{(1)}$,

$$I^{(2)} \propto \left[I^{(1)}\right]^2 ,$$

(2.26)

and similarly the THG intensity $I^{(3)}$ to the third power of the exciting intensity

$$I^{(3)} \propto \left[I^{(1)}\right]^3 .$$

(2.27)

Perturbative SHG and THG as above can easily be formulated in the frequency domain:

$$\nabla \times \nabla \times \tilde{\boldsymbol{E}}^{(2)} - \left(\frac{\omega}{c_0}\right)^2 \varepsilon \tilde{\boldsymbol{E}}^{(2)} = \left(\frac{\omega}{c_0}\right)^2 \chi^{(2)} : \tilde{\boldsymbol{E}}^{(1)} * \tilde{\boldsymbol{E}}^{(1)}$$

(2.28)

$$\nabla \times \nabla \times \tilde{\boldsymbol{E}}^{(3)} - \left(\frac{\omega}{c_0}\right)^2 \varepsilon \tilde{\boldsymbol{E}}^{(3)} = \left(\frac{\omega}{c_0}\right)^2 \chi^{(3)} : \tilde{\boldsymbol{E}}^{(1)} * \tilde{\boldsymbol{E}}^{(1)} * \tilde{\boldsymbol{E}}^{(1)} .$$

(2.29)

The multiplication in the time domain is replaced by a convolution (denoted by $*$) here. The Gaussian pulse from above transformed into the frequency domain [cf. Eq. (2.17)] leads to

$$\tilde{E}^{(1)}(\omega) = \hat{E}_0 \sqrt{\pi} \tau \, \mathrm{e}^{-\tau^2(\omega - \omega_0)^2/4} ,$$

(2.30)

which is a Gaussian-shaped spectrum peaked around $\omega \approx \omega_0 > 0$. The frequency spectrum of the SHG field consequently corresponds to a convolution of $\tilde{E}^{(1)}(\omega)$ with itself, which is a Gaussian spectrum peaked around $\omega \approx 2\omega_0 > 0$ and with a spectral width which is broadened by a factor $\sqrt{2}$ with respect to the linear-optical spectrum. The frequency spectrum of the THG field in turn corresponds to a double convolution of $\tilde{E}^{(1)}(\omega)$ with itself, delivering a Gaussian spectrum around $\omega \approx 3\omega_0 > 0$ and even larger width. The larger spectral width is directly related to the shorter pulse length of the nonlinear fields as stated earlier. We will make use of our considerations about multiplications and convolutions in section 6.2 again.

2.2.2 The Lorentz force in nonlinear optics

In a medium (e.g., a semiconductor), the linear polarization $\boldsymbol{P}^{(1)} = (-e)n_e\boldsymbol{x}^{(1)}$ can be related to electrons with charge $(-e)$ and density n_e being displaced by $\boldsymbol{x}^{(1)}$ from their equilibrium position. Illumination with an electromagnetic plane wave oscillating with a single frequency ω_0 thus results in an electron velocity $\boldsymbol{v}^{(1)} = \partial\boldsymbol{x}^{(1)}/\partial t$. In the simplest case, the velocity $\boldsymbol{v}^{(1)}$, the polarization $\boldsymbol{P}^{(1)}$ and the incident electric field $\boldsymbol{E}^{(1)}$ will all point into the same direction, which in turn is perpendicular to the wave vector $\boldsymbol{k}$. Furthermore, if the electrons can be viewed individually, the magnetic field $\boldsymbol{B}^{(1)}$ at the position of an electron corresponds to the value and orientation of the incident field, hence $\boldsymbol{B}^{(1)} \propto \boldsymbol{k} \times \boldsymbol{E}^{(1)}$.

It is obvious that such an electron feels the magnetic part of the Lorentz force $\boldsymbol{F}_{\mathrm{L,m}} = (-e)\boldsymbol{v}^{(1)} \times \boldsymbol{B}^{(1)}$, which is of second order in perturbation. The second-order oscillation $\boldsymbol{x}^{(2)}$ at frequency $2\omega_0$ resulting from this force can lead to SHG radiation. However, under the conditions described above, the dipole oscillation $(-e)\boldsymbol{x}^{(2)}$ is directed parallel to $\boldsymbol{k}$. Thus, a SHG wave cannot be radiated into the propagation direction of the exciting wave, nor into the reflected direction, which makes the magnetic part of the Lorentz force irrelevant for most nonlinear-optical experiments using solid-state samples. If the experimental setup allows, SHG may be observed in a direction perpendicular to $\boldsymbol{k}$. For free electrons, corresponding non-relativistic and relativistic SHG experiments have been reported [17].

In chapters 8 and 9 we will investigate materials in which a SHG wave based on the magnetic part of the Lorentz force can, in principle, radiate into the far-field forward direction. This new possibility arises because the "magnetic" Metamaterials used there can have a local magnetic field $\boldsymbol{B}^{(1)}$ which does not point into the same direction as the magnetic field of the incident wave.

2.3 Optics of metals

We describe a metal by a free electron gas confined to a volume in which additionally the immobile ion background resides [10]. The linear-optical properties are derived below, whereas the nonlinear optics is presented in section 8.2.

In response to a local electric field $\boldsymbol{E}$, the equation of motion of an electron with mass m_e and charge $(-e)$ is

$$\ddot{\boldsymbol{x}} + \gamma_{\mathrm{c}}\dot{\boldsymbol{x}} = \frac{-e}{m_e}\boldsymbol{E} \,. \tag{2.31}$$
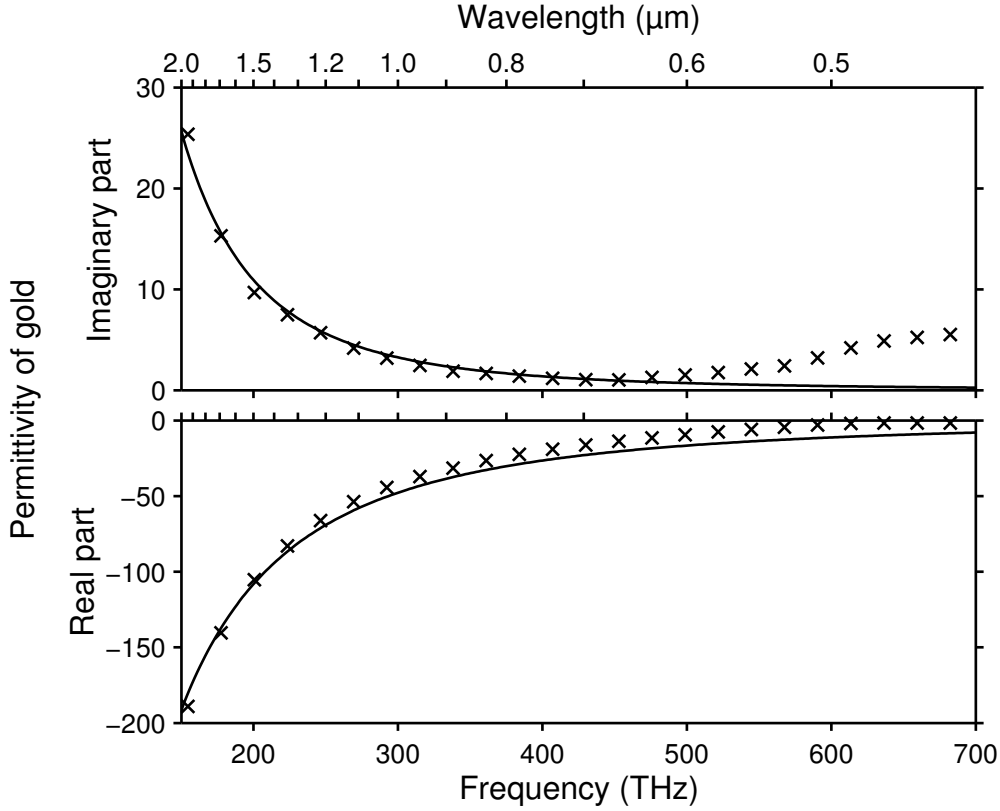
Figure 2.1: The relative permittivity of gold. Experimental values (crosses) measured for thin films [18], and the description by a Drude metal (solid lines), Eq. (2.33), as a fit to the experimental data around the frequency 200 THz. At frequencies higher than 550 THz (0.55 μm wavelength), the imaginary part of the permittivity and thus the absorption is strongly increased by interband transitions, giving gold its yellowish color.

Here, $\boldsymbol{x}$ is the electron displacement and γ_{c} is the collision frequency of the Drude metal [10] representing Ohmic damping. In the frequency domain, driving the electron with a harmonic electric field with amplitude $\hat{\boldsymbol{E}}_0$ and frequency ω results in the oscillation amplitude

$$\hat{\boldsymbol{x}} = -\frac{1}{\omega(\omega + \mathrm{i}\gamma_{\mathrm{c}})}\frac{-e}{m_e}\hat{\boldsymbol{E}}_0 \,. \tag{2.32}$$

The electrons of density n_e then make up a polarization $\hat{\boldsymbol{P}} = (-e)n_e\hat{\boldsymbol{x}}$, and, since also $\hat{\boldsymbol{P}} \overset{!}{=} \varepsilon_0(\varepsilon_{\mathrm{D}} - 1)\hat{\boldsymbol{E}}_0$, this allows to define a relative permittivity ε_{D} to describe the metal:

$$\varepsilon_{\mathrm{D}}(\omega) = 1 - \frac{\omega_{\mathrm{pl}}^2}{\omega(\omega + \mathrm{i}\gamma_{\mathrm{c}})} \,. \tag{2.33}$$

Here, $\omega_{\mathrm{pl}} = \sqrt{(n_e e^2)/(\varepsilon_0 m_e)}$ is the plasma frequency of the Drude metal.

Figure 2.1 shows the real and imaginary part of the permittivity of gold, as determined by experiments [18], as well as a fit of the Drude formula (2.33): For the frequency part of highest interest here, around $\omega = 2\pi \times 200\,\mathrm{THz}$, gold is best described by a plasma frequency $\omega_{\mathrm{pl}} = 2\pi \times 2100\,\mathrm{THz}$ and a collision frequency $\gamma_{\mathrm{c}} = 2\pi \times 20\,\mathrm{THz}$. However, for the gold
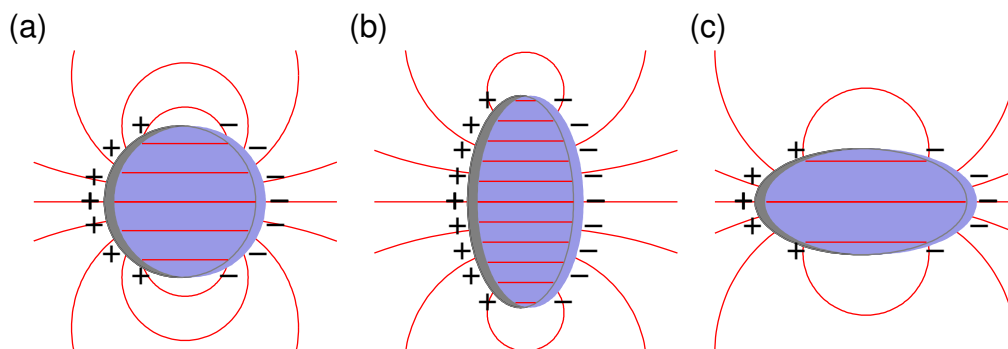
Figure 2.2: Particle plasmons. (a) All electrons (blue area) inside a spherical particle (gray shape) can oscillate in parallel: The appearing surface charges create a depolarization field inside the particle, acting as a restoring force for this harmonic oscillator. (b) In a flatter particle, the depolarization field is larger, increasing the restoring force and the particle plasmon resonance frequency. (c) In a sharper particle, the depolarization field extends to far outside the particle and is weaker inside, reducing the particle plasmon resonance frequency.

structures we fabricate (see section 3.1.1), a higher damping rate of $\gamma_{\mathrm{c}} = 2\pi \times 50\,\mathrm{THz}$ is used to better fit to the experimental results.

What happens if a plane wave with frequency ω is incident on a vacuum-metal interface? Because of the high reflectivity of the metal and the phase jump of the reflected wave [see Eqs. (2.14)], the field amplitude right at the interface resulting from superposition is very small compared to the incident field. The resulting field, however, can enter the metal, since its parallel component is conserved. Inside the metal, the field amplitude of the plane wave decays exponentially because the refractive index $n = \sqrt{\varepsilon_{\mathrm{D}}} = n_r + \mathrm{i}\kappa$ and hence the wave vector $k = n\omega/c_0$ are mostly imaginary. The corresponding skin depth $\delta = c_0/(\omega\kappa)$ has a value of $24\,\mathrm{nm}$ for gold at $200\,\mathrm{THz}$. Since our gold structures have thicknesses of the same order, the penetration of transverse electric fields is considerable.

A wave incident on a metal surface under oblique angles in P-polarization also has a component of the electric field which is normal to the metal surface. This field component is associated with a non-zero charge density ρ near the interface, and its magnitude decays very fast inside the metal, approximately on the scale of a Thomas-Fermi screening length, which is about $0.06\,\mathrm{nm}$ for gold [19].

2.3.1 Optics of metal nanoparticles

Metal nanoparticles (MNP) with a finite volume and highly curved surfaces have unique optical properties [10] beyond flat metal surfaces discussed above. The simplest case is a spherical particle [see Fig. 2.2(a)] with a size much smaller than relevant wavelengths, hence it can be described in the electrostatic approximation where no retardation of fields is considered. At a particular time all conduction electrons of the metal particle shall be displaced homogeneously by a small displacement $\boldsymbol{x}_0$. The electrons which are shifted beyond the ionic background on one side, and the bare ions themselves on the other side, constitute surface charges creating a homogeneous depolarization field $\boldsymbol{E}_0$ inside the sphere [10, 20]. This electric field accelerates the electrons against their displacement, subsequently making

them swing over beyond their equilibrium position, continuing a harmonic oscillation called particle plasmon.

The particle plasmon is hence an eigenmode of the collective oscillation of the conduction electrons. Its eigenfrequency is not primarily determined by particle size, but rather material parameters like the density of electrons. For a sphere, the polarization $\boldsymbol{P}_0 = (-e)n_e\boldsymbol{x}_0$ is connected with a depolarization field $\boldsymbol{E}_0 = -\frac{1}{3}\boldsymbol{P}_0/\varepsilon_0$ [20]. Using $\boldsymbol{E}_0$ as the only driving force in Eq. (2.31) and neglecting damping, one obtains that the eigenfrequency of the spherical particle plasmon is

$$\Omega_{\text{sphere}} = \frac{1}{\sqrt{3}}\,\omega_{\text{pl}}\,. \tag{2.34}$$

For metal particles with ellipsoidal shape [see Fig. 2.2(b) and (c)], there is one particle plasmon mode for each of the three main axes of the ellipsoid. Each axis ($i = x$, y, z) can be assigned a depolarization factor L_i for which $\boldsymbol{E}_0 = -L_i\boldsymbol{P}_0/\varepsilon_0$ holds, while generally $L_x + L_y + L_z = 1$ is fulfilled [10, 20]. Again, the eigenfrequencies depend on shape rather than on size. For a sphere, $L_i = 1/3$ holds for all directions. For an ellipsoid, the longer axes are assigned smaller values of L_i than the shorter axes. The corresponding particle plasmon frequency $\Omega_{\text{PP}} = \sqrt{L_i}\omega_{\text{pl}}$ is hence reduced when elongating a given particle along the plasmon oscillation direction.

For larger particles with sizes approaching the order of particle plasmon resonance wavelengths, one has to consider retardation effects and higher-order oscillation modes. This is possible in an analytical description for spherical particles within the framework of the Mie theory [21]. For (nearly) ellipsoidal particles, one can still use the qualitative dependence described above. We will make use of this fact in chapter 7 to experimentally tune the particle plasmon frequency of gold nanowires.

Various other particle shapes can be considered. Among these are curved particles which allow for a particle plasmon oscillation with a magnetic dipole moment. We will consider such particles briefly in section 2.5.1 and in more detail in section 8.1. Generally, the exact modes and field distributions for a metal nanoparticle of arbitrary shape can only be described accurately with sophisticated numerical methods (see chapter 4).

An important aspect of a particle plasmon is that it generally comprises an electric dipole moment. On one hand, this oscillating dipole radiates, and the associated energy loss significantly broadens the linewidth of the emission spectrum. On the other hand, an incident electromagnetic wave can couple to the dipole and excite the corresponding plasmon oscillation. The electric field inside the metal is then a superposition, of a wave decaying on the order of the skin depth and of the depolarization field. In the case of plasmons which also comprise a magnetic dipole moment, the linear-optical coupling strength of the electric field to the plasmon is usually stronger than that of the magnetic field [22].

It is clear from the above said that a particle plasmon oscillation, on an abstracted level, can be described as a harmonic oscillator, with the abstract charge q, mass m, and displacement $x(t)$, driven by the electric field $E(t)$, and the equation of motion

$$\ddot{x} + 2\gamma\dot{x} + \Omega_0^2 x = \frac{q}{m}E(t)\,. \tag{2.35}$$

This ansatz leads to a Lorentz oscillator resonance with the damped eigenfrequency $\Omega = \sqrt{\Omega_0^2 - \gamma^2}$ and the half-width-at-half-maximum (HWHM) $\gamma = 1/T_2 = 1/(2\tau)$, which is the homogeneous linewidth.[6] Here, T_2 is the dephasing time and τ is the plasmon decay time. Recently, high-resolution experiments on single gold nanoparticles have revealed particle plasmon decay times τ of 0.7–9 fs [23].

However, most other investigations have used samples consisting of ensembles of many particles, in which the homogeneous linewidth is obscured in absorption spectra by inhomogeneous broadening. Much experimental effort [24–30] has been devoted to distinguish the homogeneous and inhomogeneous contributions to particle plasmon linewidths. In particular, a combination of linear- and nonlinear-optical methods has been proposed [24]. Our proof that the combination of SHG or THG and linear optics is, on the contrary, not suitable to determine a homogeneous linewidth [31] is given in chapter 5.

The terms particle plasmon, particle plasmon resonance, and Mie resonance are often used as synonyms. A surface plasmon polariton, to clarify the difference, only describes a travelling electromagnetic wave at a (often) flat metal-dielectric interface.

2.3.2   Second-Harmonic Generation from metal surfaces

An electromagnetic wave incident onto an isotropic continuous metal surface at normal incidence, or oblique incidence in S-polarization, cannot create a SHG wave because of symmetry reasons [32]. However, SHG in reflection is possible for oblique incidence and P-polarization. First corresponding experiments [33] have been published in 1965, shortly after the invention of the laser providing the necessary field strengths. Many more experimental [34–36] as well as theoretical [37–41] investigations up to recent years have lined the history of SHG at metal surfaces, including data and models that partially contradict each other. Here, we want to trace the main discussion, restricted to the nanoscale. Thus we will neglect much-discussed effects like interband transitions and crystal orientation of the metal.

Analytically, there are two second-order contributions to nonlinear optics:

(i) The incident wave is mainly reflected, which is caused by electronic currents $\boldsymbol{j}^{(1)}$ within the skin depth of the surface. Due to the penetrating magnetic field $\boldsymbol{B}^{(1)}$, the moving electrons feel the magnetic part of the Lorentz force, $\boldsymbol{j}^{(1)} \times \boldsymbol{B}^{(1)}$.

(ii) The mentioned currents are not divergence-free. From Eq. (2.2) it follows that a surface charge density $\rho^{(1)}$ appears which diminishes the normal component of the electric field $\boldsymbol{E}^{(1)}$ inside the metal. The electric part of the Lorentz force, however, also has a second-order contribution $\rho^{(1)}\boldsymbol{E}^{(1)}$.

The relative strengths of (i) and (ii) as contributions to SHG have been discussed widely in the literature. Publications supporting a dominant role of (ii) over (i) can be found [33, 40], as well as ones supporting an almost equal contribution [34, 38, 39]. To date, the final conclusion remains open [35, 36]. "Magnetic" Metamaterials (see chapters 8 and 9), although

---

[6]The homogeneous linewidth or damping constant of a general Lorentz oscillator, γ, is not to be confused with the Drude metal collision frequency, γ_c.

not being continuous metal films, may contribute to the mosaic of data and a broader under-standing of SHG from metallic nanostructures.

2.4   Metallic Photonic Crystal Slabs

In order to introduce Metallic Photonic Crystal Slabs, we will briefly summarize the concept and basic properties of Photonic Crystals and optical slab waveguides. For more information on these two topics, we refer to the broad literature stated along the way.

General concept of Photonic Crystals

Photonic Crystals (PCs) [11, 12, 42–46] are tailored, composite materials with special optical properties. They are usually made out of two or more dielectric (or metallic) materials with different relative permittivities. These materials are structured periodically and arranged in a lattice, in one, two, or three dimensions. The simplest 1D PC is the common dielectric mirror [47], consisting of a periodic stack of alternating dielectric layers with different refractive indices. By means of nanofabrication techniques, sophisticated designs of PCs have also been realized experimentally in 2D and 3D (see [48–50] and references therein).

The most important physical mechanism in PCs is Bragg reflection of an electromag-netic wave. Consequently, PCs must be periodic on a length scale similar to the involved wavelengths of light (as opposed to Metamaterials, see section 2.5).

The key property of a PC is the appearance of a photonic band structure: Due to the spatial periodicity of the permittivity $\varepsilon(\boldsymbol{r}, \omega)$ in the wave equation (2.18), the solutions for the electric field are Bloch-periodic (vector) functions. This stands in analogy to the electronic wave functions and band structure in, e.g., semiconductors [20]. Similarly, a PC can exhibit a flat photonic dispersion relation near the boundary of the Brillouin zone, and even a band gap can appear, i.e., a band of optical frequencies for which no propagating waves exist inside the PC. These properties make Photonic Crystals highly interesting materials for applications in optics and telecommunication.

Optical slab waveguides

A slab waveguide [see Fig. 2.3(a)] [51–53] is a thin planar slab of optical material(s) permit-ting the propagation of an electromagnetic wave in a direction within the plane. It consists of a slab of a material with a high refractive index, the core, surrounded by materials with lower refractive indices. Like in an optical fiber, total internal reflection leads to the formation of a standing wave in the mode profile across the slab thickness, while the wave propagates in direction parallel to the plane of the slab.

Outside the core, only evanescent parts of a mode exist, so a waveguide mode cannot loose energy in a direction perpendicular to the slab waveguide. On the other hand, this means that a mode cannot be excited from this direction either. Coupling of light from the normal direction into a specific waveguide mode requires an arbitrary grating coupler pro-viding the lateral photon momentum [see Fig. 2.3(b)] [54–56]. The grating lattice constant
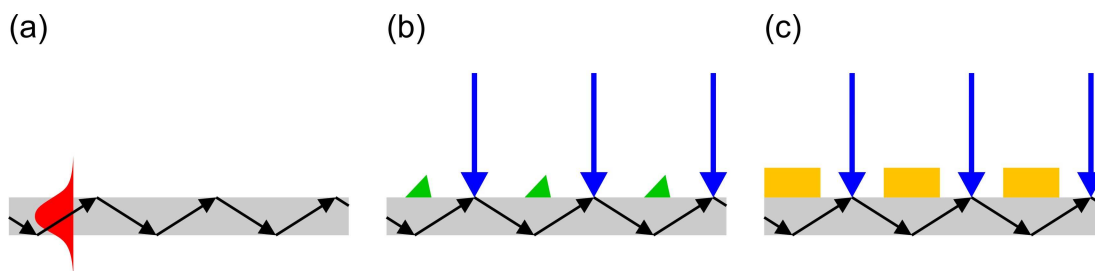
Figure 2.3: (a) A slab waveguide consists of a thin slab of dielectric material (gray) with high refractive index compared to its environment. The intensity profile (red) of the guided wave, as well as the arrows symbolizing the propagation and total internal reflection of the waveguide mode ("zigzag wave" [51]) are shown. (b) The added grating coupler (green) allows to excite the specific waveguide mode by light from above (blue). (c) In a Metallic Photonic Crystal Slab, the grating is implemented by metal wires (orange) stretching infinitely in the direction perpendicular to the plane shown. The two resonances, the waveguide mode and the wire particle plasmon, are coupled due to the overlap of the respective electric fields [cf. also Fig. 2.2(c)].

determines the propagation constant or effective wavelength of this waveguide mode and, via the waveguide dispersion relation, the waveguide mode frequency. The waveguide mode can be excited if the frequency of the incident light is resonant.

There are two possibilities for the polarization: (i) In a TE-mode, the electric field is parallel to the slab and perpendicular to the propagation direction, whereas (ii) in a TM-mode, the magnetic field of the wave is parallel to the slab and perpendicular to the propagation direction. The polarization of the incident light, in reference to the grating, determines whether a TE or TM mode is excited. Certain conditions involving the refractive indices and slab thickness must be fulfilled for the appearance of the ground modes (TE_0 or TM_0) [57].

Definition of Metallic Photonic Crystal Slabs

In a Metallic Photonic Crystal Slab (MPCS) [58–61], the grating coupler is implemented by a set of identical metal nanowires [see Fig. 2.3(c)]. At first sight, it inherits properties from both a slab waveguide and a particle plasmon.

Light can be coupled into the waveguide from the normal direction because of the efficient grating coupler. Propagating inside the waveguide with an effective wavelength matching the grating period, however, the waveguide mode also fulfills the condition for (partial) Bragg reflection. This stands in analogy to a 1D Photonic Crystal (although the periodic arrangement appears here in a direction perpendicular to the incident light direction).

If the electric field of the incident light is oriented across the wires [as in Fig. 2.3(c)], a particle plasmon resonance can be excited (cf. section 2.3.1). In contrast, if the electric field is directed along the infinite wires, the depolarization factor L is zero and a particle plasmon resonance does not exist. Corresponding to the polarization of the excited waveguide mode, the former case is called TM-polarization and the latter case is called TE-polarization. In this thesis, we will only consider excitation in TM-polarization in which a particle plasmon resonance can be excited if the frequency of the incident light matches.

Thus, two individual resonances appear: The waveguide mode resonance frequency Ω_{wg} is determined by the wires' period, while the particle plasmon resonance frequency Ω_{pl} is

determined by the wire width (assuming a constant wire thickness). The electric field distributions of the individual resonances, however, overlap spatially, which leads to a coupling of the two resonances. The key feature of a MPCS, hence, is the coupling of a photonic resonance with an electronic resonance. The coupling leads to the formation of new resonances or eigenmodes, which sometimes have been termed waveguide-plasmon polaritons [59].

While waveguide-plasmon polaritons can be described with high accuracy by microscopic electromagnetic calculations (e.g., the scattering-matrix method [62, 63]), this description does not lead to a deeper understanding of the new eigenmodes. More insight has been obtained from a semi-quantum mechanical Hamilton approach explained in [59], which has proven to reproduce some of the optical properties of MPCSs known from the experiments presented in the same work.

In section 6.1 we will take a different approach and describe MPCSs as two coupled Lorentz oscillators. This purely classical approach is simple but can serve to explain most of the important properties of MPCSs. Furthermore, and in contrast to other descriptions [30], our theory can easily and consistently be extended to nonlinear optics (section 6.2). Corresponding linear-optical experiments (section 7.2) and THG experiments (section 7.3) agree very well with our theoretical description.

2.5   General concepts of photonic Metamaterials

During the last years, the field of photonic Metamaterials [13] has opened a new chapter of optics. Photonic Metamaterials are artificial, composite materials with designed optical properties. In contrast to Photonic Crystals (cf. section 2.4), however, Metamaterials are built from structural elements which are (much) smaller than the light wavelengths of interest, thus, Bragg reflection does not play a role. Rather, the optical properties of a Metamaterial can be understood from the physics of each *single* responsive element.

The main idea of Metamaterials initially conceived by [64] is to build "artificial atoms" which have a designed electric and/or magnetic dipole response. An electromagnetic wave with a wavelength much longer than the size and arrangement of these "atoms" does not "see" the individual parts, but averages over the response of many parts. This stands in analogy to an electromagnetic wave travelling through a natural substance consisting of many real atoms. Whereas a natural atom and all dielectric materials only have an electric-dipole response at optical frequencies, nanofabrication techniques also allow to design artificial "atoms" with a magnetic response [14]. While a periodic arrangement of "atoms" in a Metamaterial is generally not necessary, it is often chosen nevertheless in order to ease the fabrication process (see section 3.1.2 and [22, 65, 66]).

Figure 2.4 shows common examples of designs (partially explained below) which have been realized or proposed as "magnetic atoms". In all cases, metallic structures with a certain geometry allow for circulating currents. Generally, a circulating current is connected with a magnetic dipole moment, and magnetic moments of a certain density form an effective magnetization M_{eff}. If the circulating currents are induced by the external magnetic field H of an electromagnetic wave, then the Metamaterial can be described with an effective
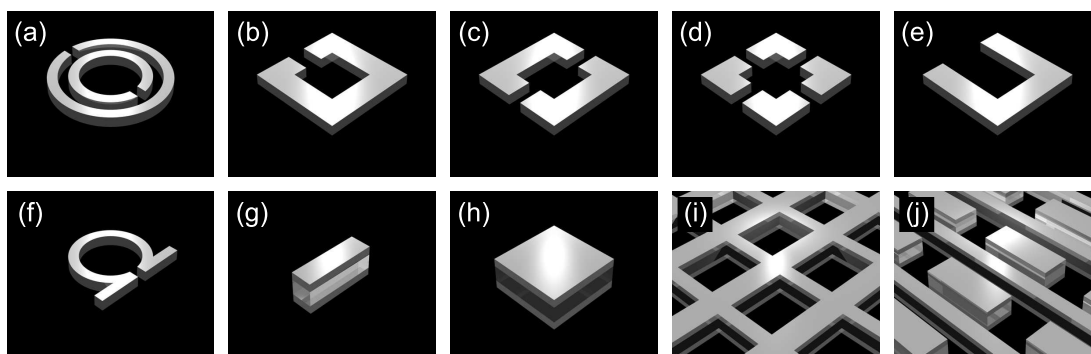
Figure 2.4: Examples of designs for (a)-(h) "magnetic atoms" and (i)-(j) materials with a negative index of refraction. (a) Doubled Split-Ring Resonator. (b), (c) and (d) Split-Ring Resonator with one, two, and four slits, respectively. (e) U-shaped Split-Ring Resonator. (f) Ω-structure. (g) Cut-wire pairs. (h) Square-plate pairs. (i) Crossed double-wires. (j) Cut-wire pairs as "magnetic atoms" combined with long-wire pairs as "electric atoms". Taken from [22] (for details, see there).

permeability $\mu_{\mathrm{eff}} \neq 1$, even at optical frequencies [14, 22].

Various conclusions follow from $\mu_{\mathrm{eff}} \neq 1$. Just to name a few: If both permittivity $\varepsilon_{\mathrm{eff}}$ and permeability μ_{eff} of a Metamaterial are simultaneously negative, the Maxwell equations (2.1) describe refraction into negative angles [67]. According to Snell's law, the traditional refractive index then has to be replaced by $n_{\mathrm{eff}} = -\sqrt{\varepsilon_{\mathrm{eff}}\mu_{\mathrm{eff}}}$. Experiments have supported this negative index of refraction [68]. Generally, the Fresnel formulas [47] and other electromagnetic quantities have to be reformulated to account for $\mu_{\mathrm{eff}} \neq 1$. A large part of the attraction Metamaterials receive stems for the idea of a perfect lens [69, 70] beating the diffraction limit of usual lenses, and the idea of electromagnetic cloaking [71–73].

Beyond these fascinating linear-optical effects, Metamaterials promise unprecedented phenomena in nonlinear optics [64]. Most of the effects described above arise at light frequencies matching a certain resonance of the "atoms" (similar to the particle plasmon resonances discussed in section 2.3.1). The resonant behavior enhances the electromagnetic near fields, which are already strong in the vicinity of the metallic structures with edges and bends (lightning-rod effect). The so enhanced fields also favor nonlinear effects (cf. section 2.2). In chapter 9, we describe the first nonlinear-optical experiments with Metamaterials in which especially magnetic-dipole resonances show a prominent nonlinear signal [74].

We clarify that in the context of this thesis, negative refraction and the description of Metamaterials by effective parameters $\varepsilon_{\mathrm{eff}}$ and μ_{eff} do not play a role. We will rather maintain the point of view of the constituent materials with their geometries and consider the electromagnetic near fields within the "atoms". For this purpose, it is sufficient to define Metamaterials as to consist of "atoms" in "unit cells" which are just smaller than wavelengths of light, such that no diffraction appears, i.e., all diffraction orders beyond the zeroth order are only evanescent waves.

Most of the theoretical papers published so far on nonlinear Metamaterials have focussed on 3D bulk effects of a material with a negative effective index of refraction [75–77]. For our planar 2D Metamaterials and and their microscopic physics, however, no published theory exists, to the best of our knowledge, so we derive our own theory in chapter 8.

2.5.1   Split-Ring Resonators

Historically the first [64], and conceptually the easiest design of a "magnetic atom" is the Split-Ring Resonator (SRR) [78–80], which is shown in Fig. 2.4(a)-(f) in different modifications. Here, we will exclusively use the designs of Fig. 2.4(b) and (e). A SRR is basically a single winding of a microscopic coil, with the ends of the SRR arms forming a capacitance. Hence, it is a small LC-resonance circuit, with a resonance frequency scaling antiproportional with its size [81, 82] as long as this resonance frequency is far below the plasma frequency [83–85] (cf. also section 2.3.1). The circulating current flowing in the coil results in a magnetic moment directed perpendicular to the plane of the SRR.

During the last few years, the increasing miniaturization of SRRs has lead to tremendous steps of their resonance wavelength, from $30\,\mathrm{mm}$ [68], via $300\,\mathrm{\mu m}$ [86], $50\,\mathrm{\mu m}$ [87], $3.2\,\mathrm{\mu m}$ [14], $1.5\,\mathrm{\mu m}$ [88, 89], down to $900\,\mathrm{nm}$ [85], in work of others and of ourselves. In the last case, the resonance frequency is already outside the size-scaling regime mentioned above, and a further reduction of the SRR resonance wavelength will hardly be possible with the chosen materials.

The LC-circuit resonance is only the ground mode of a SRR. Beyond, also higher modes exist, similar to the modes on a straight antenna (see Fig. 2.5): A straight antenna has a ground mode of which half the wavelength matches the length of the antenna [(a), one antinode]. The next higher mode, (b), has two antinodes (and one node), and the third mode, (c), has three antinodes (and two nodes). The three most important modes of a SRR [Fig. 2.5(d)-(f)] can be understood when considering a SRR as a straight antenna with the two ends folded up by 90 degrees, and corresponding current distributions.

The analogy between SRRs and antennas applies to the mode patterns, not necessarily to the relative resonance frequencies. In the SRR samples discussed in chapters 8 and 9, the SRR modes (e) and (f) are almost at the same frequency. This is obtained from experiments and from numerical simulations taking into account the details of the SRR geometries (cf. section 4.1.1). Also note that the resonant currents of nanoscale SRRs are dominantly volume currents in the metal (cf. section 2.3.1).

The current patterns for the three SRR modes in Fig. 2.5(d)-(f) can all be related to electric dipole moments: In (d) and (f), the electric dipole moment lies in the horizontal direction (on this page), in (e) it is vertical. Moreover, two of the resonances can also be related to magnetic dipole moments pointing perpendicular to this page: In (d), the magnetic moment is stronger than in (f), where the currents partially counter-propagate. This clarifies our naming convention to call the three important SRR modes the "magnetic resonance", the "vertical electric resonance", and the "horizontal electric resonance", respectively.

Because of their dipole moments, the SRR modes couple to electromagnetic waves, either with the electric or magnetic field of the wave, or with both. However, coupling of the electric field to a resonance is usually much stronger than the coupling of the magnetic field of the same wave [89]. This aspect will be confirmed by our angle-resolved linear-optical experiments in section 9.3.1. For normal incidence, i.e., a plane wave incident perpendicular to the designs in Fig. 2.5, exclusively the electric field of the wave can couple to and excite the three SRR resonances.
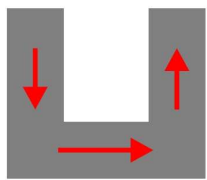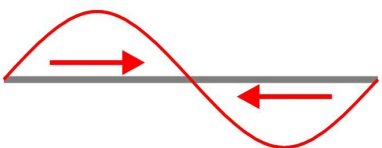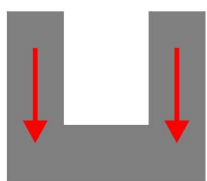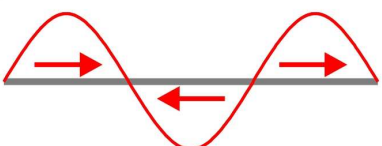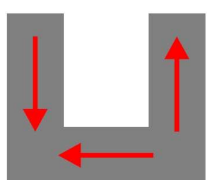
Figure 2.5: Analogy of (a)-(c) the oscillation modes of a straight antenna and (d)-(f) the three important resonances of a Split-Ring Resonator. The SRR modes are labelled according to our naming convention.

Chapter 3

Experimental methods

During the last two decades, a broad range of methods for the fabrication and characterization of Photonic Crystals, metal nanoparticles, and more recently also photonic Metamaterials has been developed and applied (see, e.g., [30, 65, 90–95] on these vast topics). In this chapter, we give the details of those methods that we use for the experiments presented in chapters 7 and 9.

The sample fabrication process, which applies to both Metallic Photonic Crystal Slabs and photonic Metamaterials, is summarized in section 3.1, explaining for example how gold is structured with 5-nanometer precision by electron-beam lithography. After the fabrication, we always investigate first the linear-optical properties of our samples, and later their nonlinear properties. The setups for measuring the linear transmittance are described in section 3.2. For the measurements of Second- and Third-Harmonic Generation, we use one of two pulsed laser sources (see section 3.3) providing the required high intensities.

3.1 Sample fabrication

The fabrication of samples containing high-quality nanostructures requires high-resolution methods [93, 94] which assure cleanness, purity and reproducibility. On top of a substrate, structuring of materials is achieved in three dimensions: Layers of materials with thicknesses between 5 nanometers and several micrometers are obtained by thin film deposition, whereas lateral structuring is achieved by a lithographic step. The former process is performed by electron-beam evaporation (section 3.1.1), and the latter by electron-beam lithography (section 3.1.2). The complete sample preparation procedure is summarized in section 3.1.3. Relevant material parameters are given along the way.

3.1.1 Thin-film evaporation

Thin films can be deposited on a substrate by various methods, including thermal evaporation, electron-beam evaporation, sputtering, and chemical vapor deposition. Among these, electron-beam evaporation is the most suitable method for our needs, since it is relatively

simple, allows to deposit metals as well as dielectric materials, and produces very homogeneous films. The source material, residing in a cooled crucible, is heated locally by a focussed electron beam, resulting in a directed beam of evaporated material consisting of small clusters. On the substrate located in the direction of the material beam, an amorphous, isotropic film is formed over time by condensation. In particular, the film is homogeneous on scales of optical wavelengths. Its thickness can be controlled with Angstrom precision by monitoring the material flux and by additionally controlling the flux to the substrate by a shutter opened for a programmed time. The whole process takes place under high vacuum conditions.

We use an electron-beam evaporation setup[1] with a high vacuum of 1×10^{-6} mbar before evaporation. A rotary holder with several crucibles allows to deposit a sequence of materials without breaking the vacuum. The substances which can be evaporated are, among many others, gold (Au), magnesium fluoride (MgF_2), indium-tin oxide (ITO), and hafnium dioxide (HfO_2). Typically, a deposition rate of 0.2, 1.0, 0.1, and 0.5 nm/s is used for the four substances, respectively. The latter two substances, ITO and HfO_2, are evaporated in an oxygen atmosphere of 1.2×10^{-5} mbar and 1×10^{-4} mbar, respectively, to increase the oxygen content within the layer. These two substances additionally require, directly after their evaporation, to be tempered at $450\,°C$ for 4 hours in a programmable oven[2] under ambient atmosphere to obtain the oxygen content for the right stoichiometry and final optical properties.

Gold is used primarily because it is a very good conductor up to optical frequencies, and additionally does not degrade when the sample is exposed to air for months (as opposed to, e.g., silver). Thus, the optical experiments have been highly reproducible with the same sample over a long time range. The other three substances mentioned above are dielectrics with different refractive indices ($n_{MgF_2}{=}1.38$, $n_{ITO}{=}1.9$, $n_{HfO_2}{=}1.95$) and are employed because of this property, e.g., to form a waveguide (cf. section 2.4). ITO, which is transparent for optical wavelengths from the infrared to ultraviolet, peculiarly is conductive for DC currents. Thus, ITO is perfectly suited for our purposes, since we need a conducting layer for subsequent electron-beam lithography. For a typical layer thickness of 5 nm, it does not impair the optical properties of the samples, which is crucial for our experiments. Additionally, ITO serves as an adhesion promoter for gold, which does not stick to bare glass very well. Furthermore, also HfO_2 is transparent for optical wavelengths longer than $0.21\,\mu m$ (photon energies smaller than 5.9 eV). For completeness, the refractive index of the quartz glass (suprasil) substrates is $n_{glass}{=}1.5$, and we describe air by $n_{air}{=}1$.

3.1.2 Electron-beam lithography

Electron-beam lithography (EBL) [96] is a versatile method to define a nanoscale 2D mask pattern. The method is based on a scanning-electron microscope (SEM) of which the electron-beam deflection unit is controlled by a computer providing the pattern from a CAD software.

---

[1]evaporation source e-vap 4000-UHV, MDC Vacuum Products Corp., USA, and deposition controller STC-200/SQ, Sycon Instruments, USA

[2]MTF 12/38/400, Carbolite Co., Great Britain

The beam is switched on and off and is moved to specific locations on the sample substrate which shall be exposed with electrons. A thin layer of organic resist susceptible to irradiation with electrons is located on the substrate, and the exposed areas of the resist can later be selectively removed.

We use the EBL system[3] at the Institute of Nanotechnology at the Forschungszentrum Karlsruhe. The SEM[4] is used with an acceleration voltage of $10\,kV$ and an aperture of $20\,\mu m$ resulting in an average beam current of $90\,pA$. Moreover, the SEM is equipped with a fast beam blanker allowing for minimal dot exposure times of $0.4\,\mu s$. Various simple shapes and patterns as defined in the CAD software[5] can be exposed: dots, lines, and rectangles (by a meandering beam spot), as well as composites of these (three rectangles form a Split-Ring-Resonator shape, cf. Fig. 2.5) and arrays consisting of many identical structures (e.g., a 1D lattice of lines or a 2D lattice of SRRs). For each geometric element, the exposure dose or dwell time can be assigned in the software. The magnification of the SEM determines both scanning resolution and write-field size, i.e., the scale which can be addressed by deflecting the electron beam alone, without moving the motorized sample stage. We mostly use a magnification of 1800 resulting in a scanning resolution of $7.5\,nm$ and a write-field size of $(100\,\mu m)^2$.

Before exposure, the substrate has to be prepared. First, a 5-nm-thick film of conductive ITO is evaporated and tempered. Later, it drains the electrons of the writing beam and avoids local charging of the sample. Second, a thin layer of the standard positive resist poly-methyl-methacrylate (PMMA)[6] is deposited from solution by spin-coating[7] at $5000\,rpm$ for $90\,s$. After $30\,min$ of post-bake at $165\,°C$ for polymerization, a PMMA film thickness of about $150\,nm$ results. Upon exposure with high-energy electrons, chemical bonds of the long polymer chains break up. In all areas where the local charge dose exceeds the sensitivity threshold of $175\,\mu C/cm^2$, the resist can subsequently be removed, during $20\,s$ in a wet developer consisting of a mixture of methyl-isobutyl-ketone (MIBK) and isopropanol in a volume ratio of 1:3.

The result is a polymer mask with holes at the exposed areas, the holes having certain desired shapes and locations. The above mentioned lithography system allows to define structures with minimal feature sizes of about $25\,nm$ and with an accuracy of about $5\,nm$. The resolution is not primarily determined by the beam spot size, but rather limited by electrons scattered from the substrate, effectively exposing nearby regions as well (proximity effect). However, electron-beam lithography yields reproducible and accurate results. The disadvantage of the method is the sequential processing (one area is exposed after another) leading to long exposure times of up to 5 hours.

---

[3]Raith GmbH, Germany

[4]LEO 1530, LEO Electron Microscopy Inc., now Carl Zeiss NTS GmbH, Germany

[5]ELPHY Plus version 1.233, and later, version 3.0 SP8, Raith GmbH, Germany

[6]PMMA 950k A4, MicroChem Corp., USA

[7]Spinner version 1.4, Reinraumtechnik Lanz, Germany

(a)

ITO

Glass

(b)

PMMA

Spin coating

(c)

e⁻

E-beam writing

(d)

Development
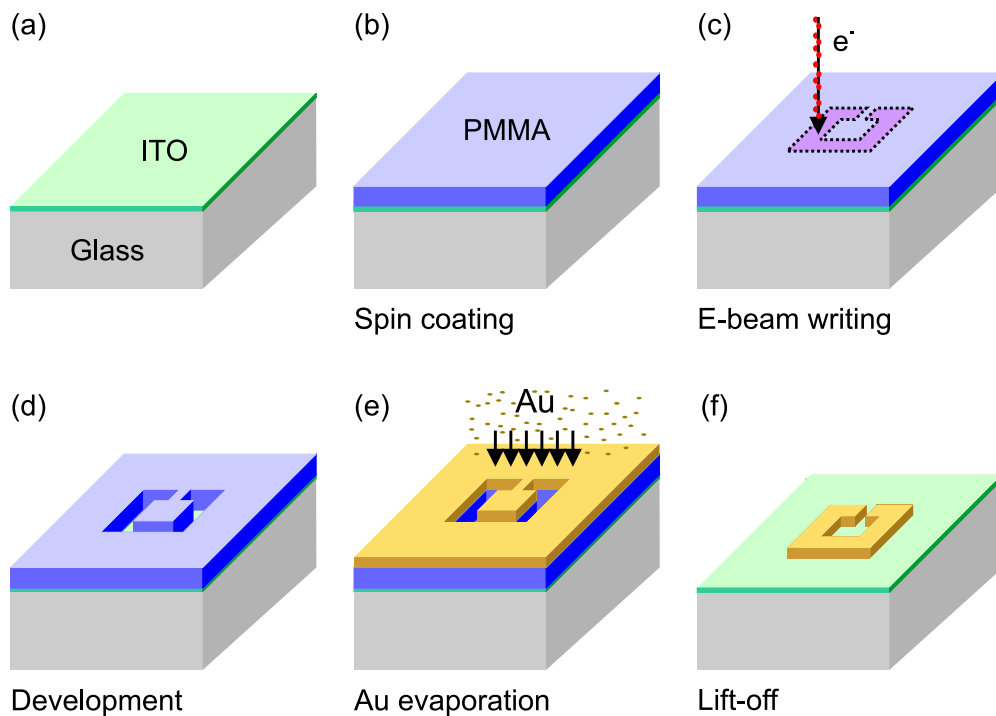
(e)

Au

Au evaporation

(f)

Lift-off

Figure 3.1: Summary of the most important steps of sample fabrication (see text). Taken from [22].

3.1.3   Sample fabrication overview

While thin-film evaporation and electron-beam lithography are the key methods to fabricate our nanoscale photonic materials, a lot of more aspects are relevant to obtain high-quality samples. Here, we summarize the details.

We start with a bare glass substrate,[8] which has a surface area of $10\,\text{mm} \times 10\,\text{mm}$ and a thickness of $1\,\text{mm}$. A specific scratch is applied to the back side of the substrate to distinguish it from the prepared front side which by eye looks identical during many of the following steps.

The substrate is cleaned mechanically with lens paper and acetone, is then rinsed with acetone, and is subject to an ultrasonic bath in acetone for $3\,\text{min}$. After that, it is rinsed again with acetone and resides in a sequence of an acetone bath and isopropanol bath for $30\,\text{s}$ each. The cleaning process is finished after dry-blowing with nitrogen, resulting in a surface which is free of dust, dirt, and fat.

The next step is the evaporation of one or several dielectric layers. For the Metamaterial samples, only ITO is used. For the Metallic Photonic Crystal Slab samples (cf. also section 7.1), a sequence of HfO_2, MgF_2, and ITO is used. After evaporating a layer which requires further oxidation, the evaporation sequence is interrupted, the sample is tempered and cleaned afterwards with the above procedure, before continuing with the next step. So far, the intermediate result is a substrate with unstructured dielectric layers, ITO being on top [see Fig. 3.1(a) for the case of Metamaterials].

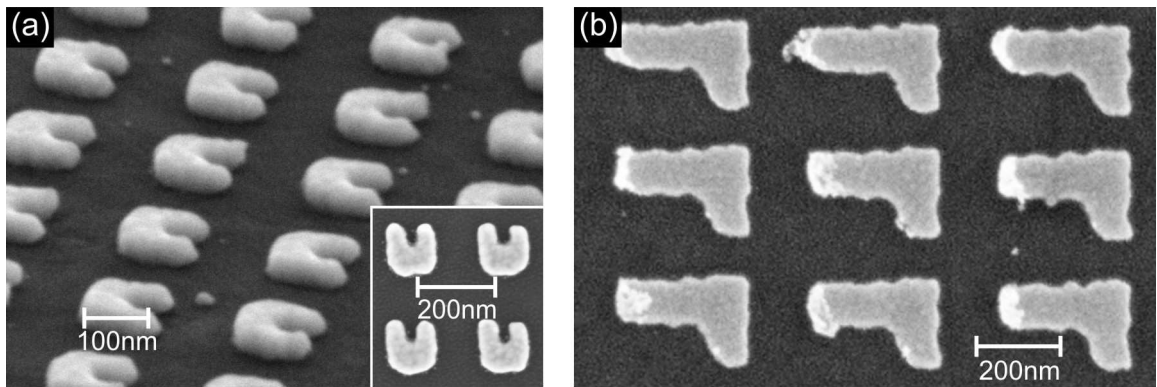[8]Suprasil 1, B. Halle GmbH, Germany

Figure 3.2: Examples of fabricated structures with high and low quality. (a) Oblique-view scanning electron micrograph of the smallest Split-Ring-Resonator structures we have fabricated. Note that all features of the shape are rounded off, due to the fabrication processes. The inset shows a top-view micrograph. (b) Top-view SEM image of gold structures with undesired defects, seen as the bright areas.

After spin-coating the substrate with PMMA [Fig. 3.1(b)], the sample is ready for electron-beam lithography, (c), and subsequent development, (d). After that, gold is evaporated with a typical thickness of 15–50 nm, (e). Most of the gold remains on top of the resist, but through the holes in the resist, gold is also deposited with the same thickness onto the substrate. Then, the resist and the gold on top of it are removed by a lift-off process, (f), in a hot acetone bath at 50 °C for 2 min and subsequent rinsing in acetone. Another cold acetone bath and isopropanol bath for 30 s each and dry-blowing with nitrogen completes the sample fabrication procedure. The result is a sample with several arrays consisting each of identical gold nanoparticles, on top of a dielectric substrate.

It is crucial to test whether a fabricated sample is suitable for experiments at all, since contaminations or failure of one of the above processes can render a sample useless. The homogeneity of the gold particle arrays and the cleanness are checked with a light microscope. The actual geometry of the gold structures must be checked with an electron microscope. For example, planar Split-Ring Resonators are shown in Fig. 3.2(a) in an oblique-view SEM picture. From such oblique-view SEM pictures we know that in some cases (especially when using an almost-too-low exposure dose during lithography), gold structures which stand off the substrate, with spikes perpendicular to the surface, are produced in error. These are probably caused by ripping off the gold from the substrate during lift-off. Such spikes or other 3D structures can be seen in top-view SEM pictures as bright spots or areas [see, e.g., Fig. 3.2(b)]. In linear-optical and, even more importantly, in nonlinear-optical experiments, these 3D structures constitute "hot spots" of extremely high electromagnetic fields (lightning-rod effect) and can result in systematic errors and misinterpretations. We emphasize that our samples investigated in chapters 7 and 9 are accurate, planar gold structures which do not contain systematic "hot spots." Neither do we observe macroscopic or microscopic inhomogeneities of the evaporated dielectric films.

We additionally point out that the oblique-view SEM picture in Fig. 3.2(a) also reveals that the corners and edges of our fabricated gold structures are actually not straight, but rounded off.

3.2   Linear-optical characterization tools

Linear-optical spectroscopy of a given sample reveals whether resonances appear at certain wavelengths. Usually, when light is incident on a sample in resonance, increased absorption and reflection (and scattering) occurs, effectively decreasing the transmitted light, compared to non-resonant radiation. Hence, measuring the transmittance gives us important information about the linear-optical properties.

All transmittance measurement setups presented in the following have in common that white light from a halogen lamp is transmitted through a sample and is then spectrally resolved. Since a single substrate often contains several sample areas, i.e., different 2D arrays each consisting of identical nanoparticles, the detected light must be restricted to those rays which traversed a certain limited area on the sample surface. This is achieved by focussing the white light onto the substrate, and by using small apertures which effectively "cut out" all undesired parts of the sample. The spectrum can be measured on one hand for light transmitted through the gold structures, dielectric layers, and the glass substrate, and on the other hand for light transmitted through the same dielectric layers and glass substrate without gold. The ratio of the two, computed for each wavelength, is called the transmittance spectrum. Alternatively, the extinction can be specified, which is defined as the negative natural logarithm of the transmittance.

Two powerful tools are presented here in detail: a commercial Fourier-transform infrared spectrometer which allows for fast and simple transmittance measurements for visible and up to mid-infrared wavelengths, and a home-built setup which allows to use wavelengths up to the near infrared and to perform angle-resolved measurements with a small numerical aperture.

3.2.1   Fourier-transform infrared spectrometer

The ready-at-hand solution for transmittance measurements is a Fourier-transform infrared (FTIR) spectrometer[9] with an attached optical microscope.[10] It can operate for shorter wavelengths ($0.4 - 1.2 \, \mu m$) with a quartz beam splitter and a silicon detector, and for longer wavelengths ($0.9 - 5.0 \, \mu m$) with a calcium-fluoride beam splitter and a indium-antimonide detector cooled by liquid nitrogen. Small sample areas between $8 - 100 \, \mu m$ in diameter can be investigated. A polarizer allows to excite the nanostructures with light of a defined linear polarization.

Importantly, the light is focussed and collected with Cassegrain lenses (reflective microscope objectives) with a numerical aperture of 0.5, or more precisely, the sample is illuminated from all directions between $15° - 30°$ off the substrate normal [22]. Since most of the resonant phenomena investigated in this thesis are (slightly) angle-sensitive, the use of Cassegrain lenses results in transmittance spectra with slightly broadened and less pronounced peaks and dips, compared to the other setups below.

This setup is used for the linear-optical measurements presented in section 9.2.

---

[9]Bruker Equinox 55, Bruker Optik GmbH, Germany
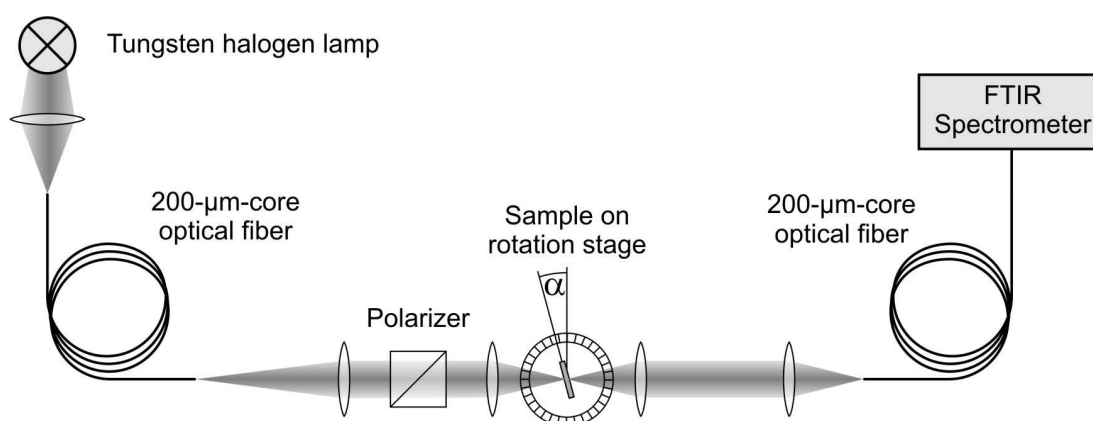[10]Bruker Hyperion 1000, Bruker Optik GmbH, Germany

Figure 3.3: Schematics of the setup for angle-resolved linear transmittance measurements. Adapted from [22].

3.2.2 Home-built transmittance setups

The first of our two home-built transmittance setups has a small numerical aperture of 0.088, and additionally allows for angle-resolved measurements [48]. It is schematically shown in Fig. 3.3. Light from a halogen lamp is sent through a Glan-Thomson polarizer and focussed with a microscope objective onto the substrate, with an effective opening angle of $\pm 5°$. The sample position can be adjusted by a 3D micrometer stage, and its angles (with respect to the incident light) by two goniometers and a $360°$-rotation stage. For rotation in the other direction, the sample has to be turned by 90 degrees (and the polarizer correspondingly). The light transmitted through the sample can be limited by a rectangular knife-edge aperture (not shown) down to a size of about $10\,\mu$m and can either be viewed with a camera or coupled into an optical fiber attached to a home-built FTIR spectrometer (a piezo-controlled Michelson interferometer with a liquid-nitrogen-cooled indium-antimonide detector). Thus, transmittance spectra can be measured for wavelengths between $0.5 - 2.2\,\mu$m and variable angles of incidence of up to $\pm 60°$. All angle-resolved transmittance spectra are normalized to the oblique substrate. This setup is used for the linear-optical measurements presented in section 9.3.1.

The second home-built setup (chronologically the earlier one) used for the measurements of section 7.2 works the same way but is slightly simpler. A commercial white light source[11] is used, and the polarized light is focussed with a numerical aperture of 0.025 to a 50-μm spot diameter, which is smaller than the investigated sample areas. The transmitted light is sent through an optical fiber and detected by an optical spectrum analyzer[12] in the wavelength range $0.55 - 1.75\,\mu$m.

---

[11] Ando AQ-4303B, Ando Electric Co. Ltd., now Yokogawa Electric Corp., Japan
[12] Ando AQ-6315B, Ando Electric Co. Ltd., now Yokogawa Electric Corp., Japan
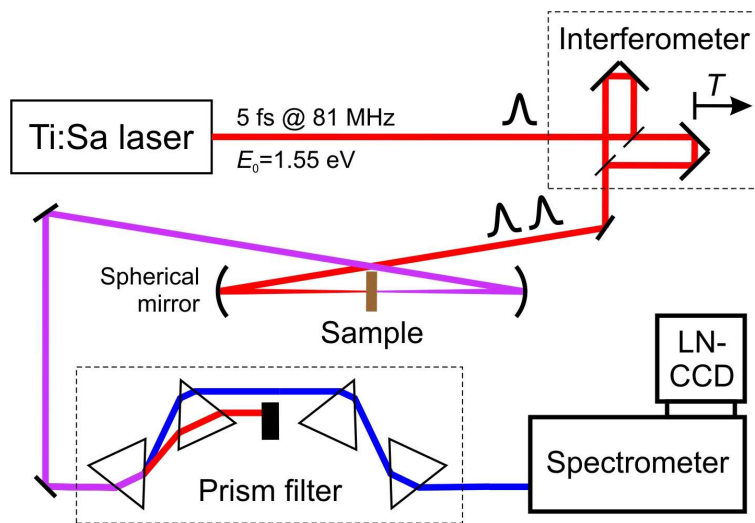
Figure 3.4: Setup for the THG experiments with Metallic Photonic Crystal Slabs (section 7.3).

3.3 Nonlinear-optical characterization setups

Nonlinear-optical experiments require excitation with high electromagnetic fields to obtain a detectable nonlinear signal strength (cf. section 2.2.1). High intensities are usually obtained from pulsed lasers providing light pulses of a certain temporal length and repetition frequency. For a certain average power, the lower the duty cycle, the higher the nonlinear signals. We use two systems, a titanium-sapphire (Ti:Sa) laser providing 5-fs pulses (section 3.3.1) and an optical parametric oscillator providing 170-fs pulses (section 3.3.2), each at a repetition frequency of about $81\,\mathrm{MHz}$ ($\approx 1/12\,\mathrm{ns}$). The two systems differ not only in pulse length and spectral width, but also in center wavelength and the ability for time-resolved measurements of the Ti:Sa setup.

Additionally, high intensities are achieved by focussing. The sources described below provide coherent and parallel light with a Gaussian lateral beam profile. Behind a lens or a spherical mirror, the light wave converges according to Gaussian beam optics [97] to a small area described by the beam waist (spot radius, $1/\mathrm{e}^2$ radius of the Gaussian intensity profile).

3.3.1 5-fs titanium-sapphire laser setup

The Ti:Sa laser delivering pulses of $5\,\mathrm{fs}$ length is used for the time-resolved spectroscopy experiments on THG presented in section 7.3. The laser shall only be described briefly here, details can be found in [16, 98]. Essentially, it is a Kerr-lens mode-locked laser with a broad-band-amplification Ti:Sa crystal and highly sophisticated methods to compensate for the dispersion of all amplified frequencies. For this purpose, prisms and doubly-chirped (dielectric) mirrors are used inside the laser cavity and externally. The laser delivers polarized pulses with a duration corresponding to about two optical cycles, at a carrier wavelength of about $0.8\,\mu\mathrm{m}$ (about $1.55\,\mathrm{eV}$ photon energy), and an average output power of around $170\,\mathrm{mW}$ (during a pulse, the power is hence a factor of $12\,\mathrm{ns}\,/\,5\,\mathrm{fs} \approx 2{\times}10^6$ higher).

The overall experimental setup is shown in Fig. 3.4. The pulses from the Ti:Sa laser are sent into a piezo-controlled Michelson interferometer to obtain two identical pulse copies. These can interfere, as long as the time delay T between them is not larger than the pulse length. The copropagating pulses with 80 mW maximal average power are focussed [31] with a spherical silver mirror (f=100 mm) onto the sample, guaranteeing a small numerical aperture of 0.025 and normal incidence. The beam waist at the sample position (measured with a knife-edge technique) is 13 μm and much smaller than the 60-μm-wide sample areas. We estimate a peak pulse intensity on the samples of 4×10^{10} W/cm^2 [31]. The transmitted light is collected by a spherical aluminum mirror (f=100 mm) and the optical third harmonic is separated from the overwhelming fundamental light by means of four fused-silica Brewster-angle prisms. The THG is spectrally resolved using a grating spectrometer[13] (with a grating blazed at 0.25 μm wavelength), and detected by a UV-sensitive, liquid-nitrogen-cooled CCD camera.[14] The whole experiment is controlled by a LabView interface which allows to automatically acquire many CCD spectra for a range of interferometric time delays. With this method, we can investigate the different quasi-temporal behaviors of different spectral components of THG from the sample (see section 7.3).

By means of the interferometer, also the laser pulses themselves can be characterized, either at the sample position or at an equivalent position. Placing a phase-matched beta-barium borate (BBO) crystal into the focus and detecting the SHG intensity by a photomultiplier tube allows to measure the usual second-order interferometric autocorrelation (SHG-IAC) shown in Fig. 3.5(a). Alternatively, replacing the sample by a sapphire plate and detecting the generated THG intensity yields the third-order interferometric autocorrelation (THG-IAC)[see Fig. 3.5(b)]. The latter can be viewed as the apparatus function and shows the high temporal resolution of our time-resolved THG measurements shown in detail in section 7.3.

In this context, the nth-order interferometric autocorrelation (IAC) function is the nth-harmonic intensity measured by a slow detector averaging over the interfering pulses, thus described as

$$I_{\text{IAC}}^{(n)}(T) = \int_{-\infty}^{\infty} \mathrm{d}t \left[\left\{ E(t) + E(t - T) \right\}^2 \right]^n \Bigg|_{n\text{th harmonic}}. \tag{3.1}$$

For large interferometric time delays T, the two pulse copies do not interfere, and $I_{\text{IAC}}^{(n)}(T)$ is a constant, which we normalize to 1. Is is easy to see that the values of $I_{\text{IAC}}^{(n)}(T = 0)$ for n=1, 2, and 3 must then be 2, 8, and 32. The ratio of 8:1 for the SHG-IAC can be seen in Fig. 3.5(a), and that of 32:1 for the THG-IAC in Fig. 3.5(b), also confirming a good alignment of the interferometer in the experiment.

Figure 3.5(c) shows the broad field spectrum of the laser pulses. Assuming a flat spectral phase and taking the Fourier transform of (c) leads to a first approximation of the pulse electric field $E(t)$. The SHG-IAC and THG-IAC calculated from this field [thin lines in (a) and (b), respectively] match very well the experimental IACs, proving that the pulses are nearly transform-limited, i.e., have negligible residual chirp (see also [16]).

---

[13] HR460, Jobin-Yvon, France
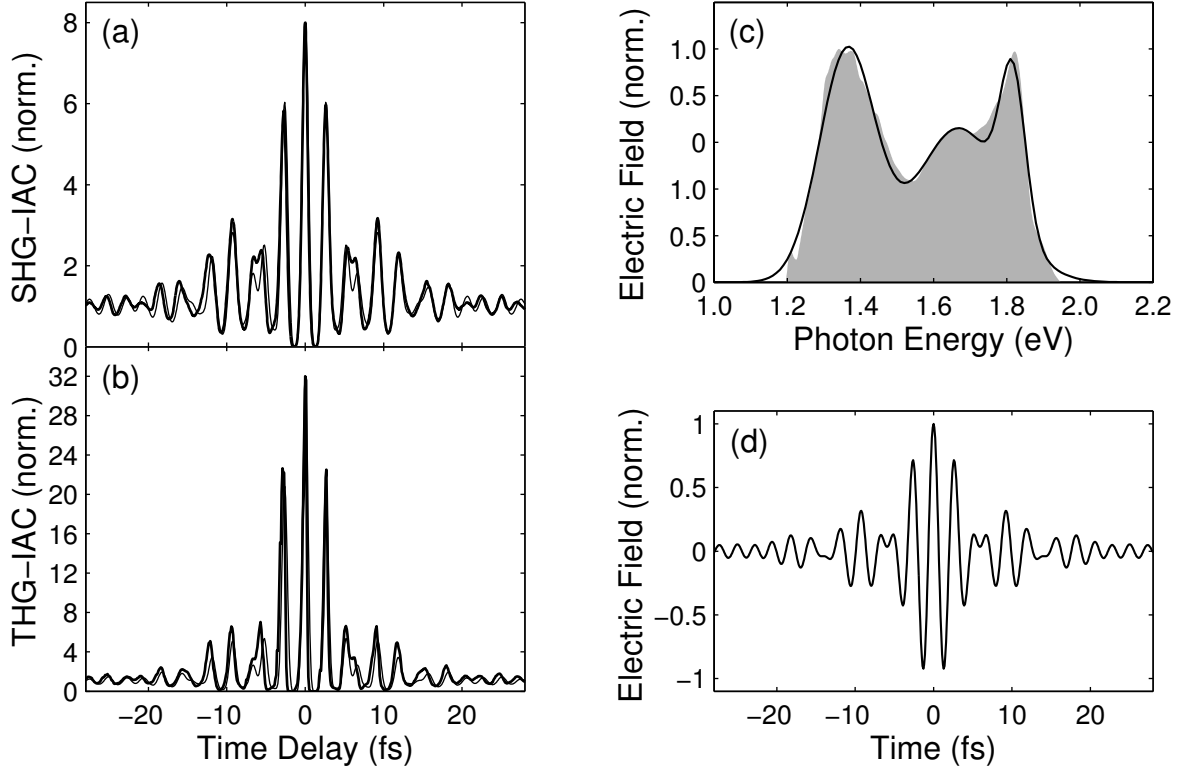[14] LN/CCD-1340/100EB, Roper Scientific, USA

Figure 3.5: Characterization of the 5-fs laser pulses. (a) Second-order interferometric autocorrelation (SHG-IAC) measured directly (thick line) and calculated (thin line) from the measured pulse spectrum under the assumption of a flat spectral phase. (b) Third-order interferometric autocorrelation (THG-IAC) measured directly (thick line) and calculated (thin line) in analogy to (a). (c) The gray area depicts the electric field spectrum (square root of measured intensity spectrum) of the pulses, the line is the fit of Eq. (3.2). (d) Temporal evolution of the pulse electric field as computed from Eq. (3.3).

To describe a single laser pulse a little bit more analytically, we apply a second approximation by expressing the electric field spectrum in Fig. 3.5(c) with the sum of 3 Gaussians

$$\tilde{E}(\omega) \propto \sum_{i=1}^{3} \hat{E}_i \, e^{-(\omega-\omega_i)^2/\sigma_i^2} , \tag{3.2}$$

where $\hat{E}_2/\hat{E}_1=0.67$, $\hat{E}_3/\hat{E}_1=0.65$, $\hbar\omega_1=1.36\,\text{eV}$, $\hbar\omega_2=1.67\,\text{eV}$, $\hbar\omega_3=1.82\,\text{eV}$, $\hbar\sigma_1=0.11\,\text{eV}$, $\hbar\sigma_2=0.17\,\text{eV}$, and $\hbar\sigma_3=0.048\,\text{eV}$. In the time domain, this corresponds to

$$E(t) \propto \sum_{i=1}^{3} \hat{E}_i\sigma_i \, e^{-\sigma_i^2 t^2/4} \cos(\omega_i t) . \tag{3.3}$$

This electric field pulse, depicted in Fig. 3.5(d), is used for the calculations in section 6.2.

3.3.2   170-fs optical parametric oscillator setup

The optical parametric oscillator (OPO) is used for the SHG and THG experiments presented in chapter 9. It provides coherent Gaussian pulses at a center wavelength of $1.5\,\mu\text{m}$ and a
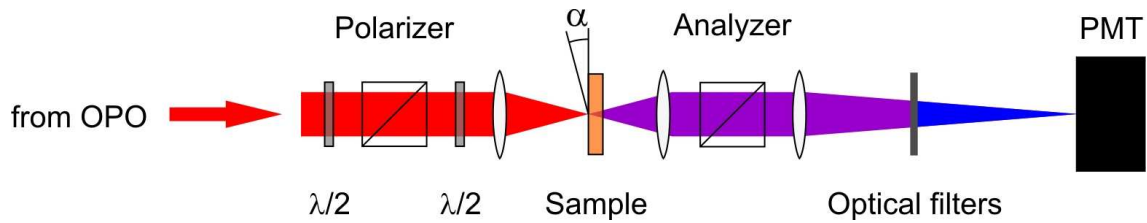
Figure 3.6: Setup for the SHG and THG experiments with photonic Metamaterials (chapter 9).

pulse length of about 170 fs, thus, each pulse contains many cycles of light. Compared to the short decay time of plasmon oscillations of typically below 10 fs (cf. section 2.3.1), these pulses can be considered as a harmonic (i.e., single-frequency) excitation for a certain time span.

The OPO[15] draws its optical power from a Ti:Sa laser[16] which provides pulses of about 120 fs duration at 0.81 μm wavelength and 2.1 W average power. The Ti:Sa laser itself is pumped by a power of 11 W from a frequency-doubled Nd:Vanadate laser.[17] The OPO output is filtered by a 5-mm-thick silicon crystal to suppress all optical products except the pulses at 1.5 μm, yielding an average output power of about 180 mW.

The experimental setup is shown in Fig. 3.6. Since the OPO delivers linearly polarized light pulses, a combination of a first half-wave plate[18] and a polarizer[19] is used to adjust the excitation intensity and to assure the polarization at the entrance of the setup. The reflection of the incident light at a oblique glass plate (not shown) is focussed onto a germanium diode to measure the linear intensity for reference. The light transmitted through the glass plate passes a second half-wave plate to adjust the polarization of the pulses without changing the following beam path. Typically, 50 mW of average power (or 10 – 90 mW power for intensity variations) are focussed onto the sample by a borosilicate lens (f=100 mm). The focus beam waist is 32 μm, the Rayleigh length [97] is 1800 μm, and the numerical aperture is 0.018, as measured with a knife-edge technique. For 50 mW average excitation power, we estimate the pulse peak intensity and electric field strength on the sample to 4×10^7 W/cm^2 and 2×10^7 V/m, respectively.

The sample position can be adjusted by a 3D translation stage, and two of its angles by goniometers and the third by a 360°-rotation stage. The sample can be tilted in the other direction after turning the sample by 90° and the second half-wave plate by 45° around the optical axis of the setup. The samples investigated in chapter 9 have areas of $(100 \, \mu m)^2$, which is large compared to the beam diameter, even for angles of incidence of ±60° (the tails of the Gaussian lateral intensity profile can be neglected, especially in nonlinear optics). In the sample, the incident light pulses generate an optical second harmonic and/or third harmonic. All light radiated into the forward direction (transmitted through the sample) is

---

[15] Opal, Spectra Physics, USA

[16] Tsunami, Spectra Physics, USA

[17] Verdi V18, Coherent Inc., USA

[18] 1450nm λ/2 Mica, B. Halle GmbH, Germany

[19] Glan-Laser 03PGL301, Melles Griot, USA

spectrally filtered by means of optical glass filters and detected by a photo-multiplier tube[20] (PMT). For measuring SHG, the optical filters are $6\,\mathrm{mm}$ of BG3 and $3\,\mathrm{mm}$ of RG715 (for THG, only $6\,\mathrm{mm}$ of BG39), effectively suppressing all undesired optical frequencies, i.e., the fundamental and the other nonlinear products. Optionally, an analyzer can be placed into the beam path in front of the PMT to determine the polarization of the emerging harmonic wave. When measuring samples at increasing oblique angles, the 3D position of the sample area is realigned, and also the collecting lens in front of the PMT is adjusted to correct for the different beam path (caused by the 1-mm-thick glass substrate of the sample).

The PMT operated with a cathode voltage of $1.1\,\mathrm{kV}$ is connected to a resistor of $1\,\mathrm{M\Omega}$ and to a lock-in amplifier.[21] The beam from the OPO is chopped by a 10-segment chopper wheel (not shown) with a frequency of $400\,\mathrm{Hz}$. This lock-in method dramatically increases the signal-to-noise ratio. The lock-in amplifier is used with an integration constant of $1\,\mathrm{s}$ and displays the final observable, i.e., a voltage in millivolts or microvolts, which is directly proportional to the respective nonlinear intensity.

With the above values, and knowing that the quantum efficiency of the PMT for SHG (THG) at $0.75\,\mathrm{\mu m}$ ($0.5\,\mathrm{\mu m}$) wavelength is $10\,\%$ ($18\,\%$), we will be able to estimate the absolute conversion efficiency of linear intensity to nonlinear intensity in section 9.2.2 (9.2.4).

---

[20]R636-10, Hamamatsu Photonics, Japan
[21]SR830, Stanford Research Systems, USA

Chapter 4

Numerical methods

For the mathematical description of our optical materials, one has to solve the Maxwell equations and take into account the material permittivities (and maybe permeabilities) for linear optics. In recent years, a variety of commercial software products has become available to perform this task in detail for materials with a given geometry. We use the FEMLAB (now Comsol Multiphysics)[1] package to simulate photonic Metamaterials.

It is a central question of numerics whether numbers and other results calculated by such software packages are accurate and significant at all; that is, whether the convergence of the results has been achieved. Various issues can arise on the long way between the (often very general) methods of a software package and a resulting number. Estimating the badness of these issues requires profound knowledge of the methods and their limitations, knowledge which often only specialists of numerics possess.

Although we are not specialists, we claim convergence for our numerical results presented in chapter 8. Thus, the present chapter describes how we have carefully considered the numerical issues which can arise when solving the 3D vector Maxwell equations with FEMLAB (section 4.1). Convergence is claimed not only for transmittance values in linear optics, but also for values associated with nonlinear near-fields which are even more critical. Especially the accurate description of electromagnetic near-fields in and around metals in three dimensions turns out to be challenging.

We briefly note that in the other two theory chapters 5 and 6, we employ the MATLAB[2] environment for relatively simple calculations in which the question of convergence is not critical.

4.1   Solving the 3D Maxwell equations with FEMLAB

Since its start in 1986, FEMLAB has become an established solution for simulations in both scientific and industrial applications. The software package solves partial differential equations of second order in one, two, or three spatial coordinates. The static or time-dependent problems can include physical systems involving electromagnetics, structural mechanics,

---

[1]Comsol Multiphysics version 3.2a, Comsol AB, Sweden
[2]MATLAB version 7.1, The Mathworks Inc., USA

fluid dynamics, thermodynamics, and many more. The numerical solution is computed using the finite element method [99–101], which has been developed since the 1940s [102, 103].

We employ this software for the simulations of Metamaterials of which the results are presented in chapter 8. Here, we give an (incomplete) overview of the methods FEMLAB [104] uses to solve 3D electromagnetic wave problems in the frequency domain. Most importantly, we discuss critical issues which potentially arise, and explain our procedures circumventing them. The following paragraphs are a more general description, while details relevant for our calculations are given in section 4.1.1.

We anticipate to mention that we use FEMLAB first to solve for the linear-optical fields only, whereas we compute nonlinear quantities subsequently within postevaluation (see below) on the basis of the linear-optical fields.

Differential equations

For the time-harmonic case[3] with the fixed frequency ω_0, the electric field is $\tilde{\boldsymbol{E}}(\boldsymbol{r}, \omega) = \hat{\boldsymbol{E}}(\boldsymbol{r})\delta(\omega - \omega_0)$, and the partial differential equations under consideration are [104]

$$\nabla \times \nabla \times \hat{\boldsymbol{E}}(\boldsymbol{r}) - \frac{\omega_0^2}{c_0^2}\varepsilon(\boldsymbol{r})\hat{\boldsymbol{E}}(\boldsymbol{r}) - \nabla\hat{\Psi}(\boldsymbol{r}) = 0, \qquad (4.1a)$$

$$\varepsilon_0 \nabla \cdot \left\{ \varepsilon(\boldsymbol{r})\hat{\boldsymbol{E}}(\boldsymbol{r}) \right\} = 0, \qquad (4.1b)$$

which are the wave equation (2.18) appended by a Lagrange multiplier $\hat{\Psi}(\boldsymbol{r})$ and an additional equation requiring that the field $\varepsilon(\boldsymbol{r})\hat{\boldsymbol{E}}(\boldsymbol{r})$ be divergence-free (i.e., we assume no free charges). The variable $\hat{\Psi}(\boldsymbol{r})$ and the second equation are included as usual in order to enhance the numerical stability [104]. Both the independent variable, $\boldsymbol{r}$, and the dependent variables, $\hat{\boldsymbol{E}}$ and $\hat{\Psi}$, are subject to approximations described in the following.

Tetrahedral mesh

The wave propagation is only considered inside a finite 3D volume. For Metamaterials, this calculation volume is a cuboid, and usually a part of the volume corresponds to air, another part to the glass substrate, and third part to a metal structure of a certain 3D geometry. The user has to define these geometry objects as the first step. (Later, these volumes can be assigned material parameters like permittivities.)

The spatial coordinate $\boldsymbol{r}$ now needs to be discretized. This is done by filling the whole calculation volume with irregular tetrahedra. Correspondingly, surfaces and interfaces are discretized by triangles (see Fig. 4.1). The mesh generator of FEMLAB allows to define regions of higher interest (e.g., the metallic structure) which can be filled with smaller tetrahedra than in other regions (e.g., in air far away from the metal), and a quasi-continuous size transition of tetrahedra between regions. The possibility of a selective local resolution is one

---

[3]We note that FEMLAB assumes a time dependence $e^{+i\omega_0 t}$ of fields, in contrast to the usual description in optics expressed by Eq. (2.16). Correspondingly, all values transferred between FEMLAB and equations of this thesis are applied a complex conjugation.
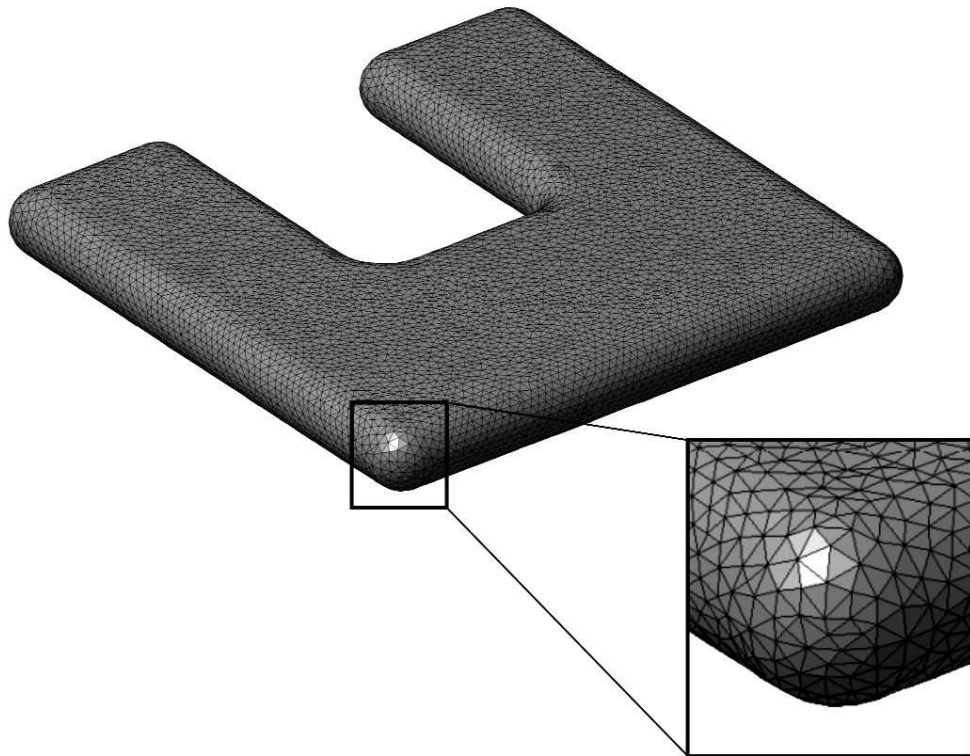
Figure 4.1: Mesh discretization. The example shows the air/metal interface mesh for a Split-Ring Resonator. The shown triangles are connected to some of the tetrahedra filling the metal, as well as to tetrahedra in the air volume (not shown for clarity). The straight edges approximate a geometric shape which is defined to be completely rounded off to avoid sharp corners and locally divergent fields.

of the key advantages of using a tetrahedral mesh. Another advantage is that virtually all geometric shapes can be approximated, in particular, round edges and surfaces. This avoids sharp bends and corners of $90°$ which are always present in the usual rectangular cartesian 3D grids (e.g., the stair-step grid of the finite-difference time-domain method [105, 106]). Sharp corners can lead to divergent local field strengths at metallic surfaces (lightning-rod effect). This can be very important for nonlinear-optical simulations.

Finite elements

The dependent variables can then be approximated within each tetrahedron individually. In the simplest case (called linear Lagrange element [99]), a scalar variable like $\hat{\Psi}$ can be described by a linear function of the space coordinates, e.g., $\hat{\Psi}(\boldsymbol{r}) := \hat{a}_0 + \hat{\boldsymbol{a}}_1 \cdot \boldsymbol{r}$, with $\hat{a}_0$ and $\hat{\boldsymbol{a}}_1$ as coefficients for each tetrahedron. However, a different assignment of appearing coefficients is favorable: Assigning each node in the complete mesh a certain value for $\hat{\Psi}$, the linear interpolation also guarantees the continuity of the variable $\hat{\Psi}(\boldsymbol{r})$ across tetrahedra. The values of Ψ at all node points are then the coefficients. The generalization for approximation with polynoms of higher order [99–101] is obvious.

Vector elements

The trickier part is the approximation of the vector field $\hat{\boldsymbol{E}}(\boldsymbol{r})$. We cannot describe each of the three vector components $\hat{E}_x, \hat{E}_y, \hat{E}_z$ by Lagrange elements since this would force normal components of $\hat{\boldsymbol{E}}$ to be continuous across material interfaces, which is generally incorrect.

However, if the permittivity $\varepsilon(\boldsymbol{r})$ is constant within each tetrahedron, a simple ansatz for a divergence-free vector field $\hat{\boldsymbol{E}}(\boldsymbol{r})$ is a field with a constant curl. In this case, the field can be described by $\hat{\boldsymbol{E}}(\boldsymbol{r}) := \hat{\boldsymbol{b}}_0 + \hat{\boldsymbol{b}}_1 \times \boldsymbol{r}$, with the components of $\hat{\boldsymbol{b}}_0$ and $\hat{\boldsymbol{b}}_1$ comprising six scalar coefficients in total. Again, a different assignment of coefficients is preferred: Each edge of the complete mesh is assigned one scalar degree of freedom, namely, the constant tangential part of the vector field along the direction of the edge. Inside each tetrahedron with its six associated edges, the field can then be interpolated. These so-called edge elements [99, 100] (or Whitney elements [107] or Nédélec elements [108–110]) assure from the ansatz functions that tangential fields are continuous across material interfaces.

It is important to note that, in contrast, normal components of fields across any tetrahedron boundary are subject to potential errors resulting from a poor space discretization or numerical convergence (see below).

For 3D wave propagation, FEMLAB offers the linear vector elements just described, or quadratic or cubic vector elements [108–110]. Note that (linear) vector elements are divergence-free inside each tetrahedron, but not necessarily on the interface between any two tetrahedra.

Direct and iterative solvers

With the fields $\hat{\boldsymbol{E}}$ and $\hat{\Psi}$ being described by many scalar coefficients distributed throughout the mesh, the differential equations (4.1) can be translated into difference equations, forming a large set of linear equations with the coefficients as unknowns. Typically, a 3D Metamaterials problem consists of about 10^4–10^7 unknowns, so the sparse matrix describing the set of linear equations cannot be inverted by simple methods but the set of equations has to be solved by sophisticated, specific solvers. The development of such solvers is a current topic of research in numerics (see, e.g., [111, 112]).

Solvers can be divided into two classes, direct ones and iterative ones. Direct solvers always lead to numerical convergence (see below) and are fast for small models of up to about 5×10^4 unknowns, but become slow and extremely memory-consuming for larger models. On our 8-gigabyte Linux machines,[4] we are able to process at most 2.2×10^5 unknowns with direct solvers. Iterative solvers, in contrast, use by far less memory and are often faster for large models, but numerical convergence is not always guaranteed. Moreover, the FEMLAB iterative solver best suited for 3D wave propagation problems requires a multigrid mesh hierarchy, i.e., a coarse mesh and a refined mesh containing all edges of the coarse mesh, or one mesh issued with vector elements of different orders. Defining such a mesh hierarchy is, however, not always possible (see next section). We are able to process at most 2×10^6 unknowns with iterative solvers.

---

[4]Sun Fire V20z Server, Sun Microsystems Inc., USA

Postevaluation

After solving, FEMLAB allows to use the computed coefficients to calculate the fields $\hat{E}$ and $\hat{\Psi}$ and virtually any analytic expression depending on them (magnetic field, intensity, nonlinear quantities etc.). This can be done, e.g., to visualize the vector field in an arbitrary plane, or integrate a derivative of the field over a certain volume, or integrate a nonlinear field component at the outside of a certain surface etc.

Convergence

For the simulation results to be meaningful at all, convergence must be ensured. There are two types of convergence. The first is the numerical convergence of solving the system of linear equations by a solver. The success can be seen from a number provided by the solver, and is always achieved for direct solvers. The second, more complicated type of convergence is associated with the question if the approximations by the mesh and the ansatz functions accurately describe the real continuum physics. For a mesh discretization with tetrahedra which are larger than relevant wavelengths, this is obviously not the case. More subtle issues and questions can appear, e.g., whether near fields or evanescent fields are well enough discretized, or whether absorbing boundaries actually do what they are designed for. In most cases, the second type of convergence cannot be put into a general number, and convergence of smooth fields and a specific observable or end result must be checked for validity by using a sequence of successively finer meshes and/or higher-order vector elements.

4.1.1 MKFEM: Modelling Metamaterials

While FEMLAB offers lots of tools to deal with numerical problems involving partial differential equations, its wideness and generalization makes it sometimes impractical to work with. Restricted to the most general case of 2D periodic Metamaterials, we have thus developed a set of our own library functions (called MKFEM, version 2.0) which enormously simplify the handling and retraceability of simulations with FEMLAB in the MATLAB environment. Using our library, for example, allows to express a simple model of Split-Ring Resonators excited with light under oblique incidence to simulate the transmittance with only about ten lines of MATLAB code.

All MKFEM library functions are provided with a detailed documentation available within the MATLAB Help context. Here, we summarize the most important parts of technical background on what is performed or assumed within the library functions, without going into the details of their usage again. Rather, we explain which aspects of numerics have carefully been taken into account for the simulations of which the converged results are presented within chapter 8.

Implementation of 2D periodic boundary conditions

The definition of 2D periodic boundary conditions in the x and y directions for both $\hat{E}$ and $\hat{\Psi}$ has to be expressed individually for each pair of corresponding surfaces, e.g., for

two boundaries of the substrate with surface normal parallel to x, and for two with surface normal parallel to y, the same for the air volume, for each perfectly matched layer (see below), etc. For each corresponding pair, FEMLAB requires the linear mapping of one surface onto the other, defined by specifying serval geometric points (FEMLAB numbers), and other information. The data substructure which describes periodic boundary conditions is a hierarchical, nested structure of different data types, consisting in total of 12 hierarchical levels and up to several thousands of entries. It is automatically generated by a MKFEM function after the user has defined all appearing geometry objects.

Moreover, the surface mesh on corresponding surfaces should be congruent (to avoid interpolation as an additional approximation). Unfortunately, FEMLAB does not offer this possibility since its version 3.0. Hence, we obtain the (coarsest) mesh from a combination of the FEMLAB mesh generator and the publicly available TetGen[5] mesh generator.

Realization of perfectly matched layers

For Metamaterials with small element-to-wavelength ratios and normal-incidence scenarios, it is sufficient in most cases to let the evanescent near fields decay along the extent of the substrate volume and air volume, respectively. For large ratios, or Photonic Crystals, as well as for Metamaterials with oblique incidence, one has to use special absorbing boundary conditions in the directions of transmission and reflection, namely so-called perfectly matched layers (PMLs) [113]. A PML is an extension of the calculation volume that can be described either as an anisotropic absorbing material [114], or alternatively as an extension into complex-valued space coordinates [115], in which normally propagating waves decay exponentially.

If the user sets a single flag, a MKFEM function automatically generates PMLs, in addition to already specified geometry objects. PMLs are defined with permittivities and permeabilities [omitted in Eq. (4.1a)] matching the corresponding adjacent physical volumes, with an absorbing contribution increasing linearly with distance. Care must be taken when using PMLs to adjust the absorption factor and PML lengths and discretization to assure convergence. Also note that only propagating modes are treated specially this way, evanescent modes entering a PML decay like in air or in the substrate. Due to the linear increase of material parameters inside the PMLs, their use generally only makes sense in combination with vector elements of quadratic or cubic order.

Plane-wave excitation

Excitation is always performed with a plane electromagnetic wave having a polarization (linear, circular, or elliptical) which has to be specified. For normal incidence, the wave propagates towards the $-z$ direction.

If no PMLs are present, the boundary conditions at the surfaces with power inflow ($z>0$) and outflow ($z<0$) do not only allow for the inward propagation of an exciting plane wave, but also outward propagating plane waves are allowed (absorbed) without reflections [104].

---

[5]TetGen version 1.4.0, http://tetgen.berlios.de (January 14, 2006)

Oblique incidence

Exciting the Metamaterial with a wave at oblique incidence is possible by specifying one or two Euler angles of rotation. The polarization vector and the propagation direction (the wave vector), specified for normal incidence, are both rotated as described by the angles. This makes it very easy to specify S- or P-polarization.

The use of oblique incidence generally requires PMLs (see above) and, thus, second-order elements. Internally, the tangential component of the electric field near the interface from which the wave emerges is produced by an artificial interface current, while the normal component in P-polarization stems from an artificial interface charge. Both these source quantities then have to be included on the right-hand sides of Eqs. (4.1).

Generation of a multigrid mesh hierarchy

If the MKFEM user desires, not only a single mesh, but a multigrid mesh hierarchy is generated. For this purpose, a single geometric mesh can be issued several times, with vector elements of increasing orders. Alternatively, a sequence of geometric meshes containing each other can be obtained by generating a first, coarsest mesh, followed by subdividing each tetrahedron into eight smaller tetrahedra (this subdivision is called mesh refinement), and maybe continuing recursively. In the latter case, all meshes are issued with elements of the same order. Also a combination is possible, the user just has to specify a list of numbers corresponding to the element orders of the multigrid levels, and mesh a refinement is only applied for each finer level which is assigned the same element order as the previous mesh case. Note that mesh refinements do not work in connection with curved geometry objects.

Choice of solvers

The MKFEM library offers two solvers, a direct[6] one and an iterative[7] one. These include the use of some parameters which have been chosen according to the experience and advice of Comsol AB as well as our own experience. The iterative solver needs a multigrid mesh hierarchy with at least two mesh cases, and solves for the finest one. Additional parameters (tolerance, error estimate) can optionally be issued to overwrite our default values. The direct solver does not need a mesh hierarchy, but can be used with such a mesh hierarchy to solve for a single specified mesh case.

Simplified postevaluation

After solving, the intensity ratio of transmittance, reflectance and absorbance of the Meta-material model can be calculated from the electric fields, by calling a MKFEM function.

Additionally, the nonlinear-optical quantities (source terms) as discussed in chapter 8 are computed from the linear-optical fields.

---

[6]SPOOLES solver [104]

[7]GMRES solver, with Geometric Multigrid preconditioner [104]

Achieving convergence

As mentioned in the previous section, two types of convergence have to be considered, and are ensured for the simulations of chapter 8. On one hand, the numerical convergence is provided by using the direct solver.

On the other hand, the convergence of numerics to physics is ensured by several procedures explained here. We always use curved geometries for metallic structures (e.g., see Fig. 4.1). This is not only in accordance with experiments [cf. Fig. 3.2(a)] but also serves to make the numbers of local fields, and especially nonlinear quantities, considerably more stable and thus achieves a much better convergence. However, we have to use the direct solver because no mesh refinements are possible, and we cannot use (respectively) higher-order elements for a mesh hierarchy because of persisting memory limitations. It is also clear that with curved geometries we cannot use mesh refinements to prove convergence (which would be the mathematically correct proof), but we have to use a sequence of increasingly finer meshes which do not contain each other. The nonlinear observables presented in chapter 8 are exclusively connected with the metal structure, and usually the convergence of these observables is investigated by varying the mesh discretization inside the metal (and on the metal surface) by a factor of 1.5–2.0. We speak of converged results because the corresponding numbers do not vary systematically (they do not increase or decrease monotonically) and vary by less than 1–5 % of their relative values when using the different meshes.

For our normal-incidence simulations, we use linear vector elements and no PMLs.[8] The evanescent fields prove to be well resolved, and they decay strongly before hitting the boundary of the calculation volume, as checked by visualizing the fields and by computing corresponding numbers.

For oblique incidence, PMLs and quadratical elements are used, and we always first check the mesh and PMLs with a simple scenario. All geometry objects, i.e., the substrate, air and gold geometry, are included for the mesh generation. However, the material parameters of the volume which later describes gold is temporarily set to the values of air, resulting in a simple flat air/substrate interface. The reflection of this interface is simulated and checked against the Fresnel formulas (2.14). Only after passing this check within less than 1 % relative or 0.1 % absolute error, the mesh and PMLs are used for simulations of the Metamaterial, including the gold parameters and further checks as described above.

In general, we always use a mesh discretization smaller than one tenth (one sixth) of relevant wavelengths for linear (quadratic) elements [104].

---

[8]except when computing the transmittance for small wavelengths and large SRRs (section 8.1), where we use "hand-made" PMLs with constant absorption and linear elements, for historical reasons

Chapter 5

The homogeneous linewidth and nonlinear-optical methods

Both Metallic Photonic Crystal Slabs and photonic Metamaterials can be considered, more generally, as arrays of Metal Nanoparticles (MNPs). In the field of MNPs (see, e.g., [90, 116–121]), an important challenge has been the experimental determination of the plasmon decay time τ. This chapter clarifies a historical misunderstanding and additionally explains why we do not, in the remaining chapters, address decay times or linewidths in any more detail.

The plasmon decay time is difficult to determine because linear- and nonlinear-optical methods usually average over several thousands of MNPs to obtain an acceptable signal strength. Depending on the fabrication method (e.g., lithographic patterning [90], Volmer-Weber growth [122]), a distribution of particle sizes, shapes, and hence plasmon resonance frequencies results (cf. section 2.3.1). Thus, linear-optical spectroscopy on particle ensembles only delivers the total linewidth, resulting from both the homogeneous linewidth $\gamma = 1/(2\tau)$ (of the plasmon) and the inhomogeneous linewidth (from differences in particles).

It was first believed in error that (nonlinear) time-resolved femtosecond measurements (similar to our experiments of chapter 7) could deliver the decay time directly [91], which subsequently has been revoked. Later, it was claimed [24] that a combination of linear- and nonlinear-optical methods could distinguish between homogeneous and inhomogeneous contributions: The authors of [24] presented calculations which seemingly show a dependence of the interferometric second-order autocorrelation signal (cf. section 3.3.1) on the plasmon decay time, while keeping the total linear-optical linewidth fixed. That work has been the basis of much if not most of the work that followed in this field [25–30, 123]. Here, we identify a technical mistake in the calculations of [24] and prove that the authors' idea is not correct when employing SHG or THG. Since we use SHG and THG for the investigations of the remaining chapters of this thesis, we will consequently not investigate linewidths in any more detail, and rather use damping constants as purely phenomenological quantities.

We begin by discussing analytic results for the limit of δ-pulses and Lorentzian inhomogeneous broadening (section 5.1), also stating which nonlinear methods indeed allow for the determination of the homogeneous linewidth. We continue with numerical simulations for pulses of finite duration and Gaussian inhomogeneous broadening (section 5.2).

5.1 Analytic calculations

Following along the lines of [24] and repeating our equivalent ansatz of section 2.3.1, we start by describing a particle plasmon by an oscillating particle with abstract charge q, mass m, and displacement $x(t)$, driven by an electric field $E(t)$ via

$$\ddot{x} + 2\gamma\dot{x} + \Omega_0^2 x + (\xi x^2 + \eta x^3 + ...) = \frac{q}{m}E(t) . \tag{5.1}$$

For the interferometric experiments to be described, $E(t)$ corresponds to a pair of copropagating pulses with time delay T. In linear optics, i.e., for $\xi = \eta = ... = 0$, this leads to a Lorentz oscillator resonance at the damped eigenfrequency $\Omega = \sqrt{\Omega_0^2 - \gamma^2}$ with a half-width-at-half-maximum (HWHM) homogeneous linewidth $\gamma = 1/(2\tau)$.

To first order in the laser electric field, the polarization $P^{(1)} \propto x^{(1)}(t)$ is given by

$$x^{(1)}(t) \propto \Omega^{-1} \int\limits_{-\infty}^{t} \mathrm{d}t' \, \mathrm{e}^{-\gamma(t-t')} \, \sin\left[\Omega\left(t - t'\right)\right] E(t') . \tag{5.2}$$

Upon excitation with resonant pulses, $P^{(1)}(t)$ oscillates with frequencies around Ω. To second order in the laser electric field, $-\xi\{x^{(1)}(t)\}^2$ is the driving term for the second-order displacement $x^{(2)}(t)$ (cp. section 2.2). Provided that this driving term is off-resonant with respect to Ω, we obtain the second-order polarization $P^{(2)}(t) \propto x^{(2)}(t)$ with

$$x^{(2)}(t) \propto \left[x^{(1)}(t)\right]^2 . \tag{5.3}$$

As explained in section 2.2.1, this expression contains a second-harmonic (SHG) contribution with frequencies around 2Ω and additionally a contribution of optical rectification (OR) around zero frequency, which plays a crucial role in this chapter. Furthermore, the authors of [24] argued (see also formulas in [27, 91]) that the signal S measured by a slow detector is given by the integral of the nonlinear intensity over time, i.e.,

$$S_{\mathrm{SHG+OR}}^{(2)}(T) \propto \int_{-\infty}^{\infty} \mathrm{d}t \left[P^{(2)}(t)\right]^2 . \tag{5.4}$$

It is crucial to note that this expression comprises both SHG and OR. *This, however, is in contrast to what is actually measured* in a second-order interferometric autocorrelation (IAC) setup, where one exclusively detects the emitted SHG by means of a photomultiplier tube behind carefully selected *optical filters* which suppress all contributions other than SHG.[1]

For reasons of simplicity and to allow for analytic results, we first discuss excitation with a pair of δ-pulses, i.e.,

$$E(t) = \hat{E}_0 \left[\delta(t) + \delta(t - T)\right] . \tag{5.5}$$

---

[1]The same problem associated with Eq. (5.4) can arise for a conventional interferometric autocorrelation of laser pulses (compare [124]), where one has $P^{(2)}(t) \propto \chi^{(2)} E^2(t)$. There, however, the IAC remains unaffected, provided that the negative-frequency part of the laser spectrum has negligible overlap with the positive-frequency part.

It is clear for symmetry reasons that the nonlinear signals only depend on $|T|$. Thus, we only consider $T \geq 0$ in what follows. For a single homogeneously broadened oscillator we obtain

$$
\begin{aligned}
P^{(1)}(t) \quad \propto \quad & \Omega^{-1}\Big(\Theta(t)\,\mathrm{e}^{-\gamma t}\sin\left(\Omega t\right) \\
& +\Theta(t-T)\,\mathrm{e}^{-\gamma(t-T)}\sin\left[\Omega(t-T)\right]\Big).
\end{aligned}
\tag{5.6}
$$

This leads to the second-order polarization

$$
\begin{aligned}
P^{(2)}(t) \quad \propto \quad & \Omega^{-2}\Big(\Theta(t)\,\mathrm{e}^{-2\gamma t}[1-\cos\left(2\Omega t\right)] \\
& +\Theta(t-T)\,\mathrm{e}^{-2\gamma(t-T)}\{1-\cos\left[2\Omega(t-T)\right]\} \\
& +2\Theta(t-T)\,\mathrm{e}^{-\gamma(2t-T)}\{\cos\left(\Omega T\right)-\cos\left[\Omega(2t-T)\right]\}\Big).
\end{aligned}
\tag{5.7}
$$

Let us now consider an inhomogeneously broadened ensemble of oscillators with fixed damping γ and a Lorentzian distribution of eigenfrequencies Ω with the distribution function

$$
w(\Omega) = \frac{\Gamma/\pi}{(\Omega-\overline{\Omega})^2 + \Gamma^2}\,,
\tag{5.8}
$$

which is centered around frequency $\overline{\Omega}$. The HWHM of this inhomogeneous distribution is Γ. To work out the convolution, we approximate the prefactor $1/\Omega^2$ in Eq. (5.7) by $1/\overline{\Omega}^2$. This approximation is justified in the limit $\Gamma \ll \overline{\Omega}$, which is usually well satisfied for lithographically fabricated particles. These two steps together lead to

$$
\begin{aligned}
P^{(2)}_{\mathrm{inhom}}(t) \quad \propto \quad & \int_{-\infty}^{\infty}\mathrm{d}\Omega\, w(\Omega)P^{(2)}(t) \\
\propto \quad & +\Theta(t)\,\mathrm{e}^{-2\gamma t} \\
& +\Theta(t-T)\,\mathrm{e}^{-2\gamma(t-T)} \\
& +2\Theta(t-T)\,\mathrm{e}^{-\gamma(2t-T)-\Gamma T}\cos\left(\overline{\Omega}T\right) \\[4pt]
& -\Theta(t)\,\mathrm{e}^{-2(\gamma+\Gamma)t}\cos\left(2\overline{\Omega}t\right) \\
& -\Theta(t-T)\,\mathrm{e}^{-2(\gamma+\Gamma)(t-T)}\cos\left[2\overline{\Omega}(t-T)\right] \\
& -2\Theta(t-T)\,\mathrm{e}^{-(\gamma+\Gamma)(2t-T)}\cos\left[\overline{\Omega}(2t-T)\right].
\end{aligned}
\tag{5.9}
$$

The first three summands correspond to OR, the last three summands to SHG. Note that the latter solely depends on the total width $\gamma + \Gamma$. In linear optics, the linewidth of the inhomogeneous ensemble results from the convolution of a Lorentzian with homogeneous width γ with a Lorentzian of inhomogeneous width Γ. This leads to a total resonance linewidth of $\gamma + \Gamma$ in linear optics. Thus, both the linear response and the correctly calculated SHG depend in the very same manner on the homogeneous and inhomogeneous linewidths, and a distinction is strictly not possible.

In contrast, the contribution from OR does not simply depend on $\gamma + \Gamma$, potentially allowing for a distinction between homogeneous and inhomogeneous linewidths. It is clear

that by erroneously including OR in the calculated interferometric "SHG signal" [24], a separation of the homogeneous and inhomogeneous contributions to the linewidth erroneously seems possible.

We have performed an analogous calculation for the third-order nonlinear-optical response. For third-harmonic generation and $T \geq 0$, we find that the ensemble THG polarization with a frequency around $3\overline{\Omega}$ is

$$
\begin{aligned}
P^{(3)}_{\text{THG, inhom}}(t) \quad \propto \quad & -\Theta(t)\,e^{-3(\gamma+\Gamma)t}\cos\left(3\overline{\Omega}t\right) \\
& -\Theta(t-T)\,e^{-3(\gamma+\Gamma)(t-T)}\cos\left[3\overline{\Omega}(t-T)\right] \\
& -3\Theta(t-T)\,e^{-(\gamma+\Gamma)(3t-T)}\cos\left[\overline{\Omega}(3t-T)\right] \\
& -3\Theta(t-T)\,e^{-(\gamma+\Gamma)(3t-2T)}\cos\left[\overline{\Omega}(3t-2T)\right].
\end{aligned}
\tag{5.10}
$$

The THG again only depends on $\gamma + \Gamma$, and no information on the homogeneous linewidth γ can be obtained. However, self-phase modulation (SPM) with a frequency around $\overline{\Omega}$ (see section 2.2.1) would provide such information. In a non-copropagating geometry, the latter would give rise to a diffracted four-wave-mixing (FWM) signal. Corresponding calculations have been presented in [125].

Broadly speaking, nonlinear-optical signals of the type $\omega + \omega$ (SHG) or $\omega + \omega + \omega$ (THG), etc. do not allow one to distinguish between homogeneous and inhomogeneous contributions to the linewidth, whereas signals of the type $\omega - \omega$ (OR) or $\omega + \omega - \omega$ (SPM or FWM), etc. do allow for such distinction. The "$-$" sign in OR, SPM, FWM, etc., effectively reverses the time axis in analogy to phase conjugation. For example in FWM, the "$-$" sign leads to the well-known photon-echo response [125]. At this point, a decay of the ensemble polarization due to inhomogeneous broadening (just interference) is reversed, whereas damping due to homogeneous broadening (a dissipative process) cannot be reversed.

5.2 Numerical calculations

The presented analytical calculations for δ-pulses are appropriate if the (complex) laser electric field spectrum exhibits negligible variation on the scale of the homogeneous linewidth γ. For longer pulses, we perform numerical simulations.[2] As described above, the correct way to calculate the SHG contribution is to spectrally filter the second-order response of the oscillator ensemble. To obtain the final IAC signal as a function of the time delay T, the square modulus of this filtered second-order polarization has to be integrated with respect to frequency. To allow for a direct comparison with the results of [24], we also use sech[2]-shaped $15\,\text{fs}$ pulses with a center wavelength of $780\,\text{nm}$, resonantly exciting the ensemble. The latter has a Gaussian distribution of resonances and is discretized in steps of $1\,\text{nm}$.

Figure 5.1 shows the resulting full-width-at-half-maximum (FWHM) of the interferometric autocorrelation as a function of the plasmon decay time τ. The full symbols correspond to the correct calculation, whereas the open symbols erroneously comprise the OR

---

[2]These simulations are performed within the MATLAB environment [126] which facilitates discrete Fourier transforms, spectral filtering, convolutions, and interpolation of data vectors.
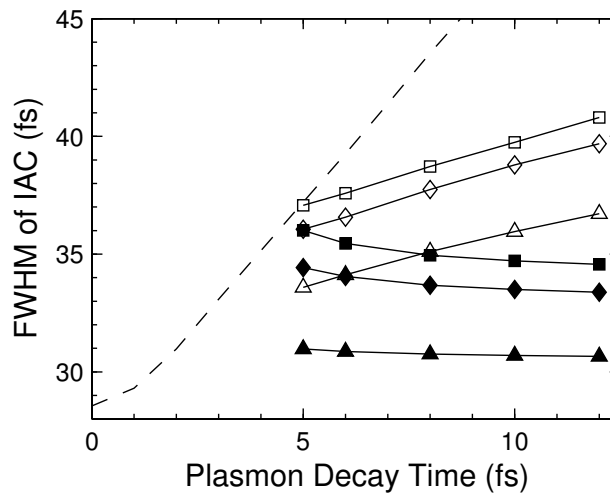
Figure 5.1: Recalculated data of Fig. 2 of [24]. The dashed line describes the simulated FWHM of the second-order interferometric autocorrelation (IAC) from one single resonant Lorentz oscillator (the particle plasmon), versus plasmon decay time τ. The solid lines represent ensembles of many oscillators with eigenfrequencies following a Gaussian distribution, for which the width is determined by fixing the total extinction linewidth $\Delta\lambda$ (squares: $\Delta\lambda$=70 nm; diamonds: $\Delta\lambda$=80 nm; triangles: $\Delta\lambda$=125 nm). The autocorrelation width is indicated by the full symbols for considering exclusively the correct contribution of SHG. Corresponding results for erroneously including both SHG and OR on trial are shown by the open symbols.

contribution and qualitatively reproduce the results of [24] (see their Fig. 2). For each of the curves in our Fig. 5.1, the total linewidth of the linear-optical spectrum is fixed. The squares, diamonds, and triangles correspond to a fixed extinction linewidth (FWHM) of $\Delta\lambda$=70, 80, and 125 nm, respectively (see parameters of Fig. 2 of [24]). The dashed curve corresponds to a single (homogeneously broadened) oscillator for reference. The correct results and those including the OR contribution differ strongly – as in our analytical calculations. In particular, the slopes of the correct curves in our Fig. 5.1 are very nearly zero (within typical experimental error bars of 1 fs), while the incorrect simulations have a small positive slope. Thus, using the correct curves one cannot infer the plasmon decay time from measured interferometric autocorrelations, whereas the incorrect curves erroneously suggest this possibility [24]. We conclude that, under inhomogeneous conditions, the homogeneous linewidth cannot be determined by analyzing linewidths from linear optics and SHG (or THG) measurements. In consequence, we refrain from making any quantitative statements about plasmon decay times in any other part of this thesis.

We note in passing that the IAC acquires artificial "wings" [24] if the OR contribution is erroneously included. Indeed, such wings are visible in Fig. 1a of [24]. They disappear in the correct calculation (not shown).

Chapter 6

Nonlinear optics of Metallic Photonic Crystal Slabs: Theory

In section 2.4, we have introduced Metallic Photonic Crystal Slabs (MPCSs) and explained their key feature, the coupling of a photonic resonance (the waveguide mode resonance) with an electronic resonance (the particle plasmon resonance). In this chapter, we develop a simple model describing MPCSs as two coupled Lorentz oscillators, and derive their optical properties.

We discuss their linear optics in section 6.1. In contrast to frequent belief, two coupled classical Lorentzian oscillators which include damping lead to an optical response which does not correspond to that of two new effective Lorentzian oscillators. Instead, our model generally leads to Fano-like lineshapes in the linear-optical absorption spectra. This aspect is consistent with experiments on MPCSs [30, 58–61]. In section 6.2 we extend our model to the nonlinear optics of two coupled oscillators. We show that signatures of interferometric third-harmonic generation depend on the source of nonlinearity. The parameters of the presented numerical calculations are chosen to allow for a direct comparison with our experimental results, which are presented in chapter 7.

Our theoretical approach is thus distinct from earlier descriptions of the linear- and nonlinear-optical properties of MPCSs. Those descriptions include either a semi-quantum mechanical approach [59], or two independent Lorentz oscillators with ad-hoc decay times [30] (also confer chapter 5). In comparison, our simple model gives a clearer picture of the fundamental physical relations while explaining more findings of experiments, e.g., the lineshapes appearing in linear as well as nonlinear optics.

6.1 Linear optics of two coupled Lorentz oscillators

In section 2.3.1 we have introduced an abstract harmonic oscillator as a system to describe a particle plasmon oscillation. Now, we additionally apply the same idea to the oscillating electric field of the waveguide mode. Then, the generalization of Eq. (2.35) to a system of

two coupled, oscillating particles of equal mass m leads to the equations of motion

$$\ddot{x}_{\mathrm{pl}} + 2\gamma_{\mathrm{pl}}\dot{x}_{\mathrm{pl}} + \Omega_{\mathrm{pl}}^2 x_{\mathrm{pl}} + (\mathrm{NL})_{\mathrm{pl}} - \Omega_{\mathrm{c}}^2 x_{\mathrm{wg}} = \frac{q_{\mathrm{pl}}}{m} E(t), \tag{6.1a}$$

$$\ddot{x}_{\mathrm{wg}} + 2\gamma_{\mathrm{wg}}\dot{x}_{\mathrm{wg}} + \Omega_{\mathrm{wg}}^2 x_{\mathrm{wg}} + (\mathrm{NL})_{\mathrm{wg}} - \Omega_{\mathrm{c}}^2 x_{\mathrm{pl}} = \frac{q_{\mathrm{wg}}}{m} E(t). \tag{6.1b}$$

Here, $x_{\mathrm{pl}}(t)$ and $x_{\mathrm{wg}}(t)$ are the displacements representing the plasmon and waveguide oscillations, respectively. The resonance frequencies, the HWHMs, and the oscillator strengths of the uncoupled system are denoted by Ω_j, γ_j, and q_j ($j = \mathrm{pl}, \mathrm{wg}$), respectively. Ω_{c}^2 represents the coupling strength between the oscillators. The nonlinear terms (denoted by NL) are discussed in section 6.2 and ignored here.

In order to make the resulting formulas transparent, we immediately discuss a few parameters in terms of their experimentally relevant values. Since the uncoupled waveguide resonance is extremely sharp [127] as compared to the plasmon width, we set the waveguide damping $\gamma_{\mathrm{wg}} = 0$. In the following, we derive formulae for an arbitrary waveguide oscillator strength q_{wg}, however, most aspects can already be understood in the simpler case $q_{\mathrm{wg}} = 0$. For typical sample parameters, $|q_{\mathrm{wg}}| \ll |q_{\mathrm{pl}}|$ holds, i.e., the area under the extinction curve of the (uncoupled) waveguide mode is much smaller than that of the plasmon.

The differential equations (6.1) can easily be solved analytically in the frequency domain (cf. section 2.1.2), that is, after replacing each variable in Eqs. (6.1) by its transformed variable ($x_{\mathrm{pl}} \to \tilde{x}_{\mathrm{pl}}$ etc.) and replacing each time derivative by the factor $(-\mathrm{i}\omega)$. Excitation with the electric field $\tilde{E}(\omega)$ then leads to the first-order displacements $\tilde{x}_j^{(1)}(\omega)$ and the polarizations $\tilde{P}_j^{(1)}(\omega) = N\,q_j\,\tilde{x}_j^{(1)}(\omega)$. N is the density of the oscillators. Note that in the case $q_{\mathrm{wg}} = 0$, only the plasmon oscillation $\tilde{x}_{\mathrm{pl}}^{(1)}(\omega)$ contributes to the polarization. In general, the total linear polarization $\tilde{P}^{(1)}(\omega) = \tilde{P}_{\mathrm{pl}}^{(1)}(\omega) + \tilde{P}_{\mathrm{wg}}^{(1)}(\omega)$ becomes

$$\tilde{P}^{(1)}(\omega) = \frac{N}{m} \frac{q_{\mathrm{pl}}^2\left(-\omega^2 + \Omega_{\mathrm{wg}}^2\right) + 2q_{\mathrm{pl}}q_{\mathrm{wg}}\Omega_{\mathrm{c}}^2 + q_{\mathrm{wg}}^2\left(-\omega^2 - 2\mathrm{i}\omega\gamma_{\mathrm{pl}} + \Omega_{\mathrm{pl}}^2\right)}{\left(-\omega^2 - 2\mathrm{i}\omega\gamma_{\mathrm{pl}} + \Omega_{\mathrm{pl}}^2\right)\left(-\omega^2 + \Omega_{\mathrm{wg}}^2\right) - \Omega_{\mathrm{c}}^4} \tilde{E}(\omega). \tag{6.2}$$

The linear susceptibility $\chi^{(1)}(\omega) = \tilde{P}^{(1)}(\omega)/[\varepsilon_0\tilde{E}(\omega)]$ and the absorption coefficient

$$\begin{aligned}
\alpha(\omega) &= \frac{\omega}{c_0} \mathrm{Im}\left[\chi^{(1)}(\omega)\right] \\
&= \alpha_{\mathrm{pl}} \frac{4\gamma_{\mathrm{pl}}^2\omega^2\left[\omega^2 - \Omega_{\mathrm{wg}}^2 - (q_{\mathrm{wg}}/q_{\mathrm{pl}})\,\Omega_{\mathrm{c}}^2\right]^2}{\left[\left(\omega^2 - \Omega_{\mathrm{pl}}^2\right)\left(\omega^2 - \Omega_{\mathrm{wg}}^2\right) - \Omega_{\mathrm{c}}^4\right]^2 + 4\gamma_{\mathrm{pl}}^2\omega^2\left(\omega^2 - \Omega_{\mathrm{wg}}^2\right)^2}
\end{aligned} \tag{6.3}$$

are independent of the excitation and immediately follow. $\alpha_{\mathrm{pl}} = Nq_{\mathrm{pl}}^2/(2m\varepsilon_0 c_0\gamma_{\mathrm{pl}})$ is the maximum absorption coefficient of the uncoupled plasmon oscillation.

Examples of absorption spectra are shown in Fig. 6.1(a) for $q_{\mathrm{wg}}/q_{\mathrm{pl}}=0$ and in Fig. 6.1(b) for $q_{\mathrm{wg}}/q_{\mathrm{pl}}=+0.1$. In both cases, one obtains the anticipated anti-crossing behavior. For $q_{\mathrm{wg}}=0$, absorption maxima appear at the spectral positions

$$\Omega_{a,b}^2 = \left(\Omega_{\mathrm{pl}}^2 + \Omega_{\mathrm{wg}}^2\right)/2 \pm \left[\left(\Omega_{\mathrm{pl}}^2 - \Omega_{\mathrm{wg}}^2\right)^2/4 + \Omega_{\mathrm{c}}^4\right]^{1/2}. \tag{6.4}$$
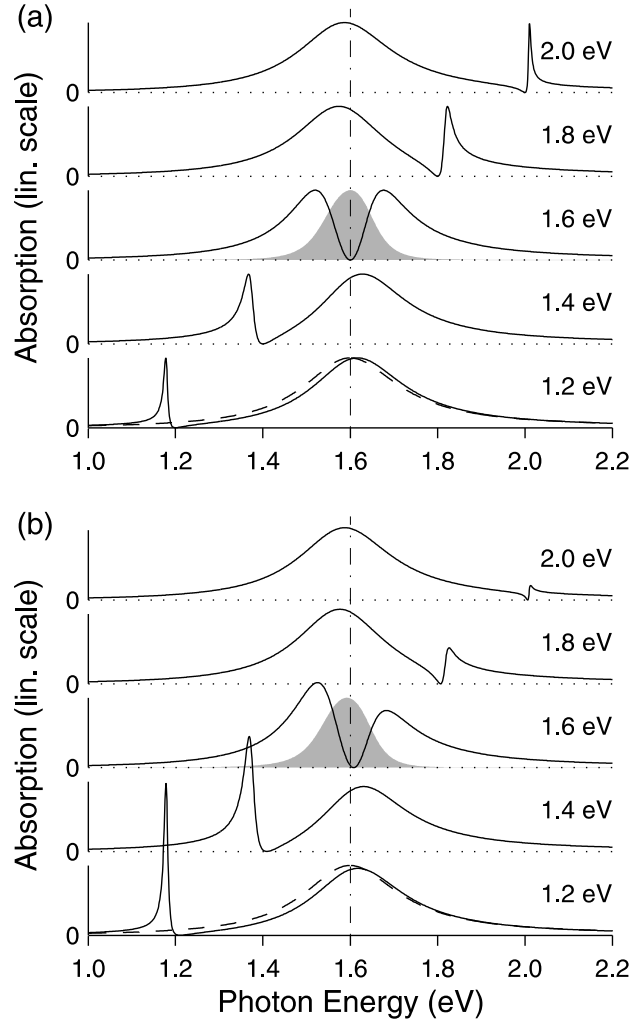
Figure 6.1: Optical absorption spectra according to Eq. (6.3) (solid lines). One observes an anti-crossing behavior when varying the waveguide resonance frequency, Ω_{wg}, with respect to the fixed plasmon resonance frequency, Ω_{pl}. Note the highly asymmetric, Fano-like lineshape of the peaks. All curves are displayed on the same scale. $q_{\text{wg}}/q_{\text{pl}}$ equals 0 in (a) and $+0.1$ in (b). Common parameters are $\hbar\Omega_{\text{pl}}=1.6\,\text{eV}$, $\hbar\Omega_{\text{wg}}$ as denoted for each curve, $\gamma_{\text{pl}}=1/(2\tau)$, $\tau=2.5\,\text{fs}$, and $\hbar\Omega_{\text{c}}=0.5\,\text{eV}$. The dashed lines represent the pure plasmonic absorption in the absence of coupling, i.e., for $\hbar\Omega_{\text{c}}=0$. Assuming $|\tilde{E}(\omega)| = \text{const}$, the gray areas shown for $\hbar\Omega_{\text{wg}}=1.6\,\text{eV}$ depict the square modulus of the waveguide amplitude spectrum, $|\tilde{x}_{\text{wg}}^{(1)}|^2$, each exhibiting a single peak. In (a), the square modulus of the plasmon amplitude spectrum, $|\tilde{x}_{\text{pl}}^{(1)}|^2$, is roughly proportional to the corresponding absorption spectrum. The vertical line is a guide to the eye.

These positions coincide with the normal mode frequencies of the coupled, but undamped system. For small Ω_{c} and for $\Omega_{\text{pl}}=\Omega_{\text{wg}}$, the corresponding Rabi splitting is given by $\Omega_{\text{c}}^2/\Omega_{\text{pl}}$. Hence, the two oscillators can be considered as "resonant" if $|\Omega_{\text{pl}} - \Omega_{\text{wg}}| \ll \Omega_{\text{c}}^2/\Omega_{\text{av}}$ with $\Omega_{\text{av}}=(\Omega_{\text{pl}} + \Omega_{\text{wg}})/2$, and as "nonresonant" otherwise.

In contrast to frequent belief, the lineshapes in Fig. 6.1 do not correspond to the sum of two effective Lorentz oscillators. One rather gets a highly asymmetric, Fano-like lineshape. Usually, a Fano resonance results from the coherent interaction of a discrete quantum me-

chanical state with a continuum of states [128, 129]. In our purely classical model, a single sharp oscillator coherently interacts with a strongly broadened second oscillator. The latter replaces the continuum. One result of the Fano-like interaction is that one obtains zero absorption between the two absorption maxima. The position of this zero appears at the root of the numerator of (6.3), i.e., at or near the spectral position of the (uncoupled) waveguide mode Ω_{wg}. Intuitively, this minimum is a result of destructive interference, which effectively suppresses the response of the two absorption "channels," of which the polarizations have a phase difference near π. This phase difference will also be important in nonlinear optics (see section 6.2). When q_{wg} is changed from zero to a nonzero value, the positions of the absorption extrema shift slightly, and the two peaks exhibit different heights as an additional characteristic. For example, a reduced absorption of the more waveguide-like channel results, in the case $q_{\mathrm{wg}}/q_{\mathrm{pl}} > 0$ and $\Omega_{\mathrm{pl}} < \Omega_{\mathrm{wg}}$ [see top curves in Fig. 6.1(b)]. Note that the lineshapes in Fig. 6.1 describe very well the key experimental features of the linear optics of MPCSs (see section 7.2 and [30, 58–61]).

We mention briefly that, for instance for $q_{\mathrm{wg}}{=}0$, the total absorption (6.3) can be rewritten as a sum of two "Lorentzians," but with strongly frequency-dependent dampings. In the time domain, these frequency-dependent dampings correspond to a non-Markovian (and non-exponential) decay. For $\Omega_a < \Omega_{\mathrm{wg}} < \Omega_b$, one solution can be described by the oscillator a having a constant resonance frequency Ω_a and a frequency-dependent damping

$$\gamma_a(\omega) = \begin{cases} \frac{\gamma_{\mathrm{pl}}\alpha_{\mathrm{pl}}}{2\alpha(\omega)}\left(1 + \left[1 - \frac{\alpha^2(\omega)\left(\omega^2 - \Omega_a^2\right)^2}{\alpha_{\mathrm{pl}}^2\gamma_{\mathrm{pl}}^2\omega^2}\right]^{1/2}\right), & \omega < \Omega_{\mathrm{wg}} \\ \infty & , & \omega \geq \Omega_{\mathrm{wg}} \end{cases} \tag{6.5}$$

and an analogous expression for the oscillator b.

6.2 Nonlinear optics of two coupled Lorentz oscillators

We now discuss the nonlinear-optical properties of two coupled Lorentz oscillators in terms of third-harmonic generation, starting in the time domain. Our analysis allows for a direct comparison with our interferometric experiments presented in section 7.3. We consider an inversion-symmetric medium, hence all second-order nonlinear terms in Eqs. (6.1) are zero. At first sight, one might only expect third-order nonlinear terms like $(\mathrm{NL})_{\mathrm{pl}} \propto x_{\mathrm{pl}}^3$ or $(\mathrm{NL})_{\mathrm{wg}} \propto x_{\mathrm{wg}}^3$ in Eqs. (6.1). However, mathematically, the most general form is given by the terms

$$\eta_{j,k}\left(x_{\mathrm{pl}}(t)\right)^{3-k}\left(x_{\mathrm{wg}}(t)\right)^k \tag{6.6}$$

appearing in the differential equation for $x_j(t)$, respectively ($j = \mathrm{pl}, \mathrm{wg}; k = 0, 1, 2, 3$). Here, we are only interested in THG, which is off-resonant. In a perturbational approach (cp. section 2.2), the THG contributions to the third-order displacements are given by

$$x_j^{(3)}(t) \propto \sum_{k=0}^{3} \eta_{j,k}\left(x_{\mathrm{pl}}^{(1)}(t)\right)^{3-k}\left(x_{\mathrm{wg}}^{(1)}(t)\right)^k. \tag{6.7}$$

The eight parameters $\eta_{j,k}$ can be reduced to four nonlinearity parameters $\eta_k = \sum_j q_j \eta_{j,k}$ with $k = 0, 1, 2, 3$, because the optical polarization is given by the weighted sum of the displacements. This leads to the following general form for the THG contribution to the third-order polarization:

$$P^{(3)}(t) \propto \sum_{k=0}^{3} \eta_k \left(x_{\mathrm{pl}}^{(1)}(t) \right)^{3-k} \left(x_{\mathrm{wg}}^{(1)}(t) \right)^k . \tag{6.8}$$

We note in passing that this form is generally different from the ansatz $P^{(3)}(t) \propto [P^{(1)}(t)]^3$ (in analogy to [30]), which leads to $\eta_k \propto \binom{3}{k} q_{\mathrm{pl}}^{3-k} q_{\mathrm{wg}}^k$.

For the numerical computation of THG spectra, we choose the electric field $E(t)$ depicted in Fig. 3.5(d) in order to resemble the 5-fs laser pulses of the experiments. (Alternatively, 5-fs Gaussian pulses deliver qualitatively similar results for all conditions discussed here.) Furthermore, we fix $\Omega_{\mathrm{pl}}{=}1.67\,\mathrm{eV}$, $\Omega_{\mathrm{wg}}{=}1.56\,\mathrm{eV}$, $\Omega_{\mathrm{c}}{=}0.66\,\mathrm{eV}$, $\tau{=}1.06\,\mathrm{fs}$, and $q_{\mathrm{wg}}/q_{\mathrm{pl}}{=}{+}0.085$. These parameters correspond to the sample MPCS-*A* in chapter 7, which can be considered as "resonant" according to the definition given in the previous section. The integration[1] of the equations of motion (6.1) yields the first-order displacements $x_j^{(1)}(t)$ and, with (6.8), the third-order polarization. The square modulus of its filtered Fourier transform delivers the THG intensity spectrum. Spectra are calculated as functions of the spectrometer photon energy and of the interferometric time delay T between the two excitation pulses.

We first discuss the case $\eta_k \propto \delta_{k,0}$ ($\delta_{k,l}$ is the Kronecker symbol) in which the nonlinearity is exclusively connected with the plasmon oscillation. The corresponding data set is shown in Fig. 6.2(a). A cut at $T{=}0$ (not shown) reveals four broad but clearly distinct spectral peaks in the THG spectrum. The appearance of four peaks can easily be understood in the frequency domain (cp. example in section 2.2.1), since the third-order polarization for this case is proportional to the twofold convolution of the displacement $\tilde{x}_{\mathrm{pl}}^{(1)}(\omega)$ with itself, this displacement containing two peaks [cp. Fig. 6.1(a)]. The relative weights of the four peaks can be estimated by employing the time domain. Assuming δ-pulses, $q_{\mathrm{wg}}{=}0$, and neglecting damping, the two effective oscillators (see previous section) have comparable amplitudes, and the general form of the THG polarization is proportional to

$$\left(\cos(\Omega_a t) + \cos(\Omega_b t) \right)^3 \quad \propto \quad \dots$$
$$+1 \cos(3\Omega_a t)$$
$$+3 \cos[(2\Omega_a + \Omega_b)t]$$
$$+3 \cos[(\Omega_a + 2\Omega_b)t]$$
$$+1 \cos(3\Omega_b t) . \tag{6.9}$$

The THG polarization contains terms at three times the normal mode frequencies Ω_a and Ω_b as well as spectral mixing products. The relative amplitudes 1:3:3:1 of the frequency components $3\Omega_a$, $2\Omega_a + \Omega_b$, $\Omega_a + 2\Omega_b$, and $3\Omega_b$ lead to the intensity ratios 1:9:9:1. This

---

[1]The Runge-Kutta integrator of MATLAB [126] needs to be able to evaluate the electric-field pulse $E(t)$ at arbitrary points of time t, which explains why we use an analytical formula, Eq. (3.3), to describe a single pulse. Furthermore, MATLAB facilitates discrete Fourier transforms and spectral filtering of data vectors.
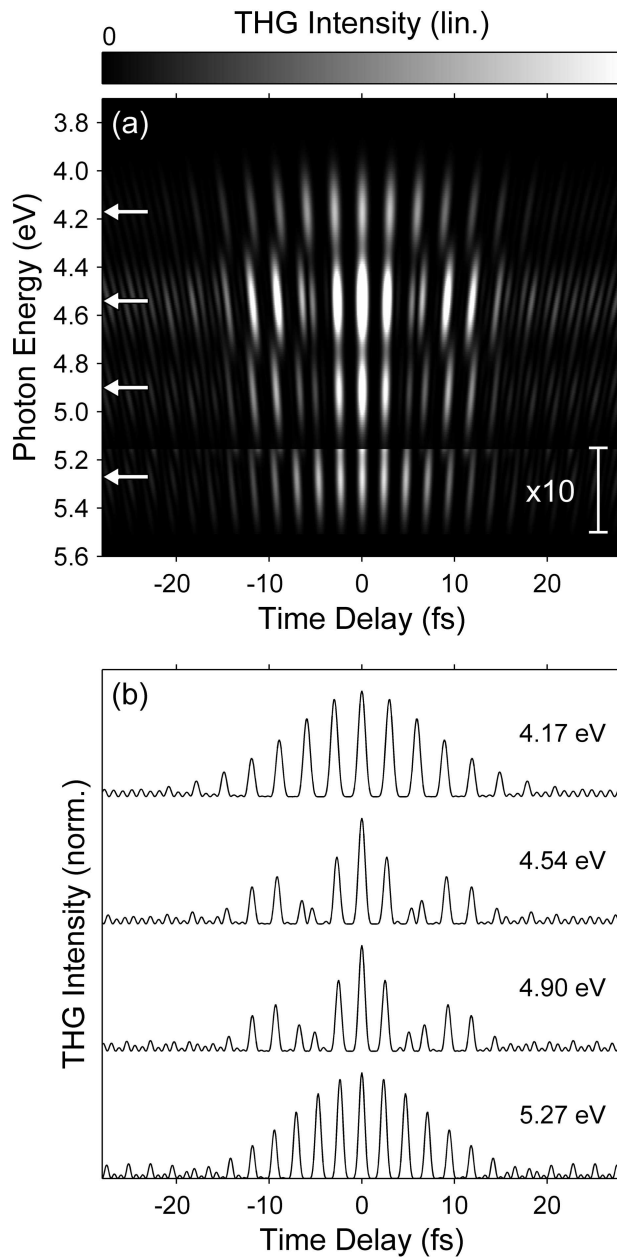
Figure 6.2: (a) Optical THG intensity derived from the coupled nonlinear oscillators. The THG intensity is shown on a saturated gray scale, versus spectrometer photon energy and time delay T between the two excitation pulses. At $T=0$, the THG spectrum exhibits four distinct peaks (the high-energy peak is amplified by a factor of 10 for the sake of clarity). The four peaks exhibit different temporal behaviors. Corresponding cuts at the spectral peak positions indicated by the white arrows in (a) are shown in (b). For better comparison, the curves are normalized to the same maximum and are vertically displaced. Obviously, the first and fourth curves both have a smoothly decaying (upper) envelope, while only the second and third curves show an envelope resulting from a beating. The nonlinearity parameters used are $\eta_k \propto \delta_{k,0}$. The other parameters are quoted in the text. Compare with the corresponding experiment (Fig. 7.3).

means that the two central frequency components are more prominent, in agreement with the numerical findings in Fig. 6.2(a).

The pronounced dips between the four spectral peaks are closely related to the Fano-like lineshapes discussed in section 6.1. In linear optics, the phase relation between the two effective oscillators (absorption "channels") leads to destructive interference, and hence to zero absorption in the dip. The same destructive interference is also responsible for the deep dips in the THG spectra.

The behavior of the THG intensity as a function of time delay T differs among the four spectral peaks. Corresponding cuts at the spectral peak positions indicated by the white arrows in Fig. 6.2(a) are shown in Fig. 6.2(b). The curves exhibit the usual oscillations with the respective fundamental and harmonic frequencies, enclosed in the (upper) envelope of interest. The first and fourth curves clearly show a smoothly decaying envelope for increasing $|T|$. In contrast, the envelopes of the central two curves (which are associated with the spectral mixing products) reveal a beating. In spectrally integrated measurements [30], this distinction is not possible.

So far, we have only discussed the case $\eta_k \propto \delta_{k,0}$. Next, we calculate corresponding THG spectra for different nonlinearity parameters (see Fig. 6.3). In each part of this figure, all nonlinear parameters are zero except for a single one. The parts (a), (b), and (c) result from a nonzero value of η_1, η_2, and η_3, showing three peaks, two peaks, and one peak, respectively. In the frequency domain, this can again be understood by the corresponding convolutions. Remember that $\tilde{x}_{\mathrm{pl}}^{(1)}(\omega)$ contains two peaks for the values chosen here, whereas $\tilde{x}_{\mathrm{wg}}^{(1)}(\omega)$ only contains one peak (compare to gray areas in Fig. 6.1).

In general, all parameters η_k can have nonzero values simultaneously. When adding up the nonlinear contributions to the polarization, interference can result in a THG intensity with amplified or suppressed spectral peaks and dips, spectrally shifted peak positions, or even with new peaks or dips which are not present at all in Figs. 6.2(a) and 6.3. We will not go into a detailed analysis. We only note that for $\eta_0 \gg \eta_1 > \eta_2 = \eta_3 = 0$, the tendency is to suppress the high-energy peaks compared to the case $\eta_0 \neq 0$ and $\eta_1 = \eta_2 = \eta_3 = 0$.

The key feature of the calculations presented so far is that the THG spectra depend on the underlying source of the nonlinearity, i.e., they depend on which of the coefficients η_k is nonzero. In other words, observing four, three, two, or just one peak in experimental THG spectra allows one to learn something about the system by comparison with theory. This, however, is only possible for a certain regime of coupling between the two oscillators, which we shall refer to as the regime of "moderate coupling." Obviously, for very small coupling strengths (for small values of Ω_c), the four spectral peaks in the THG spectrum of the case $\eta_k = \delta_{k,0}$ (discussed above) merge into a single peak. In the other limit (for large values of Ω_c), also $\tilde{x}_{\mathrm{wg}}^{(1)}(\omega)$ exhibits several peaks (unlike the gray areas in Fig. 6.1), which can, for example, lead to several spectral peaks in the THG spectrum for the case $\eta_k = \delta_{k,3}$ as well. By numerical calculations for the "resonant" case (i.e., $\Omega_{\mathrm{pl}} = \Omega_{\mathrm{wg}} = \Omega_{\mathrm{av}}$), for $q_{\mathrm{wg}} = 0$, and assuming δ-pulses, we can specify the regime of "moderate coupling" by the condition $0.15 < \Omega_c^2/(2\gamma\Omega_{\mathrm{av}}) < 1.35$. Thus, since we want to learn something about the source of the optical nonlinearity from the comparison of experiment and theory, we have to tailor the coupling parameter of samples correspondingly.
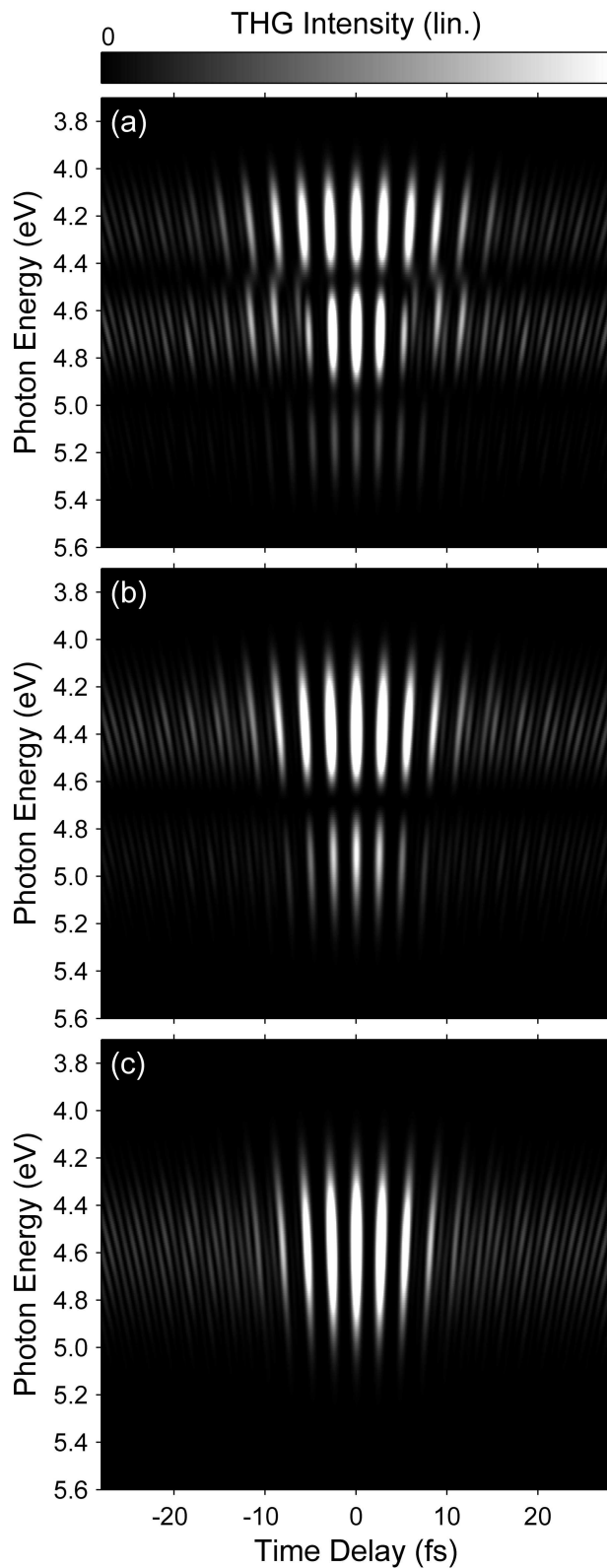
Figure 6.3: As Fig. 6.2(a), but for different nonlinearity parameters. The shown THG contributions result from a nonzero value of (a) η_1, (b) η_2, and (c) η_3 while keeping the respectively other nonlinearity parameters zero. At $T=0$, the number of spectral peaks is three, two, and one, respectively. (a), (b), and (c) are displayed on individual gray scales.

Chapter 7

Nonlinear optics of Metallic Photonic Crystal Slabs: Experiments

In this chapter, we present linear- and nonlinear-optical experiments on Metallic Photonic Crystal Slabs (MPCSs) and compare the findings with our theory (chapter 6). A MPCS constitutes a simple system to investigate the coupling of two resonances experimentally. Tailoring the waveguide parameters allows one to easily control the coupling strength, since the coupling arises from the spatial overlap of the plasmon and waveguide-mode fields.

The linear optics of MPCSs has first been discussed in [58] for 2D arrays of gold nanoparticles and in [59] for 1D arrays of gold nanowires. More recently, first nonlinear-optical experiments on MPCSs have been presented [30] which have been interpreted in terms of Lorentz oscillators with ad-hoc decay times. We disregard decay times and rather focus on lineshapes, which yield additional insights into the underlying physics. Moreover, our experiments on Third-Harmonic Generation go beyond previous work in two aspects. First, we use 5-fs optical pulses (instead of 13-fs pulses [30]) and thus achieve a better temporal resolution. Second, we do not only obtain indirect information on the temporal behavior by exciting the sample with a pair of time-delayed pulses (as usual in "time-resolved spectroscopy"), but we spectrally resolve the emitted nonlinear signals simultaneously (unlike [30]). Thus, we are able to observe in our experiments that the various spectral components of the third-harmonic signal exhibit substantially different temporal dynamics. Finally, the comparison of our experimental data with our simple theoretical model allows us to determine the dominant source of the underlying optical nonlinearity.

7.1 Description of samples

Metallic Photonic Crystal Slabs have been introduced in section 2.4. A more detailed scheme of our samples is shown in Fig. 7.1(a). The dielectric layers and the gold nanowire arrays are fabricated as described in section 3.1. Hafnium dioxide (HfO_2) is used as the high-index material forming the core of the slab waveguide between the quartz substrate and the magnesium fluoride (MgF_2) spacer layer. These dielectrics are best suited because of their transparency in the total spectral range of interest and exhibit minimal intrinsic THG (as we
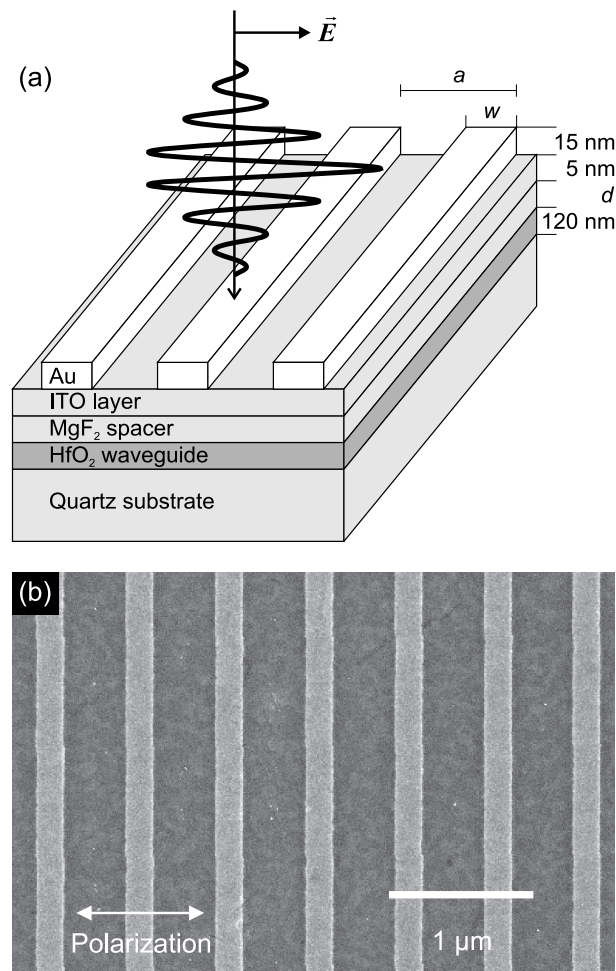
Figure 7.1: Experimental realization of a Metallic Photonic Crystal Slab. (a) Scheme showing gold nanowires on top of a set of dielectric layers forming the slab waveguide. HfO_2 is used as a high-index material, while MgF_2 serves as a low-index spacer. The polarization of the normally incident white light or laser pulses is perpendicular to the wires (TM-polarization) for the experiments shown in Figs. 7.2, 7.3, and 7.4. Samples with different lattice constant a, wire width w, and spacer thickness d are investigated. (b) Scanning electron micrograph of the gold nanowires (light gray) on top of the waveguide (dark gray).

investigated in independent experiments). The thin indium-tin oxide (ITO) layer is required during fabrication.

The particle plasmon resonance and the waveguide mode resonance are coupled due to the spatial overlap of their electric field distributions. The coupling strength (denoted by Ω_c^2 in the theory chapter 6) between the two resonances can conveniently be tailored by the spacer thickness d. It is clear that an increasing spacer thickness leads to decreasing coupling. We experimentally find that when choosing $d=30$ nm, the samples described below are within the regime of "moderate coupling" as defined in section 6.2 (for the values, see next section).

Each of the fabricated gold nanowire arrays covers a total area of $(60\,\mu m)^2$. The electron micrograph in Fig. 7.1(b) shows an enlarged view of a typical sample, revealing the high quality of the resulting structures. Typically, we fabricate entire sets of arrays on one glass
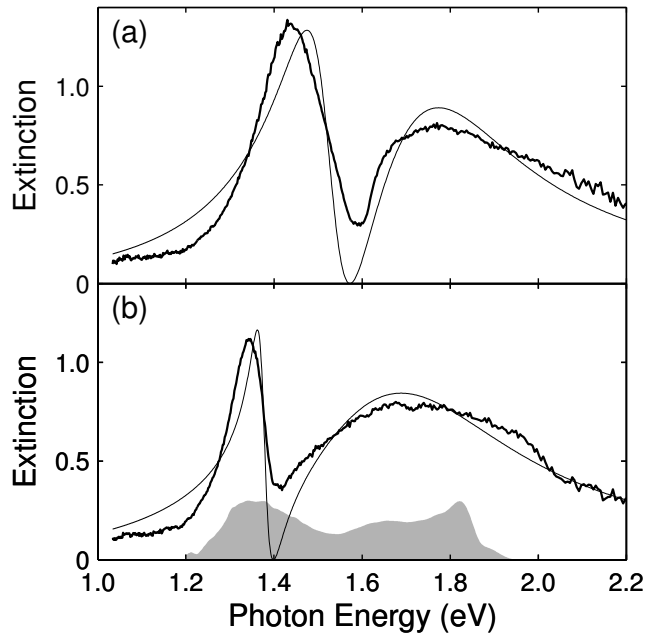
Figure 7.2: Extinction of the selected samples (a) MPCS-*A* and (b) MPCS-*B*. The thick curves show the extinction measured with a white-light source, referenced to the substrate without gold structures. The thin lines are absorption spectra based on the model of coupled Lorentz oscillators, Eq. (6.3), and obtained by a nonlinear least-squares fit to the corresponding experimental data. The gray area in (b) depicts again the electric field spectrum of the laser pulses used for the nonlinear-optical experiments [see Fig. 3.5(c)].

substrate. In such a set, e.g., the lattice constant a is varied from $500\,\text{nm}$ to $650\,\text{nm}$ in steps of $25\,\text{nm}$, and the nominal wire width from around $120\,\text{nm}$ to around $220\,\text{nm}$ in steps of $20\,\text{nm}$. In this fashion, we fabricate and investigate a total of 42 nanowire arrays on each substrate.

Out of this systematic study, we discuss a representative selection of two samples in the following, as examples for the "resonant" and "nonresonant" cases, respectively (see definition in section 6.1). The experimental parameters for sample MPCS-*A* are a=$550\,\text{nm}$ and w=$185\pm5\,\text{nm}$, and for sample MPCS-*B* a=$625\,\text{nm}$ and w=$195\pm5\,\text{nm}$, hence, the wire widths of the two samples are identical within experimental uncertainty, but their lattice constant differs.

7.2 Linear-optical properties

Using the second setup described in section 3.2.2, we measure the extinction spectra of sample MPCS-*A* and *B* (see thick curves in Fig. 7.2) for TM-polarization and for normal incidence. The extinction dip would be even more pronounced if we used a yet smaller numerical aperture [130].

To connect to the theory presented in chapter 6, we compare the measured extinction spectra with theoretical absorption spectra, Eq. (6.3). We find a good qualitative agreement of our simple model and the experiments. From a least-squares fit of the theory to the ex-

periment (see thin lines in Fig. 7.2) we obtain all relevant linear-optical parameters, leaving only the nonlinear coefficients η_k as free parameters for the nonlinear-optical experiments to come. The fit parameters of sample MPCS-*A* (MPCS-*B*) are $\hbar\Omega_{\mathrm{pl}}$=1.67 eV, $\hbar\Omega_{\mathrm{wg}}$=1.56 eV, $\hbar\Omega_{\mathrm{c}}$=0.66 eV, τ=1.06 fs, and $q_{\mathrm{wg}}/q_{\mathrm{pl}}$=+0.085 ($\hbar\Omega_{\mathrm{pl}}$=1.65 eV, $\hbar\Omega_{\mathrm{wg}}$=1.39 eV, $\hbar\Omega_{\mathrm{c}}$=0.54 eV, τ=0.97 fs, and $q_{\mathrm{wg}}/q_{\mathrm{pl}}$=+0.049), where τ=$1/(2\gamma_{\mathrm{pl}})$. The additional fit parameter α_{pl}, together with the coefficients η_k, determines the absolute strength of the THG signals.

Hence, sample MPCS-*A* is "resonant," i.e., $\hbar|\Omega_{\mathrm{pl}} - \Omega_{\mathrm{wg}}|$=0.11 eV < 0.27 eV=$\hbar\Omega_{\mathrm{c}}^2/\Omega_{\mathrm{av}}$, while sample MPCS-*B* is "nonresonant," i.e., $\hbar|\Omega_{\mathrm{pl}} - \Omega_{\mathrm{wg}}|$=0.26 eV > 0.19 eV=$\hbar\Omega_{\mathrm{c}}^2/\Omega_{\mathrm{av}}$, according to the definition of section 6.1. Additionally, both samples are within the regime of "moderate coupling" (see section 6.2), with a normalized coupling strength $\Omega_c^2/(2\gamma\Omega_{\mathrm{av}})$ of 0.43 for sample MPCS-*A* and 0.28 for sample MPCS-*B*.

7.3   Third-Harmonic Generation

In our THG experiments, we use the 5-fs pulses derived from the Ti:Sa laser setup described in section 3.3.1. The interferometer delivers two identical, copropagating, time-delayed copies of the linearly polarized pulses. These are focused onto a sample at normal incidence and in TM-polarization, with a numerical aperture comparable to the linear-optical measurements. Figure 3.5 characterizes the laser pulses, emphasizing the high temporal resolution. The THG intensity is detected by the CCD camera attached to the spectrometer.

Figure 7.3 shows a typical data set of sample MPCS-*A*, containing 600 individual spectra obtained in a total of about 8 minutes acquisition time. Here, the THG signal is plotted on a linear gray scale as a function of spectrometer photon energy and interferometric time delay. Exactly the same representation has already been employed in the theory section 6.2. Indeed, the nonlinear data of Figs. 6.2 and 6.3 shown there are based on linear-optical parameters corresponding to those of sample MPCS-*A* here [compare also Fig. 7.2(a)]. Obviously, the measured nonlinear-optical spectra in Fig. 7.3(a) are in very good agreement with those in Fig. 6.2(a), much more than with any of the spectra in Fig. 6.3. In particular, four peaks occur in the experimental spectra at zero time delay. Also, the dependencies of the different spectral cuts versus time delay in Fig. 7.3(b) are in very good agreement with those in Fig. 6.2(b). Again, the envelopes of the first and fourth cuts show hardly any beating, whereas the envelopes of the second and third cuts reveal a pronounced beating behavior [note that the very weak fourth peak in Fig. 7.3(a) spectrally overlaps with the wing of the third peak, resulting in a small residual beating]. This comparison allows us to conclude that the nonlinear model where only η_0 is nonzero is the appropriate one. This means that the nonlinearity predominantly originates from the particle plasmon, which is not *a priori* clear. This finding is consistent with the experimental observation that the nonlinear signal decreases by a factor of 19 (and the multi-peak features disappear) when going from TM-polarization used so far to TE-polarization (effectively switching off the plasmonic response). It is also consistent with the fact that the THG signals drop by a factor of about 20 when going from the gold nanowire arrays to areas of the glass substrate where only the dielectric layers are present.

It is important for our interpretation that the experiments are performed in the third-

order perturbation regime which is also assumed in the theoretical analysis. Higher-order contributions would obviously modify the ratio of 32:1 between the THG signal at zero time delay and that at large time delays. In the experiments, the ratio of 32:1 is reached within experimental uncertainty: From analyzing the upper envelope of spectrally integrated data similar to those shown in Fig. 7.3 but for time delays up to ± 60 fs, we derive a ratio of 24:1, from the corresponding lower envelope we obtain a ratio of 35:1. The actual ratio, which refers to a comparison between zero and infinite time delay, must lie between these two ratios.

In Fig. 7.4, we show the data set for the "nonresonant" sample MPCS-*B*. As for sample MPCS-*A*, four spectral peaks are visible in the THG spectra. In contrast, however, the peaks in Fig. 7.4(a) have rather different spectral widths. This can be understood from the fact that the two effective extinction peaks [see Fig. 7.2(b)] exhibit rather different spectral widths and from our discussion of section 6.2. The different spectral widths in Fig. 7.4(a) correspond to strongly different decay times of the envelopes in Fig. 7.4(b). Again, only the envelopes of the first and fourth cuts show a smooth decay, whereas the envelopes of the second and third cuts exhibit a pronounced beating.

Hence, our experiments reveal that different spectral components of the third-harmonic signal can exhibit substantially different temporal dynamics. This information would obviously not be available from a spectrally integrated experiment [30].
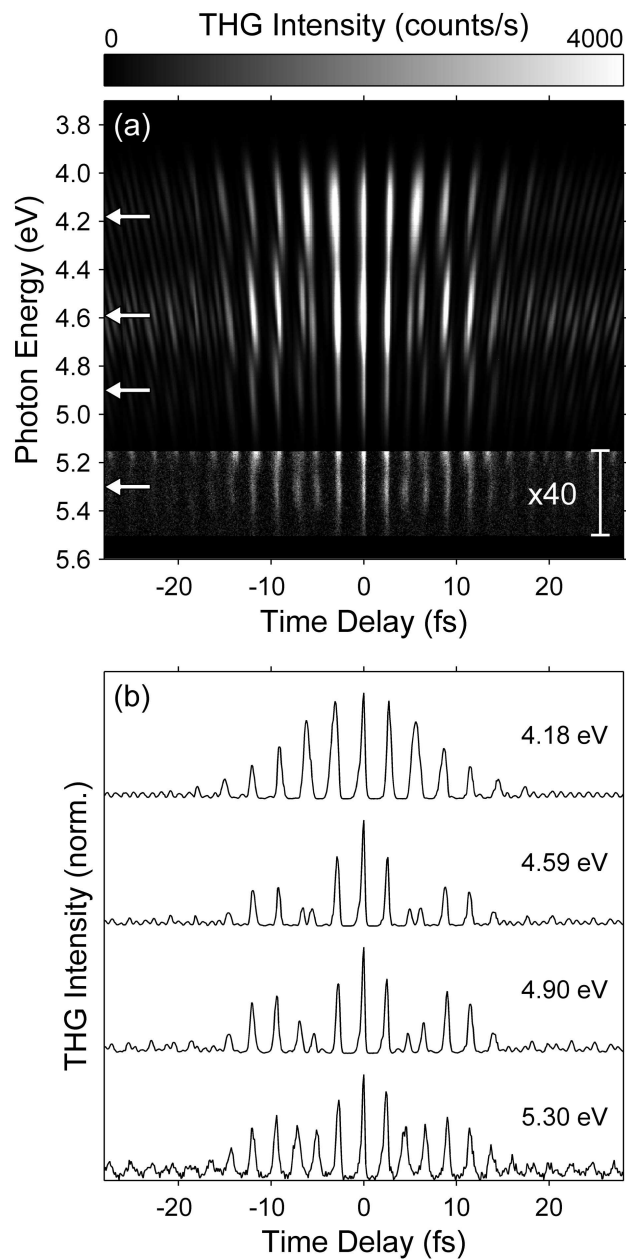
Figure 7.3: (a) Measured THG intensity from sample MPCS-*A*. The THG intensity is shown on a saturated gray scale, versus spectrometer photon energy and interferometric time delay. Near time delay $T=0$, the THG spectrum exhibits four peaks (the weak high-energy peak is amplified by a factor of 40 to become visible). The four peaks exhibit a different temporal behavior. Corresponding cuts at the spectral peak positions indicated by the white arrows in (a) are shown in (b). For better comparison, the curves are normalized to the same maximum and are vertically displaced. The appearance and absence of beating is discussed in the text. Compare with the corresponding theory (Fig. 6.2).
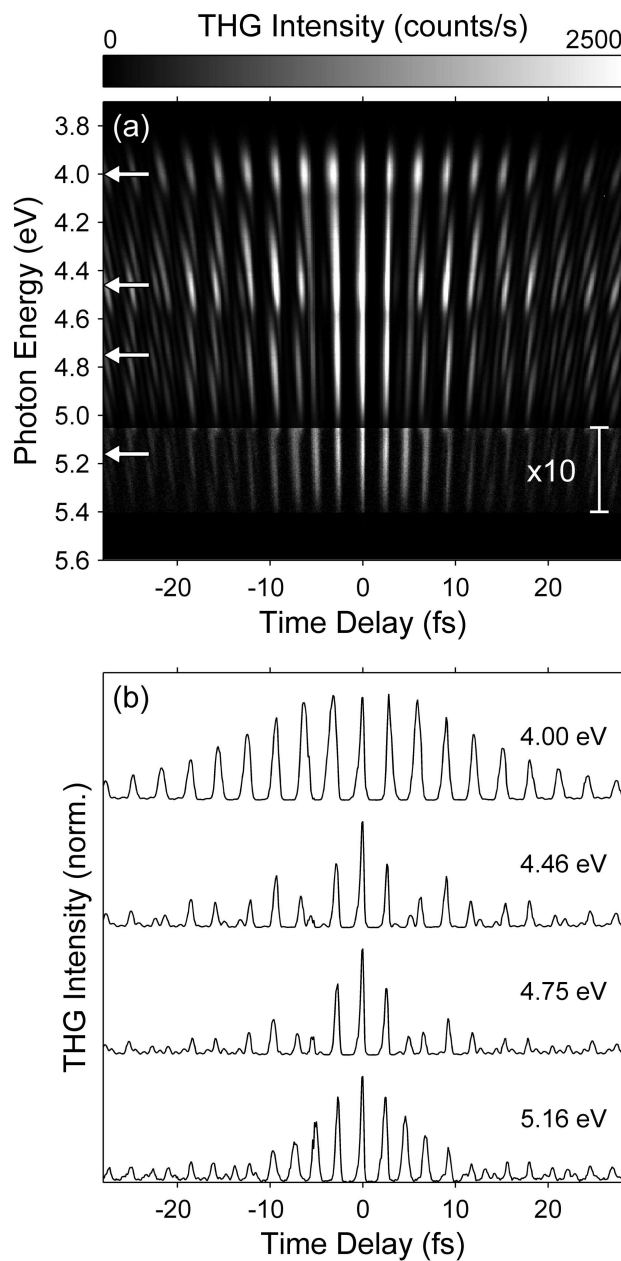
Figure 7.4: (a) Measured optical THG intensity from sample MPCS-*B*. Near $T=0$, the THG spectrum clearly exhibits four peaks (the high-energy peak is amplified by a factor of 10). Normalized cuts at the spectral peak positions indicated by the white arrows in (a) are shown in (b). Note the much slower, smooth decay of the envelope of the cut at 4.00 eV as compared to the cut at 5.16 eV, and the beating, which only occurs in the other two curves.

Chapter 8

Nonlinear optics of planar Metamaterials: Theory

During the last few years, various numerical calculations have confirmed that the linear (optical) properties of Metamaterials working at frequencies ranging from the microwave to optical frequencies can very well be described by the Maxwell equations (2.1) and the Drude model for the metal permittivity (cf. section 2.3). Sometimes, the results have been interpreted in terms of effective material parameters of a Metamaterial, i.e., an effective permittivity and permeability (cf. section 2.5). We do not follow this route for linear or nonlinear optics.

So far, theoretical publications on nonlinear-optical Metamaterials have addressed new options regarding optical bistability [75, 82], Second-Harmonic Generation [77, 131], parametric nonlinear processes [132, 133], and nonlinear sub-wavelength imaging [134]. Most of these publications assume a given nonlinearity (nonlinear susceptibility) which is not discussed or motivated further. In contrast, we present here a theory containing a straightforward microscopic nonlinear mechanism. This theory is based on the Lorentz force acting on the mobile metal electrons usually present in Metamaterials, and does not need any further (unknown) parameters beyond those already fixed for linear optics. The theory has been developed in the groups of S. W. Koch and J. V. Moloney [135, 136]. Corresponding numerical simulations are under investigation in the latter group, but we additionally present own simulation results here.

In this chapter, we present the theory and data to be compared with some of the experiments on Metamaterials (see chapter 9). We start by describing the linear-optical properties of planar Metamaterials consisting of Split-Ring Resonators (SRRs) in section 8.1. Next, we derive our nonlinear theory analytically (section 8.2), with focus on perturbative Second-Harmonic Generation. In preparation for our simulations, we develop an approximation for normal and oblique incidence in section 8.3. The actual numerical results of the simulations, based on the magnetic part of the Lorentz force, are presented in section 8.4.
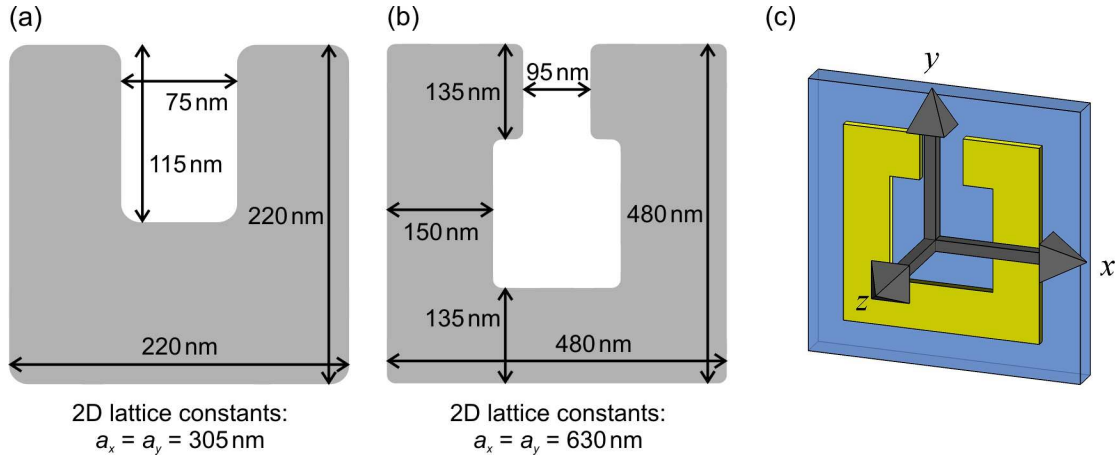
Figure 8.1: Geometric parameters of the simulated Split-Ring Resonators, for designs (a) META-*A* and (b) META-*B*. In both cases, the SRR thickness is Δz=25 nm and the radius of curvature is half the thickness. (c) Scheme of the coordinate system we use. The "horizontal" ("vertical") direction is parallel to the x-axis (y-axis).

8.1   Linear optics of Split-Ring Resonators

The three fundamental resonances of SRRs have been introduced schematically in section 2.5.1 [see Fig. 2.5(d)-(f)]. Here, we discuss the details of the linear-optical properties of SRRs for two concrete examples, named designs META-*A* and META-*B* (these correspond to the principal experimental samples in chapter 9). Each example consists of gold SRRs with a certain geometry (see Fig. 8.1) arranged in an infinite 2D lattice (square grid). This planar array with thickness Δz=25 nm is located on top of a half-space of glass, the remaining volume is air. For gold, we use the Drude permittivity ε_D described in section 2.3, for the glass substrate we use a refractive index of $n_\mathrm{sub}=\sqrt{\varepsilon_\mathrm{sub}}$=1.5, and for air we use $n_\mathrm{air}=\sqrt{\varepsilon_\mathrm{air}}$=1. We employ the finite-element method described in chapter 4 to simulate the linear-optical electric field $\hat{\boldsymbol{E}}^{(1)}(\boldsymbol{r})$ for the frequency domain and compute transmittance spectra.

Normal incidence

For normal incidence, calculated transmittance spectra are shown in Fig. 8.2 for design META-*A* and META-*B*, and horizontal and vertical polarization of the exciting plane wave. Each transmittance minimum corresponds to the excitation of a particular resonance [14, 89]. The parameters of the designs are chosen such that resonances of different types appear around the particular wavelength of 1.5 μm (corresponding to the excitation wavelength in our nonlinear-optical experiments, see chapter 9). The magnetic, horizontal electric, and vertical electric resonances are thus connected with design META-*A* in horizontal, META-*B* in horizontal, and META-*B* in vertical polarization, respectively. Design META-*A* in vertical polarization is nonresonant at 1.5 μm wavelength.

These correspondences are supported by considering the metal electron velocity field distributions inside the SRRs, shown in Fig. 8.3. Three of the field patterns shown there can easily be related to the three fundamental resonances depicted in Fig. 2.5(d)-(f). The
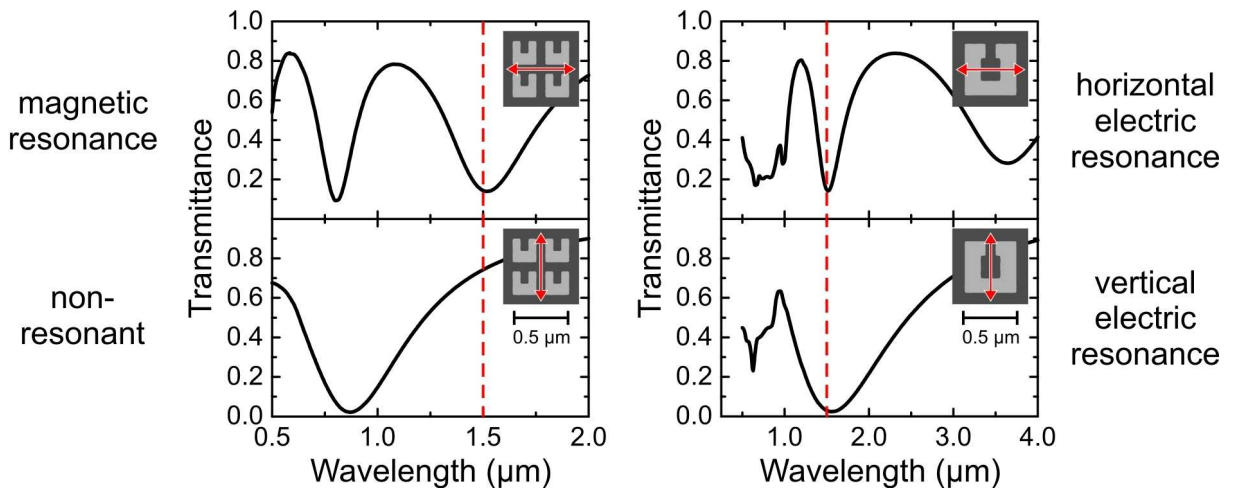
Figure 8.2: Simulated linear-optical transmittance spectra for normal incidence. The left (right) column corresponds to design META-*A* (META-*B*), the top (bottom) row to excitation with horizontal (vertical) polarization, as indicated by the red arrows in the insets depicting the SRRs. Because of the character of resonances (not) appearing at $1.5\,\mu\mathrm{m}$ wavelength (dashed red line), we call these four cases, as denoted, the magnetic resonance, the nonresonant case, the horizontal electric resonance, and the vertical electric resonance, respectively. [Confer also Figs. 8.3 and 2.5(d)-(f).] Compare to the corresponding experiments (Fig. 9.2).
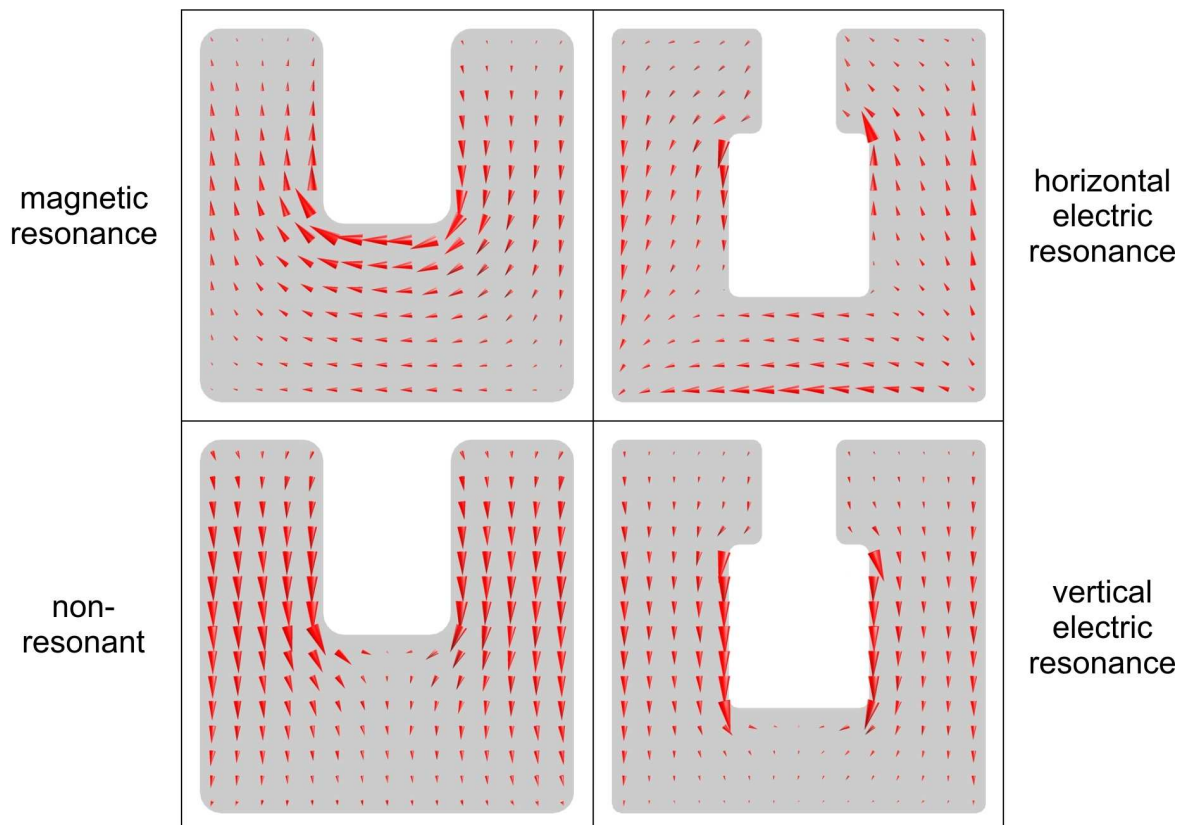
Figure 8.3: Snapshots of the metal electron velocity field $\mathrm{Re}[\hat{\boldsymbol{v}}^{(1)}(\boldsymbol{r})]$ for the four cases discussed in the text. The electric field and the current density inside the SRRs are also proportional to the shown fields. Each of the field distributions is shown on its own scale of field strength. In the left column, the actually smaller SRRs are shown on a larger scale, for better comparison of the field patterns.
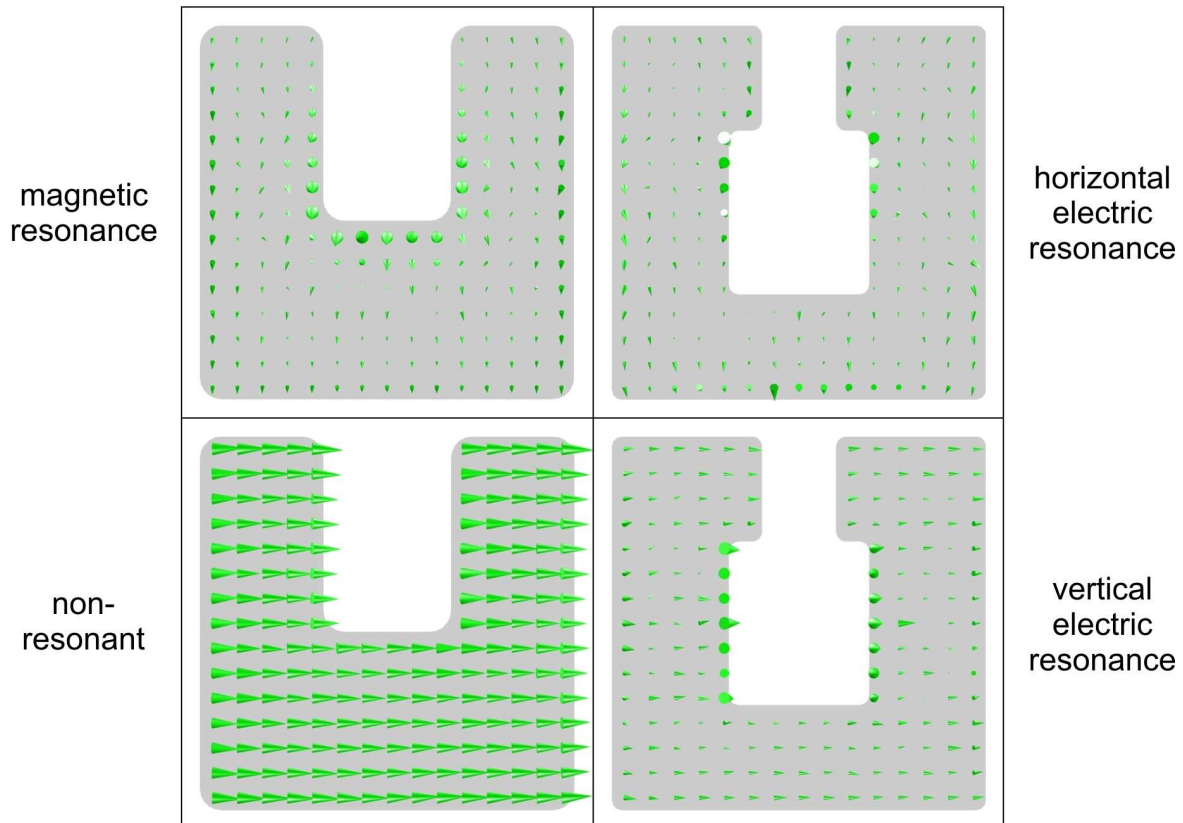
Figure 8.4: Snapshots of the magnetic field $\mathrm{Re}[\hat{\boldsymbol{B}}^{(1)}(\boldsymbol{r})]$ inside the SRRs, shown in analogy to Fig. 8.3. The local magnetic fields of the three resonant SRRs are mainly based on the electronic currents inside the SRRs: The currents lead to magnetic fields with prominent components normal to the SRR plane. In contrast, the magnetic field of the nonresonant SRR (bottom left) stems mainly from the incident wave. Again, each of the field distributions is shown on its own scale of field strength. (In fact, the field in the nonresonant case is much smaller in magnitude than for all other cases.)

electron velocity $\hat{\boldsymbol{v}}^{(1)}(\boldsymbol{r})$ is computed from the electric field by $\hat{\boldsymbol{v}}^{(1)}(\boldsymbol{r}) = -\mathrm{i}\omega\varepsilon_0(\varepsilon_\mathrm{D} - 1)\hat{\boldsymbol{E}}^{(1)}(\boldsymbol{r})/[(-e)n_e]$ (cf. section 2.3) for the frequency $\omega = 2\pi c_0/(1.5\,\mu\mathrm{m}) = 2\pi \times 200\,\mathrm{THz}$. The nonresonant character of the remaining case (Fig. 8.3, bottom left) can be seen from the magnetic field distributions (inside the SRRs), shown in Fig. 8.4. There, the nonresonant case (bottom left) shows a magnetic field which mainly stems from the incident electromagnetic wave, whereas in the other, resonant cases, the local magnetic field mainly stems from the large local electronic currents. Note that for the resonances with magnetic dipole moment (top row) the strongest magnetic field is directed perpendicular to the plane of the SRR.

Oblique incidence

For the three resonant cases, we show calculated linear transmittance spectra for oblique incidence in Fig. 8.5. The left column is for P-polarization, the right column for S-polarization. The schemes adjacent to the spectra show the corresponding configurations of the incident fields (the directions of the wave vector $\boldsymbol{k}$, the electric field $\boldsymbol{E}$, and the magnetic field $\boldsymbol{B}$). In S-polarization, the normal component (with respect to the substrate) of the magnetic field changes sign when going from positive angles of incidence (see schemes) to negative angles with flipped $\boldsymbol{k}$ (not shown). This means that positive and negative angles of incidence do not necessarily lead to equal results. The simulated transmittance spectra in Fig. 8.5 are thus shown for positive angles (solid curves) as well as for negative angles (dots). We find, however, no significant differences for opposite angles. This means that the incident magnetic field does not couple strongly to the SRRs and does not excite significant electronic currents interfering with the prominent currents excited by the incident electric field.

In detail, the transmittance spectra of Fig. 8.5(a) are associated with the magnetic resonance at $1.5\,\mu\mathrm{m}$ wavelength and show only a slight dependence on the angle of incidence. A stronger dependence can be observed in (b) for the horizontal electric resonance at $1.5\,\mu\mathrm{m}$ wavelength, which for increasing angle of incidence slightly shifts to longer wavelengths for S-polarization, but shifts substantially and becomes less pronounced for P-polarization. In (c), the vertical electric resonance at $1.5\,\mu\mathrm{m}$ wavelength also shifts substantially for P-polarization, but not for S-polarization. In the latter case, however, the resonance splits into two resonances (corresponding to two transmittance minima), as has been observed and explained in [89]: For normal incidence, the electronic currents in the two side arms of the SRRs flow in parallel in the vertical direction (one resonance), but for S-polarization, the currents in the two side arms can have a phase shift, and modes with predominantly parallel and anti-parallel flow can be excited (two distinct resonances). In [89], also more data have been shown which are similar to ours and confirm our results.

In order to allow for a direct comparison with the experiments, all shown transmittance values are normalized to the transmittance through the bare substrate (both surfaces) for the corresponding angle of incidence, by using the Fresnel formulas (2.14).

The transmittance values for zero angle of incidence in Fig. 8.5 match the corresponding normal-incidence spectra of Fig. 8.2, although the employed numerical methods (regarding perfectly matched layers and the order of vector elements, see chapter 4) are different. This agreement confirms each calculation.
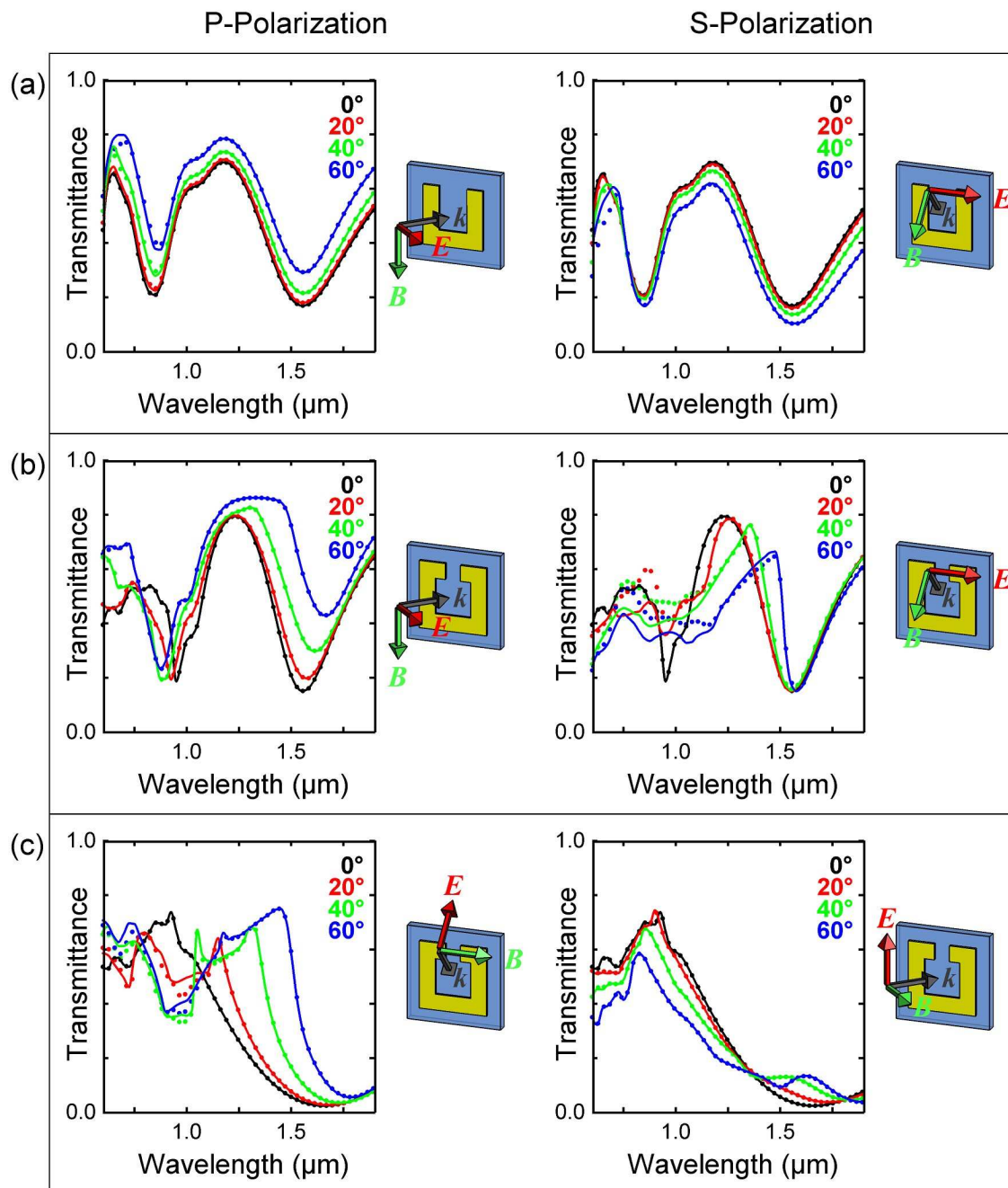
Figure 8.5: Simulated linear-optical transmittance spectra for oblique incidence, for the cases with a resonance near 1.5 μm wavelength: (a) magnetic resonance (design META-*A* and horizontal polarization), (b) horizontal electric resonance (design META-*B* and horizontal polarization), (c) vertical electric resonance (design META-*B* and vertical polarization). The left column is for P-polarization, the right column for S-polarization. Transmittance spectra for positive angles (solid curves) and negative angles (dots) are shown, the angle of incidence with respect to the surface normal is indicated by the color. The schemes adjacent to the spectra show the configuration of the incident fields for positive angles of incidence. Compare to the corresponding experiments (Fig. 9.10).

8.2 Nonlinear optics of metals: The fluid-dynamic approach

In this section, we derive our general nonlinear theory for Metamaterials. This theory will be the basis for our investigations in the later sections. The nonlinear theory is based on the (nonlinear) Lorentz force acting on the metal electrons and is a natural extension of the linear description of metals as explained in section 2.3. The theory has been formulated within the groups of S. W. Koch and J. V. Moloney [135, 136] and follows an approach based on the Vlasov-Maxwell equations in the classical limit [135, 137], similar to fluid dynamics. Here, we will first trace the general time-domain formulation and then switch to the frequency domain to describe the linear optics and the perturbative nonlinear optics.

Time domain

We start by considering the background permittivities of the half-spaces of the glass substrate and air,

$$\varepsilon_{\text{bg}}(\boldsymbol{r}) = \left\{ \begin{array}{ll} \varepsilon_{\text{sub}}\,, & z < 0 \\ 1\,, & z \geqslant 0\,. \end{array} \right. \tag{8.1}$$

Correspondingly, we regard the metal electrons (and the immobile ions) in terms of free charges ρ and currents $\boldsymbol{j}$ appearing in the Maxwell equations (2.1). The metallic SRRs residing in the half-space of air, just touching the substrate, enter with their detailed geometry by defining a space-dependent, equilibrium, metal electron density

$$n_0(\boldsymbol{r}) = \left\{ \begin{array}{ll} n_e\,, & \boldsymbol{r} \text{ inside SRRs} \\ 0\,, & \text{else}\,, \end{array} \right. \tag{8.2}$$

where n_e is the same as in section 2.3. At a time t, the actual electron density is $n(\boldsymbol{r}, t)$. Defining $q = -e$, the total electronic charge density then becomes

$$qn(\boldsymbol{r}, t) = qn_0(\boldsymbol{r}) + \rho(\boldsymbol{r}, t)\,, \tag{8.3}$$

where ρ is the net charge including both the electrons and the metal-ion background. In the following, also all vector quantities are space- and time-dependent, and we omit these dependencies for the sake of conciseness. The electronic current density $\boldsymbol{j}$ and the electron velocity $\boldsymbol{v}$ are related via

$$\boldsymbol{j} = qn\boldsymbol{v}\,. \tag{8.4}$$

Now we assume that each electron feels a force $\boldsymbol{F}$, which consists of the electric and magnetic part of the Lorentz force, and additionally the damping term in analogy to the derivation in section 2.3,

$$\boldsymbol{F} = q(\boldsymbol{E} + \boldsymbol{v} \times \boldsymbol{B}) - m_e \gamma_{\text{c}} \boldsymbol{v}\,. \tag{8.5}$$

We do not want to follow each electron on its trajectory but rather want to describe the space-dependent flow field $\boldsymbol{v}$, like in fluid dynamics, and consequently derive differential equations describing the dynamics of continuum quantities. Thus, we introduce the force

density $\boldsymbol{f} = n\boldsymbol{F}$. Then, the evolution of the current density is given by

$$
\begin{aligned}
\partial_t \boldsymbol{j} &= \left[\frac{d}{dt}\boldsymbol{j}\right] - \left[(\boldsymbol{v}\cdot\nabla)\boldsymbol{j}\right] \\
&= \left[qn\frac{d}{dt}\boldsymbol{v} + \boldsymbol{v}\left(\frac{d}{dt}(qn)\right)\right] - \left[\boldsymbol{v}(\boldsymbol{v}\cdot\nabla)(qn) + qn(\boldsymbol{v}\cdot\nabla)\boldsymbol{v}\right] \\
&= \left[qn\frac{\boldsymbol{F}}{m_e} + \boldsymbol{v}\left(\partial_t(qn) + (\boldsymbol{v}\cdot\nabla)(qn)\right)\right] - \left[\boldsymbol{v}(\boldsymbol{v}\cdot\nabla)(qn) + (\boldsymbol{j}\cdot\nabla)\boldsymbol{v}\right] \\
&= \left[q\frac{\boldsymbol{f}}{m_e} + \boldsymbol{v}\left(-\nabla\cdot\boldsymbol{j}\right)\right] - \left[(\boldsymbol{j}\cdot\nabla)\boldsymbol{v}\right] \\
&= \frac{q}{m_e}\boldsymbol{f} - \sum_k \partial_k\left(\boldsymbol{v}j_k\right) \\
&= \frac{q}{m_e}\boldsymbol{f} - \sum_k \partial_k\left(\frac{\boldsymbol{j}j_k}{qn_0 + \rho}\right).
\end{aligned}
\tag{8.6}
$$

Here, we have used the relation $d/dt = \partial/\partial t + (\boldsymbol{v}\cdot\nabla)$ several times, and for the fourth equation, we have employed the charge conservation law Eq. (2.2). Inserting the force density $\boldsymbol{f}$ based on Eq. (8.5) into Eq. (8.6) yields the time derivative of the current density

$$
\partial_t \boldsymbol{j} = \frac{q}{m_e}\left[(qn_0 + \rho)\boldsymbol{E} + \boldsymbol{j}\times\boldsymbol{B}\right] - \gamma_{\mathrm{c}}\boldsymbol{j} - \sum_k \partial_k\left(\frac{\boldsymbol{j}j_k}{qn_0 + \rho}\right).
\tag{8.7}
$$

Taking Eq. (8.7) together with the Maxwell equations (2.1) as well as the equations $\boldsymbol{D} = \varepsilon_0\varepsilon_{\mathrm{bg}}\boldsymbol{E}$ and $\boldsymbol{B} = \mu_0\boldsymbol{H}$ forms the complete set of equations describing the dynamics of the nonlinear system.

   We will discuss different orders of nonlinearity below. Here, we state that the system is nonlinear to any order because of several product terms appearing in Eq. (8.7). Hence, in the time domain, e.g., SHG, THG, and higher-order harmonics can be investigated by simulating the described set of equations. Using a finite-difference time-domain method [105, 106] and normal-incidence conditions, this approach is followed in the ongoing Metamaterial simulations of J. Förstner of the group of J. V. Moloney (Tucson, USA). However, convergence issues have not permitted stable results so far [136].

Frequency domain

We now take a perturbative approach by switching to the frequency domain (cf. section 2.1.2). Assuming a monochromatic excitation with frequency ω_0, the first-order electric field is $\boldsymbol{E}^{(1)}(\boldsymbol{r}, t) = \hat{\boldsymbol{E}}^{(1)}(\boldsymbol{r})\,\mathrm{e}^{-\mathrm{i}\omega_0 t}$, and similarly for other fields. For linear optics, all nonlinearities in Eq. (8.7) have to be neglected, leading to

$$
(-\mathrm{i}\omega_0)\,\hat{\boldsymbol{j}}^{(1)} = \frac{q}{m_e}qn_0\hat{\boldsymbol{E}}^{(1)} - \gamma_{\mathrm{c}}\hat{\boldsymbol{j}}^{(1)}
\tag{8.8}
$$

or

$$
\hat{\boldsymbol{j}}^{(1)} = \mathrm{i}\varepsilon_0 \frac{\omega_{\mathrm{pl}}^2(\boldsymbol{r})}{\omega_0 + \mathrm{i}\gamma_{\mathrm{c}}}\,\hat{\boldsymbol{E}}^{(1)},
\tag{8.9}
$$

where $\omega_{\mathrm{pl}}(\boldsymbol{r}) = \sqrt{n_0(\boldsymbol{r})e^2/(\varepsilon_0 m_e)}$ corresponds to the usual plasma frequency (cf. section 2.3) inside the SRRs and to zero outside.

With $\hat{\boldsymbol{j}}^{(1)}$ appearing as a free current density, the Maxwell equations (2.1) together with $\mu = 1$ lead to the linear wave equation

$$\nabla \times \nabla \times \hat{\boldsymbol{E}}^{(1)} - \frac{\omega_0^2}{c_0^2} \varepsilon_{\mathrm{bg}} \hat{\boldsymbol{E}}^{(1)} = \mathrm{i}\omega_0\mu_0 \hat{\boldsymbol{j}}^{(1)} \,. \tag{8.10}$$

Inserting Eq. (8.9) into Eq. (8.10) and defining the full permittivity

$$\varepsilon_{\mathrm{full}}(\boldsymbol{r}, \omega_0) = \begin{cases} \varepsilon_{\mathrm{sub}}\,, & z < 0 \\ 1\,, & z \geqslant 0 \text{ and } \boldsymbol{r} \text{ not inside SRRs} \\ \varepsilon_D(\omega_0)\,, & \boldsymbol{r} \text{ inside SRRs}\,, \end{cases} \tag{8.11}$$

allows to write the linear wave equation in its usual form:

$$\nabla \times \nabla \times \hat{\boldsymbol{E}}^{(1)} - \frac{\omega_0^2}{c_0^2} \varepsilon_{\mathrm{full}}(\boldsymbol{r}, \omega_0) \hat{\boldsymbol{E}}^{(1)} = 0 \,. \tag{8.12}$$

The Drude permittivity $\varepsilon_D(\omega)$ for the metal has been introduced in section 2.3. Equation (8.12) shows that the ansatz of our theory, the force in Eq. (8.5), leads to the known linear-optical relations.

We now turn to the case of Second-Harmonic Generation. As a preparation step, we clarify the nature of multiplications which will appear. Let us consider three general physical quantities A, B, and C which are related by some multiplication in the time domain, i.e., $C(t) = A(t) \bullet B(t)$. If A and B oscillate with frequency ω_0, we can write $A = \hat{A}^{(1)}\,\mathrm{e}^{-\mathrm{i}\omega_0 t}$ and $B = \hat{B}^{(1)}\,\mathrm{e}^{-\mathrm{i}\omega_0 t}$ in the "lax" formulation (see section 2.1.2), however, we have to remember that the physically relevant parts are only the real parts. Hence we can relate the complex-valued quantities A, B, and C by

$$\begin{aligned} \mathrm{Re}(C) &= \mathrm{Re}(A) \bullet \mathrm{Re}(B) \\ &= \frac{1}{2}\mathrm{Re}[A \bullet B + A \bullet B^*]\,, \end{aligned} \tag{8.13}$$

where B^* is the complex-conjugate of B. It is important to note that the first summand in Eq. (8.13) oscillates with the frequency $2\omega_0$ and the second summand is constant in time. Hence, the products leading to second-harmonic generation and those leading to optical rectification can easily be distinguished. Here, we are only interested in the SHG term at frequency $2\omega_0$, and the amplitude of the SHG part of C is simply

$$\hat{C}^{(\mathrm{SHG})} = \frac{1}{2}\,\hat{A}^{(1)} \bullet \hat{B}^{(1)} \,. \tag{8.14}$$

Note that the factor $\frac{1}{2}$ is the same as in Eq. (2.23).

With this preparation, we are ready to express Eq. (8.7) for second-order amplitudes, limited to the SHG parts:

$$\begin{aligned} (-2\mathrm{i}\omega_0)\,\hat{\boldsymbol{j}}^{(\mathrm{SHG})} &= \frac{q}{m_e}\left[qn_0\hat{\boldsymbol{E}}^{(\mathrm{SHG})} + \frac{1}{2}\,\hat{\rho}^{(1)}\hat{\boldsymbol{E}}^{(1)} + \frac{1}{2}\,\hat{\boldsymbol{j}}^{(1)} \times \hat{\boldsymbol{B}}^{(1)}\right] \\ &\quad - \gamma_{\mathrm{c}}\hat{\boldsymbol{j}}^{(\mathrm{SHG})} - \sum_k \partial_k\left(\frac{1}{2}\,\frac{\hat{\boldsymbol{j}}^{(1)}\hat{j}_k^{(1)}}{qn_0}\right) \,. \end{aligned} \tag{8.15}$$

Applying a similar procedure as for linear optics, we obtain the wave equation for SHG

$$\nabla \times \nabla \times \hat{\boldsymbol{E}}^{(\text{SHG})} - \frac{(2\omega_0)^2}{c_0^2} \varepsilon_{\text{full}}(\boldsymbol{r}, 2\omega_0)\hat{\boldsymbol{E}}^{(\text{SHG})} = -\frac{1}{2}\frac{1}{1 + \text{i}\gamma_c/(2\omega_0)}\frac{1}{c_0^2}\hat{\boldsymbol{S}}^{(\text{SHG})} \quad (8.16)$$

with the total SHG source term

$$\hat{\boldsymbol{S}}^{(\text{SHG})}(\boldsymbol{r}) = \frac{q}{\varepsilon_0 m_e}\left[\hat{\rho}^{(1)}\hat{\boldsymbol{E}}^{(1)} + \hat{\boldsymbol{j}}^{(1)} \times \hat{\boldsymbol{B}}^{(1)}\right] - \sum_k \partial_k \left(\frac{\hat{\boldsymbol{j}}^{(1)}\hat{j}_k^{(1)}}{\varepsilon_0 q n_0}\right). \quad (8.17)$$

The total SHG source term $\hat{\boldsymbol{S}}^{(\text{SHG})}$ contains three summands. The first source term (which we call ρE-term) only has nonzero-values at the metal surfaces where charge accumulation occurs in linear optics; it describes a second-order reaction of the surface charges to their own electric field. The second term ($j \times B$-term) is only nontrivial in the metal volume, and simply results from the magnetic part of the Lorentz force. We exemplarily show this term in Fig. 8.7 for the four SRRs cases discussed earlier. Finally, the third source term (jj-term) contains contributions both at the metal surfaces and the metal volume and stems from the transformation to the continuum formulation. This term is related to the advection appearing in fluid dynamics.

We briefly note that, by using the relations

$$\hat{\rho}^{(1)} = \varepsilon_0 \nabla \cdot \left(\varepsilon_{\text{bg}}\hat{\boldsymbol{E}}^{(1)}\right), \quad (8.18\text{a})$$

$$\hat{\boldsymbol{j}}^{(1)} = \text{i}\varepsilon_0\frac{\omega_{\text{pl}}^2(\mathbf{r})}{\omega_0 + \text{i}\gamma_c}\hat{\boldsymbol{E}}^{(1)}, \quad (8.18\text{b})$$

$$\hat{\boldsymbol{B}}^{(1)} = \frac{1}{\text{i}\omega_0}\nabla \times \hat{\boldsymbol{E}}^{(1)}, \quad (8.18\text{c})$$

the source terms in Eq. (8.17) can be rewritten only in terms of the electric field,

$$\begin{aligned}\hat{\boldsymbol{S}}^{(\text{SHG})} = \frac{q}{m_e}\Bigg[&\hat{\boldsymbol{E}}^{(1)}\left(\nabla \cdot \left\{\varepsilon_{\text{bg}}\hat{\boldsymbol{E}}^{(1)}\right\}\right) \\ &+ \frac{\omega_{\text{pl}}^2(\mathbf{r})}{\omega_0(\omega_0 + \text{i}\gamma_c)}\hat{\boldsymbol{E}}^{(1)} \times \left(\nabla \times \hat{\boldsymbol{E}}^{(1)}\right) \\ &+ \frac{1}{(\omega_0 + \text{i}\gamma_c)^2}\sum_k \partial_k\left(\omega_{\text{pl}}^2(\mathbf{r})\hat{\boldsymbol{E}}^{(1)}\hat{E}_k^{(1)}\right)\Bigg].\end{aligned} \quad (8.19)$$

Here, it is not obvious whether one term dominates others in strength, because in the first line, the strong electric fields outside the metallic SRRs are important, and for the volume terms in the other lines, equally strong pre-factors appear.

In conclusion, Eqs. (8.16) and (8.17) describe a microscopic theory which constructively explains a mechanism of Second-Harmonic Generation. We will investigate the sources in more detail in the following. This includes numerical simulations based on the known linear electric field $\hat{\boldsymbol{E}}^{(1)}$ (see section 8.1). Here, we additionally note that for Third-Harmonic Generation based on Eq. (8.7), a total of seven source terms would have to be considered, six of which depend on the self-consistent SHG fields like $\hat{\boldsymbol{E}}^{(\text{SHG})}$. The latter fields, however, are not easily available.

8.2.1 Symmetry considerations

Is this theory for SHG in agreement with the usual selection rules [32] known for SHG on planar structures of certain symmetry and normal-incidence excitation? In order to investigate this point, we pick a coordinate system as depicted in Fig. 8.1(c).

Let us first consider a centrosymmetric medium for which $n_0(-x,-y,z) = n_0(x,y,z)$ holds. The selection rules [32] would not allow for radiated SHG into the $\pm z$ directions in this case. It is straightforward to derive, e.g., the following relations:

$$\hat{E}_{x,y}^{(1)}(-x,-y,z) \;=\; +\,\hat{E}_{x,y}^{(1)}(x,y,z)\,, \tag{8.20a}$$

$$\hat{E}_{z}^{(1)}(-x,-y,z) \;=\; -\,\hat{E}_{z}^{(1)}(x,y,z)\,, \tag{8.20b}$$

$$\hat{\rho}^{(1)}(-x,-y,z) \;=\; -\,\hat{\rho}^{(1)}(x,y,z)\,, \tag{8.20c}$$

$$\hat{S}_{x,y}^{(\mathrm{SHG})}(-x,-y,z) \;=\; -\,\hat{S}_{x,y}^{(\mathrm{SHG})}(x,y,z)\,, \tag{8.20d}$$

$$\hat{S}_{z}^{(\mathrm{SHG})}(-x,-y,z) \;=\; +\,\hat{S}_{z}^{(\mathrm{SHG})}(x,y,z)\,. \tag{8.20e}$$

The sources $\hat{\boldsymbol{S}}^{(\mathrm{SHG})}(-x,-y,z)$ and $\hat{\boldsymbol{S}}^{(\mathrm{SHG})}(x,y,z)$, however, lead to radiation fields which interfere. At a point within the far field in the $(0,0,\pm 1)$ direction, the tangential (xy) parts of the radiation fields interfere destructively to zero because of Eq. (8.20d). A longitudinal component based on $\hat{S}_{z}^{(\mathrm{SHG})}$, in turn, cannot be radiated into the forward or backward directions at all. Thus, no SHG radiation can be observed in the far-field forward or backward directions for a centrosymmetric medium described by our theory, which agrees with the selection rules.

Our SRR designs [see Fig. 8.1(a) and (b)] have a mirror symmetry (C_{1v}) with respect to the x-axis, hence, $n_0(-x,y,z) = n_0(x,y,z)$ holds. Here, the considerations depend on the incident polarization. Exciting with horizontal polarization (along the x-axis), one finds, e.g., the following relations:

$$\hat{E}_{x}^{(1)}(-x,y,z) \;=\; +\,\hat{E}_{x}^{(1)}(x,y,z)\,, \tag{8.21a}$$

$$\hat{E}_{y,z}^{(1)}(-x,y,z) \;=\; -\,\hat{E}_{y,z}^{(1)}(x,y,z)\,, \tag{8.21b}$$

$$\hat{\rho}^{(1)}(-x,y,z) \;=\; -\,\hat{\rho}^{(1)}(x,y,z)\,, \tag{8.21c}$$

$$\hat{S}_{x}^{(\mathrm{SHG})}(-x,y,z) \;=\; -\,\hat{S}_{x}^{(\mathrm{SHG})}(x,y,z)\,, \tag{8.21d}$$

$$\hat{S}_{y,z}^{(\mathrm{SHG})}(-x,y,z) \;=\; +\,\hat{S}_{y,z}^{(\mathrm{SHG})}(x,y,z)\,. \tag{8.21e}$$

In contrast, exciting the SRRs with vertical polarization (along the y-axis), one finds in analogy:

$$\hat{E}_{x}^{(1)}(-x,y,z) \;=\; -\,\hat{E}_{x}^{(1)}(x,y,z)\,, \tag{8.22a}$$

$$\hat{E}_{y,z}^{(1)}(-x,y,z) \;=\; +\,\hat{E}_{y,z}^{(1)}(x,y,z)\,, \tag{8.22b}$$

$$\hat{\rho}^{(1)}(-x,y,z) \;=\; +\,\hat{\rho}^{(1)}(x,y,z)\,, \tag{8.22c}$$

$$\hat{S}_{x}^{(\mathrm{SHG})}(-x,y,z) \;=\; -\,\hat{S}_{x}^{(\mathrm{SHG})}(x,y,z)\,, \tag{8.22d}$$

$$\hat{S}_{y,z}^{(\mathrm{SHG})}(-x,y,z) \;=\; +\,\hat{S}_{y,z}^{(\mathrm{SHG})}(x,y,z)\,. \tag{8.22e}$$

Because of Eqs. (8.21d) and (8.22d), a SHG wave radiated into the far-field forward or backward direction cannot have a polarization component in the x-direction. The only allowed polarization of such a SHG wave must be parallel to the y-direction, due to Eqs. (8.21e) and (8.22e). This again agrees with the selection rules [32]. We note that Eqs. (8.21d), (8.21e), (8.22d), and (8.22e) do not only hold for the symmetry of $\hat{\boldsymbol{S}}^{(\mathrm{SHG})}$, but in analogy also for each of the three summands in Eq. (8.17), that is, for the ρE-term, the $j \times B$-term, and the jj-term individually. We do not discuss mixed (xy) excitation here.

8.3   Nonlinear radiation of planar Metamaterials

Our aim is the numerical investigation of perturbative SHG of the Metamaterial examples, based on the theory presented in the preceding section. In principle, FEMLAB delivers the linear-optical fields which enter in Eq. (8.17). First, however, the question of convergence arises for linear and nonlinear fields individually. Second, for the exact description, the far-field radiation has to be calculated self-consistently according to Eq. (8.16). We test and ensure convergence (cf. chapter 4), but the self-consistent calculation of the radiated nonlinear field cannot easily be achieved with FEMLAB. Thus, we apply an approximation, which we call Driven-Dipole Approximation (DDA) and which is based on expressions involving only linear fields. We derive corresponding formulas for radiation into the normal direction as well as oblique angles in the following sections and present numerical results in section 8.4.

8.3.1   The Driven-Dipole Approximation

For our approximation, we remember that in section 2.3.1 we have introduced an abstract harmonic oscillator to describe particle plasmon oscillations, and we remember that this abstraction has proven very successful for the theory in chapter 6.

In the same spirit, we now consider a SRR as a single harmonic oscillator. It is driven by a net force $\hat{\boldsymbol{F}}^{(\mathrm{SHG})}$, equal to the (sum or) integral over all force contributions proportional to Eq. (8.17). Provided that the driving terms at the SHG frequency are off-resonant, the displacement $\hat{\boldsymbol{r}}^{(\mathrm{SHG})}$ of the oscillator will simply be proportional to the net driving force. Since the oscillator is connected with an abstract charge (stemming from the oscillating metal electrons), it is effectively an electric dipole, which (together with the other dipoles) radiates a far-field SHG wave amplitude

$$\hat{\boldsymbol{E}}^{(\mathrm{SHG})}(|z| \to \infty) \quad \propto \quad \hat{\boldsymbol{r}}_{xy}^{(\mathrm{SHG})} \quad \propto \quad \hat{\boldsymbol{F}}_{xy}^{(\mathrm{SHG})} \quad \propto \quad \int\limits_{\text{one SRR}} \mathrm{d}^3 r' \, \hat{\boldsymbol{S}}_{xy}^{(\mathrm{SHG})}(\boldsymbol{r}') \, . \quad (8.23)$$

Here, we have also taken care of the fact that only tangential (xy) components can radiate into the far field. We additionally note that the SHG wave amplitude $\hat{\boldsymbol{E}}^{(\mathrm{SHG})}$ is proportional to the density of the described dipoles, so the integral in Eq. (8.23) is effectively an average over one unit cell of the periodic Metamaterial. Also note that, provided that the unit cell

dimensions are smaller than the SHG wavelength, the radiated far-field SHG wave is simply a plane wave (i.e., no diffraction orders other than the zeroth order appear).

The Driven-Dipole Approximation introduced this way gives a clear physical picture of the simplification. Now, we discuss an equivalent, analytical approach. The approximation is equivalent to modifying the SHG wave equation (8.16) by replacing the full permittivity by the background permittivity

$$\varepsilon_{\text{full}}(\boldsymbol{r}, 2\omega_0) \quad \rightarrow \quad \varepsilon_{\text{bg}}(\boldsymbol{r}) . \tag{8.24}$$

The loss of the frequency dependence is not critical since we will only compare results for the same excitation frequency. After the above replacement, the SHG electric far-field radiated into the $\pm z$-directions can be computed analytically. To explain the main idea, we neglect the substrate temporarily, because then Eq. (8.16) leads to the SHG electric far field

$$\hat{\boldsymbol{E}}_{\text{far field}}^{(\text{SHG})}(z) = -\mathrm{i}\frac{1}{4c_0} \frac{1}{2\omega_0 + \mathrm{i}\gamma_{\text{c}}} \mathrm{e}^{2\mathrm{i}\omega_0|z|/c_0} \frac{1}{a_x a_y} \int\limits_{\text{one unit cell}} \mathrm{d}^3 r' \, \hat{\boldsymbol{S}}_{xy}^{(\text{SHG})}(\boldsymbol{r}') . \tag{8.25}$$

Here, we have also neglected small phase factors due to the small SRR thickness Δz (which is much smaller than the SHG wavelength).

Since in the following we are only interested in relative SHG intensities $I_{\text{far field}}^{(\text{SHG})} \propto |\hat{\boldsymbol{E}}_{\text{far field}}^{(\text{SHG})}|^2$, Eqs. (8.23) and (8.25) are similarly applicable. We have thus a method for obtaining relative SHG intensities from expressions depending on the linear-optical fields only. At the same time, this method also delivers the polarization direction of the SHG wave.

8.3.2 Radiation into normal direction

During the introduction of the Driven-Dipole Approximation, we have given Eqs. (8.23) and (8.25) to support the main idea. In fact, these equations assume radiation into the $\pm z$-directions, i.e., they apply for radiation into the direction normal to the planar Metamaterial.

Because of Eq. (8.25), it is clear that we can, without further approximation, replace the sources by their spatial average

$$\hat{\boldsymbol{S}}^{(\text{SHG})}(\boldsymbol{r}) \quad \rightarrow \quad \bar{\hat{\boldsymbol{S}}}^{(\text{SHG})} = \frac{1}{a_x a_y \Delta z} \int\limits_{\text{one unit cell}} \mathrm{d}^3 r' \, \hat{\boldsymbol{S}}^{(\text{SHG})}(\boldsymbol{r}') , \tag{8.26}$$

where $\bar{\hat{\boldsymbol{S}}}^{(\text{SHG})}$ is constant and (presumably) nonzero within a slab of thickness Δz. Equation (8.25) describes the radiated field without the substrate. Taking into account the substrate or any other isotropic environment only results in an additional prefactor, which disappears when we consider ratios of intensities. Hence, in detail, we can compute the relative intensity of the radiated wave transmitted through the substrate (as in the experiments) as $I_{\text{far field}}^{(\text{SHG})} \propto \left|\bar{\hat{\boldsymbol{S}}}_{xy}^{(\text{SHG})}\right|^2$, and the polarization is simply the vectorial orientation of $\bar{\hat{\boldsymbol{S}}}_{xy}^{(\text{SHG})}$.

Additionally, we are now able to simplify the jj-term [see third line in Eq. (8.19)]. The integration appearing in Eq. (8.23), (8.25), or (8.26) is performed over the volume V of one
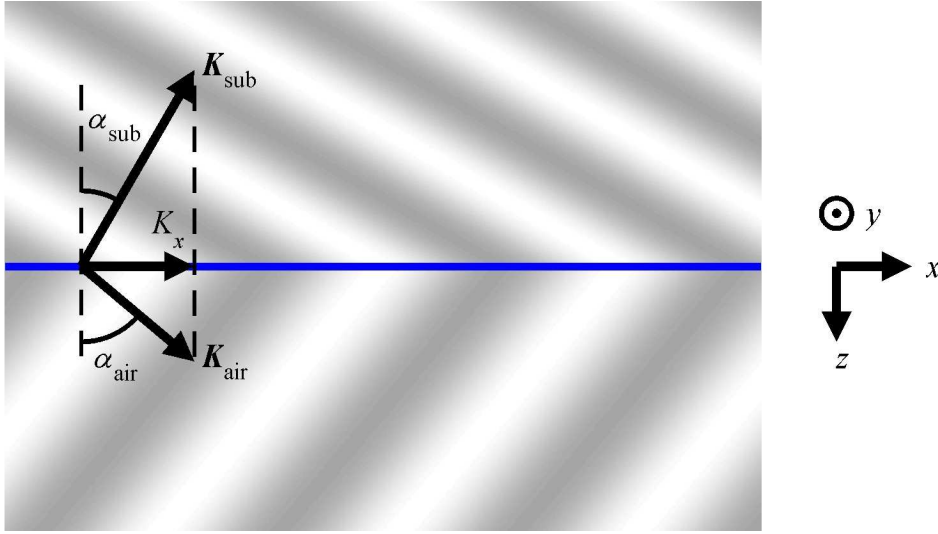
Figure 8.6: Nonlinear radiation emitted by the sources in the thin planar Metamaterial (blue line) into oblique directions. The emerging plane waves are depicted in gray scale. Corresponding wave vectors $\boldsymbol{K}_{\text{air}}$ and $\boldsymbol{K}_{\text{sub}}$ and their relation are shown by the arrows on the left, for the case of air and substrate. The arrows on the right repeat our coordinate system. In linear optics (not shown) the exciting wave would be incident onto the Metamaterial from the lower left corner of the picture.

unit cell of which the bounding surface ∂V completely lies in air and/or the substrate outside all metal. The volume integral over the appearing generalized divergence can be rewritten into a surface integral. For the l-component of the jj-term, this reads

$$
\begin{aligned}
\int_V \mathrm{d}^3 r' \left(\hat{\boldsymbol{S}}^{(\text{SHG})}_{jj,xy}(\boldsymbol{r}') \right)_l \; &\propto \; \int_V d^3 r' \sum_k \partial_k \left(\omega_{\text{pl}}^2(\boldsymbol{r}') \hat{E}^{(1)}_l \hat{E}^{(1)}_k \right) \\
&= \int_{\partial V} d\boldsymbol{A}' \, \omega_{\text{pl}}^2(\boldsymbol{r}') \hat{E}^{(1)}_l \hat{\boldsymbol{E}}^{(1)} \\
&= \; 0 \,,
\end{aligned}
\tag{8.27}
$$

because $\omega_{\text{pl}}^2(\boldsymbol{r}') \equiv 0$ on the surface ∂V. This means that within the Driven-Dipole Approximation, the jj-term does not contribute at all to SHG radiation into the normal direction.

8.3.3 Radiation into arbitrary angles

Equations (8.23) and (8.25) apply for the Driven-Dipole Approximation and radiation into $\pm z$-direction. When the Metamaterial is excited, in linear optics, with a plane wave at oblique incidence, SHG waves with oblique radiation directions appear, and different equations have to be used. It is crucial to note that in nonlinear optics, i.e., for the SHG fields, no incident waves exist. The SHG waves simply emerge from the layer containing the sources $\hat{\boldsymbol{S}}^{(\text{SHG})}(\boldsymbol{r})$. Adjacent to each side of the layer (assumed to be almost infinitely thin), a wave emerges (see Fig. 8.6). Also note that in the oblique case, source components pointing normal to the plane of the Metamaterial can radiate into the far fields.

Consequently, we have to derive different equations to formulate the DDA for arbitrary angles. We first restrict our description to radiation directions in the xz-plane. For a Metamaterial, the radiated waves must be plane waves in the far field. We also only consider these plane waves in the near field. The two SHG waves radiated from the planar Metamaterial into the two half-spaces must have the same x-component of wave vector, K_x (see Fig. 8.6). This component is fixed by linear optics, i.e., by the exciting wave with wave vector $\boldsymbol{k}$ incident from air at the angle α, resulting in $K_x = 2k_x = 2|\boldsymbol{k}| \sin \alpha$.

Then, in contrast to Eqs. (8.23), (8.25), and (8.26), a different spatial Fourier component of the source field $\hat{\boldsymbol{S}}^{(\mathrm{SHG})}(\boldsymbol{r})$ is relevant:

$$\hat{\tilde{\boldsymbol{S}}}_{\alpha}^{(\mathrm{SHG})} = \frac{1}{a_x a_y \Delta z} \int\limits_{\text{one unit cell}} \mathrm{d}^3 r' \, \mathrm{e}^{-\mathrm{i}K_x x} \, \hat{\boldsymbol{S}}^{(\mathrm{SHG})}(\boldsymbol{r}') \,, \tag{8.28}$$

and we now apply the replacement

$$\hat{\boldsymbol{S}}^{(\mathrm{SHG})}(\boldsymbol{r}) \quad \rightarrow \quad \mathrm{e}^{\mathrm{i}K_x x} \, \hat{\tilde{\boldsymbol{S}}}_{\alpha}^{(\mathrm{SHG})} \tag{8.29}$$

within the Metamaterial slab of small thickness Δz. Equations (8.28) and (8.29) basically extract from the Bloch-periodic function $\hat{\boldsymbol{S}}^{(\mathrm{SHG})}(\boldsymbol{r})$ the radiating dipole part while maintaining the lateral wave vector K_x.

For describing the radiated SHG waves, we again start by considering two half-spaces of free space only, i.e., air everywhere except for the thin slab of sources near $z = 0$. After contracting the constant prefactors into

$$C = -\mathrm{i} \frac{\Delta z}{2c_0} \frac{1}{2\omega_0 + \mathrm{i}\gamma_{\mathrm{c}}} \,, \tag{8.30}$$

the electric field of the radiated SHG waves becomes

$$\hat{\boldsymbol{E}}_{\text{far field}}^{(\mathrm{SHG})}(\boldsymbol{r}) =$$
$$C \, \mathrm{e}^{\mathrm{i}\boldsymbol{K}_{\pm} \cdot \boldsymbol{r}} \frac{1}{2n_{\mathrm{air}} \cos \alpha_{\mathrm{air}}} \begin{pmatrix} \cos \alpha_{\mathrm{air}} \left(\hat{\tilde{S}}_{\alpha,x}^{(\mathrm{SHG})} \cos \alpha_{\mathrm{air}} \mp \hat{\tilde{S}}_{\alpha,z}^{(\mathrm{SHG})} \sin \alpha_{\mathrm{air}} \right) \\ \hat{\tilde{S}}_{\alpha,y}^{(\mathrm{SHG})} \\ \mp \sin \alpha_{\mathrm{air}} \left(\mp \hat{\tilde{S}}_{\alpha,z}^{(\mathrm{SHG})} \sin \alpha_{\mathrm{air}} + \hat{\tilde{S}}_{\alpha,x}^{(\mathrm{SHG})} \cos \alpha_{\mathrm{air}} \right) \end{pmatrix} . \tag{8.31}$$

Here, α_{air} is the off-normal angle of the radiation into air (see Fig. 8.6), and $\boldsymbol{K}_{\pm}$ is the SHG wave vector for each half-space of air, i.e., $\boldsymbol{K}_+ = K_{\mathrm{air}} (\sin \alpha_{\mathrm{air}}, 0, \cos \alpha_{\mathrm{air}})^{\mathrm{T}}$ for $z > 0$ and $\boldsymbol{K}_- = K_{\mathrm{air}} (\sin \alpha_{\mathrm{air}}, 0, -\cos \alpha_{\mathrm{air}})^{\mathrm{T}}$ for $z < 0$, where $K_{\mathrm{air}} = 2|\boldsymbol{k}|$. Note in Eq. (8.31) that for the radiation in each direction, only the corresponding transverse components of $\hat{\tilde{\boldsymbol{S}}}_{\alpha}^{(\mathrm{SHG})}$ are relevant, and that the $\hat{\tilde{S}}_{\alpha,z}^{(\mathrm{SHG})}$ component can indeed radiate here.

In the corresponding experiments, we detect a SHG wave which is transmitted through the substrate at varying angles. Hence, we cannot neglect the substrate as for normal radiation (see previous section), but we have to take into account the Fresnel formulas (2.14).

From now on, we will only consider the SHG field in the half space $z < 0$ corresponding to describe the first part of the substrate. The sources reside in a (almost infinitely thin) layer between the substrate and air. It is crucial to note that there can be a difference in the radiation, depending on whether the sources reside just outside the substrate (in air) or just inside the substrate – a question which is nontrivial to answer.

We consider first the case in which the sources are at $z = +0$ just outside the substrate (corresponding to the scenario described by $\varepsilon_{\mathrm{bg}}$). For this case, we can take the radiation according to Eq. (8.31) ("$-$" case) and apply the Fresnel formulas for the air/substrate interface to obtain the radiated wave transmitted to the substrate. Doing this, we obtain

$$\hat{\boldsymbol{E}}_{\mathrm{sub}}^{(\mathrm{SHG})}(\boldsymbol{r}) = C\, e^{i\boldsymbol{K}_{\mathrm{sub}}\cdot\boldsymbol{r}} \left[\begin{pmatrix} 0 \\ 1 \\ 0 \end{pmatrix} \frac{\hat{\tilde{S}}_{\alpha,y}^{(\mathrm{SHG})}}{n_{\mathrm{sub}}\cos\alpha_{\mathrm{sub}} + n_{\mathrm{air}}\cos\alpha_{\mathrm{air}}} + \right.$$
$$\left. \begin{pmatrix} \cos\alpha_{\mathrm{sub}} \\ 0 \\ \sin\alpha_{\mathrm{sub}} \end{pmatrix} \frac{\hat{\tilde{S}}_{\alpha,x}^{(\mathrm{SHG})}\cos\alpha_{\mathrm{air}} + \hat{\tilde{S}}_{\alpha,z}^{(\mathrm{SHG})}\sin\alpha_{\mathrm{air}}}{n_{\mathrm{sub}}\cos\alpha_{\mathrm{air}} + n_{\mathrm{air}}\cos\alpha_{\mathrm{sub}}} \right]. \quad (8.32)$$

Here, $\boldsymbol{K}_{\mathrm{sub}} = n_{\mathrm{sub}}K_{\mathrm{air}}\left(\sin\alpha_{\mathrm{sub}}, 0, -\cos\alpha_{\mathrm{sub}}\right)^{\mathrm{T}}$ and α_{sub} are the wave vector inside the substrate and the off-normal angle of the radiation direction, respectively (see Fig. 8.6). n_{air} and n_{sub} are the refractive indices defined earlier.

The second case in which the sources reside just inside the substrate at $z = -0$ is slightly more complicated. We have to start by the radiation to two half-spaces of glass, that is described by Eq. (8.31) when replacing all occurrences of the subscript "air" by "sub". Then, taking the substrate/air interface into account, interference takes place of the partially reflected wave with $\boldsymbol{K}_+$ and the normally propagating wave with $\boldsymbol{K}_-$. The result is

$$\hat{\boldsymbol{E}}_{\mathrm{sub}}^{(\mathrm{SHG})}(\boldsymbol{r}) = C\, e^{i\boldsymbol{K}_{\mathrm{sub}}\cdot\boldsymbol{r}} \left[\begin{pmatrix} 0 \\ 1 \\ 0 \end{pmatrix} \frac{\hat{\tilde{S}}_{\alpha,y}^{(\mathrm{SHG})}}{n_{\mathrm{sub}}\cos\alpha_{\mathrm{sub}} + n_{\mathrm{air}}\cos\alpha_{\mathrm{air}}} + \right.$$
$$\left. \begin{pmatrix} \cos\alpha_{\mathrm{sub}} \\ 0 \\ \sin\alpha_{\mathrm{sub}} \end{pmatrix} \frac{\hat{\tilde{S}}_{\alpha,x}^{(\mathrm{SHG})}\cos\alpha_{\mathrm{air}} + \hat{\tilde{S}}_{\alpha,z}^{(\mathrm{SHG})}(n_{\mathrm{air}}^2/n_{\mathrm{sub}}^2)\sin\alpha_{\mathrm{air}}}{n_{\mathrm{sub}}\cos\alpha_{\mathrm{air}} + n_{\mathrm{air}}\cos\alpha_{\mathrm{sub}}} \right].$$
$$(8.33)$$

Equation (8.33) is identical to Eq. (8.32) except for the factor $(n_{\mathrm{air}}^2/n_{\mathrm{sub}}^2) = 1/\varepsilon_{\mathrm{sub}}$ applied to $\hat{\tilde{S}}_{\alpha,z}^{(\mathrm{SHG})}$. This means that when taking the sources from just outside the substrate to just inside, we effectively have to divide the normal component of the sources by the substrate permittivity. We will show numerical results for both cases. We note in passing that Eqs. (8.33) and (8.32) are consistent with much longer formulas presented in [138].

In the experiments, the wave is detected after being transmitted also through the back side of the substrate, where the Fresnel formulas have to be applied again, but this part is not critical. We have shown Eqs. (8.32) and (8.33) solely for the purpose to make evident that we have to consider two cases, one with $\hat{\tilde{S}}_{\alpha,z}'^{(\mathrm{SHG})} = \hat{\tilde{S}}_{\alpha,z}^{(\mathrm{SHG})}$ and one with $\hat{\tilde{S}}_{\alpha,z}'^{(\mathrm{SHG})} = \hat{\tilde{S}}_{\alpha,z}^{(\mathrm{SHG})}/\varepsilon_{\mathrm{sub}}$. Knowing this, we can express the SHG intensity transmitted through both surfaces of the

substrate by the intensity radiated according to Eq. (8.31) for air and applying twice the corresponding intensity transmittance factors according to the Fresnel formulas. Hence, the experimentally detectable SHG intensity is proportional to

$$I_{xz} \propto \frac{1}{\cos^2 \alpha_{\text{air}}} \left[\beta_{\text{S}}^2 \left| \hat{\tilde{S}}_{\alpha,y}^{(\text{SHG})} \right|^2 + \beta_{\text{P}}^2 \left| \hat{\tilde{S}}_{\alpha,x}^{(\text{SHG})} \cos \alpha_{\text{air}} + \hat{\tilde{S}}'^{(\text{SHG})}_{\alpha,z} \sin \alpha_{\text{air}} \right|^2 \right] \qquad (8.34)$$

for oblique radiation directions in the xz-plane and

$$I_{yz} \propto \frac{1}{\cos^2 \alpha_{\text{air}}} \left[\beta_{\text{S}}^2 \left| \hat{\tilde{S}}_{\alpha,x}^{(\text{SHG})} \right|^2 + \beta_{\text{P}}^2 \left| \hat{\tilde{S}}_{\alpha,y}^{(\text{SHG})} \cos \alpha_{\text{air}} + \hat{\tilde{S}}'^{(\text{SHG})}_{\alpha,z} \sin \alpha_{\text{air}} \right|^2 \right] \qquad (8.35)$$

for oblique radiation directions in the yz-plane. Here, the intensity transmittance factors β_{S} and β_{P} following from the Fresnel formulas (2.14) are

$$\beta_{\text{S}} = 1 - \frac{\sin^2(\alpha_{\text{air}} - \alpha_{\text{sub}})}{\sin^2(\alpha_{\text{air}} + \alpha_{\text{sub}})}, \qquad (8.36)$$

$$\beta_{\text{P}} = 1 - \frac{\tan^2(\alpha_{\text{air}} - \alpha_{\text{sub}})}{\tan^2(\alpha_{\text{air}} + \alpha_{\text{sub}})}. \qquad (8.37)$$

For radiation directions in the yz-plane, the relevant Fourier component of the sources must be determined according to Eq. (8.28) with the replacement $K_x x \to K_y y$.

In summary, we have a method of obtaining the relative SHG intensity for the Driven-Dipole Approximation for oblique-incidence excitation and SHG radiation for various angles. The description is valid for a fixed excitation frequency and contains an ambiguity concerning the normal component of the sources.

We note that we have only considered the two cases in which the sources reside in one of the two adjacent materials. One can think of a general case in which the sources reside in a layer with its own, independent permittivity, however, this scenario leads to more ambiguities, e.g., it alters also the influence of xy-components of the sources. The even more general case of an independent non-isotropic layer permittivity (a tensor) will hardly give physical insights in the comparison with experiments.

We additionally note that all above formulas describe plane waves with infinite extent. In the experiments, no infinite waves are used, but rather light beams with Gaussian lateral profiles, of which the widths (in linear and nonlinear optics) are much larger than corresponding wavelengths, thus, diffraction because of finite beam width can be neglected near the focus. Hence, no corrections are needed for relative intensities, since the SHG beam width (behind the substrate) is independent of the angle of incidence, and all "plane waves" in air are simply multiplied by the same (but tilted) profile envelope.

8.4 Second-Harmonic Generation based on the magnetic part of the Lorentz force

Here, we present numerical results on the nonlinear optics of Metamaterials, described by our theory of section 8.2 and numerically computed using FEMLAB (see chapter 4). Since we

have no numerical tools to obtain the self-consistent SHG fields, we use the Driven-Dipole Approximation (see previous section) for Second-Harmonic Generation. (Third-Harmonic Generation cannot be computed with these methods.)

As discussed in section 8.2, the theory predicts SHG owing to three source terms. Here, we present results for the $j \times B$-term, i.e., the magnetic part of the Lorentz force. This term seems most interesting in the context of magnetic Metamaterials, e.g., because of strong local magnetic fields of particular direction (cf. section 8.1).

As to the other source terms, we have performed simulations based on the ρE-term, but have not achieved convergence within our careful studies.[1] Preliminary (unstable) results have indicated that the ρE-term leads to SHG intensities smaller than for the $j \times B$-term, but we will not discuss this aspect nor this term further. For the jj-term, we have shown in section 8.3.2 that it does not contribute at all to SHG for normal incidence. Additionally, FEMLAB encounters the same principal problems for the surface terms of the jj-term as for the ρE-term. Thus, our results presented here are based exclusively on the $j \times B$-term. A more systematic investigation is left to others possessing extended numerical and/or analytical possibilities.

We compute relative nonlinear intensities for the SRRs of which the linear-optical properties have been discussed in section 8.1. Among these are resonances with magnetic dipole moments and cases without. As in the experiments, we always use an excitation at the fixed frequency $\omega_0 = 2\pi c_0/(1.5\,\mu\text{m}) = 2\pi \times 200\,\text{THz}$, such that frequency dependencies do not need to be discussed in following comparisons.

8.4.1 Radiation into normal direction

In Figs. 8.3 and 8.4, we have shown snapshots of the electron velocity field and the magnetic field, respectively, for the four cases of interest. Now we discuss the $j \times B$-term, and show corresponding field distributions of this source term in Fig. 8.7. There, only the tangential components (in the plane of the Metamaterial) leading to SHG are depicted, on individual scales for each case. The fields which are radiated due to the source term $\hat{\boldsymbol{v}}^{(1)}(\boldsymbol{r}) \times \hat{\boldsymbol{B}}^{(1)}(\boldsymbol{r})$ from different locations $\boldsymbol{r}$, interfere in the far field and partially cancel each other, when two opposing contributions are present. This applies for the fields in the lower row in Fig. 8.7, i.e., for the nonresonant case and the vertical electric resonance. For the other two cases, associated with a magnetic dipole moment, the horizontal components sum to zero (as expected from our symmetry considerations of section 8.2.1), while a vertical component remains.

We note that in all cases, a strong longitudinal force component (not shown) appears. However, this force leads to a longitudinal electron oscillation which cannot radiate into the longitudinal, i.e., forward or backward direction. For our Metamaterials with a magnetic dipole moment, the longitudinal component of the local magnetic field, however, gives rise to a transverse component of the magnetic part of the Lorentz force, of which the vertical component leads to radiation into the forward and backward directions.

In the Driven-Dipole Approximation, the source fields of Fig. 8.7 are averaged over the

---

[1] see chapter 4 on errors of the divergence of the electric field on surfaces and interfaces
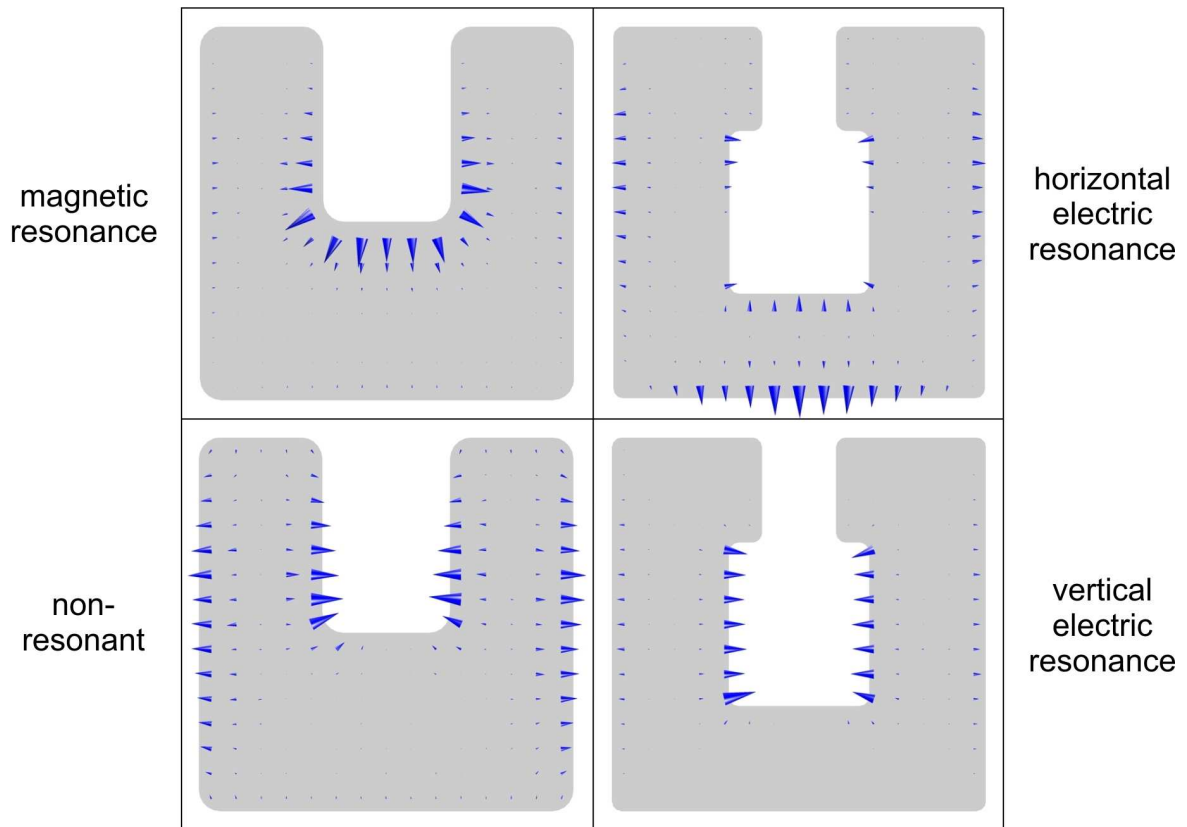
Figure 8.7: Snapshots of the magnetic component of the Lorentz force field (only the tangential SHG part) acting on metal electrons, $(-e)\mathrm{Re}[\hat{\boldsymbol{v}}^{(1)}(\boldsymbol{r})\times\hat{\boldsymbol{B}}^{(1)}(\boldsymbol{r})]_{xy}$. Compare Figs. 8.3 and 8.4. Each of the field distributions is shown on its own scale of field strength.
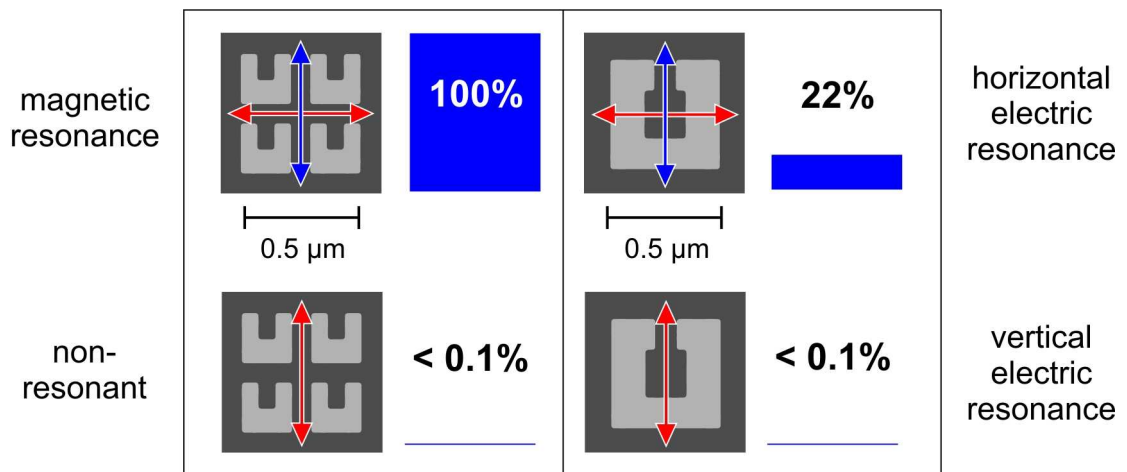

Figure 8.8: Calculated SHG for the four cases under normal-incidence excitation, with a linear-optical polarization indicated by the red arrows. The SHG source is the magnetic component of the Lorentz force on metal electrons in the SRRs. The blue bars highlight the corresponding SHG intensities, normalized to 100 % for the highest SHG intensity obtained from the magnetic resonance. The polarization of the SHG wave is indicated by the blue arrows, for the cases with intensities far above the numerical noise. Compare to the corresponding experiments (Fig. 9.3).

corresponding unit cells. The relative SHG intensities calculated this way for the four cases are depicted in Fig. 8.8, normalized to $100\,\%$ for the strongest intensity, which is obtained for the magnetic resonance associated with a strong magnetic dipole moment. The second strongest result is found for the horizontal electric resonance which also is connected with a smaller, but finite magnetic dipole moment. The other two cases yield much weaker intensities. The blue arrows in Fig. 8.8 depict the vertical polarization of the SHG wave for the strong-intensity cases. The polarization corresponds to the remaining vertical component after averaging the field distributions.

8.4.2   Radiation into arbitrary angles

For the three resonant cases, the linear-optical transmittance spectra for oblique angles of incidence have been shown in Fig. 8.5. Applying the Driven-Dipole Approximation for arbitrary angles to these cases yields the angle-resolved relative SHG intensities shown in Fig. 8.9 for S- and P-polarization. Again, the intensities are normalized to $100\,\%$ for the magnetic resonance at normal incidence. Note the different signal scales (bold numbers). The blue and green curves depict the cases (i) $\hat{\bar{S}}'^{(\mathrm{SHG})}_{\alpha,z} = \hat{\bar{S}}^{(\mathrm{SHG})}_{\alpha,z}$ and (ii) $\hat{\bar{S}}'^{(\mathrm{SHG})}_{\alpha,z} = \hat{\bar{S}}^{(\mathrm{SHG})}_{\alpha,z}/\varepsilon_{\mathrm{sub}}$ which result from the ambiguity of the DDA for arbitrary angles as discussed in section 8.3.3. Obviously, the two cases (i) and (ii) differ strongly for all configurations in Fig. 8.9, owing to a strong z-component of the source term. Also, a considerable angle-dependence of the SHG strength can be observed. Additionally, for S-polarization and case (i), the magnetic resonance in Fig. 8.9(a) and the horizontal electric resonance in Fig. 8.9(b), which are both connected with magnetic dipole moments, exhibit an asymmetric SHG intensity behavior with respect to opposite angles of incidence. This asymmetry arises because of the normal component of the magnetic field (confer discussion of oblique incidence in section 8.1).
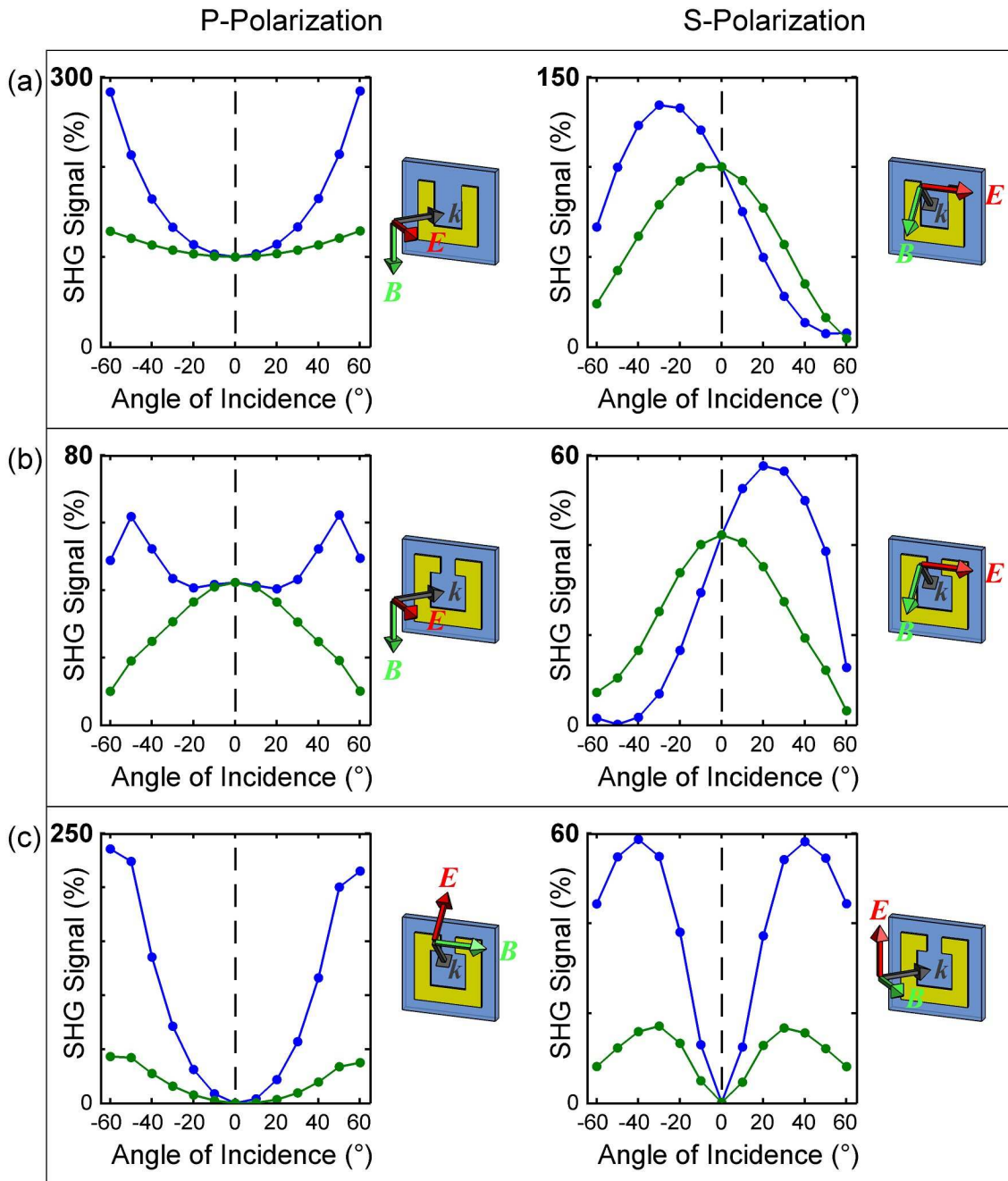
Figure 8.9: Calculated SHG intensities resulting from oblique-incidence excitation, for the cases with a resonance near $1.5\,\mu m$ wavelength (cf. transmittance spectra in Fig. 8.5). The SHG source is again the magnetic component of the Lorentz force on metal electrons in the SRRs. The SHG intensity radiated into the forward direction, transmitted through both surfaces of the substrate, is shown for different angles of incidence. Intensities are normalized to $100\,\%$ for the magnetic resonance (a) at normal incidence ($0°$). Note the different signal scales (bold numbers). The blue (green) curves depict the SHG intensity in the case in which the nonlinear sources are located at the air/substrate interface just outside (inside) the substrate. Compare to the corresponding experiments (Fig. 9.11).

Chapter 9

Nonlinear optics of planar Metamaterials: Experiments

The linear optics of Metamaterials has been investigated experimentally since a few years ago (cf. section 2.5). While also "enhanced and novel nonlinear-optical properties" [64] have already been predicted theoretically in 1999, the field of corresponding nonlinear-optical experiments is still at its beginning. Our experiments are the first systematic study of the nonlinear optics of Metamaterials. In this chapter, we present corresponding results on Second- (SHG) and Third-Harmonic Generation (THG) from planar Metamaterials. In addition, we compare our findings to our theoretical results of chapter 8.

In section 9.1, we describe the details of our principal Metamaterial samples which consist of planar arrays of Split-Ring Resonators (SRRs). For normal-incidence experiments (section 9.2), we present the linear-optical properties and the SHG and THG results of these samples, and additionally for several control samples characterized along the way. We find a positive correlation of strong nonlinear signals and strong magnetic dipole moments of the samples. For oblique-incidence experiments (section 9.3), we discuss the linear-optical and SHG results for the principal samples.

9.1   Description of principal samples

Photonic Metamaterials have been defined in section 2.5 as artificial (usually periodic) optical materials which do not exhibit diffraction and consist of responsive building blocks ("atoms"). In particular, Split-Ring Resonators (cf. section 2.5.1) and their three fundamental resonances have been introduced there [see Fig. 2.5(d)-(f)]. Our two principal Metamaterial samples META-*A* and META-*B* (see Fig. 9.1) are planar arrays of gold SRRs arranged in a square lattice. They are located on top of a 1-mm-thick quartz substrate with a 5-nm-thick layer of ITO and are fabricated by the methods described in section 3.1. The SRRs of sample META-*A* (sample META-*B*) have a side length of about $220\,\text{nm}$ ($480\,\text{nm}$) and lattice constants $a_x=a_y=305\,\text{nm}$ ($630\,\text{nm}$). The gold thickness of $25\,\text{nm}$ and the footprint of $(100\mu\text{m})^2$ are equal for all samples presented in this chapter. Hence, sample META-*A* and META-*B* directly correspond to the examples META-*A* and META-*B* of the theory chapter 8.
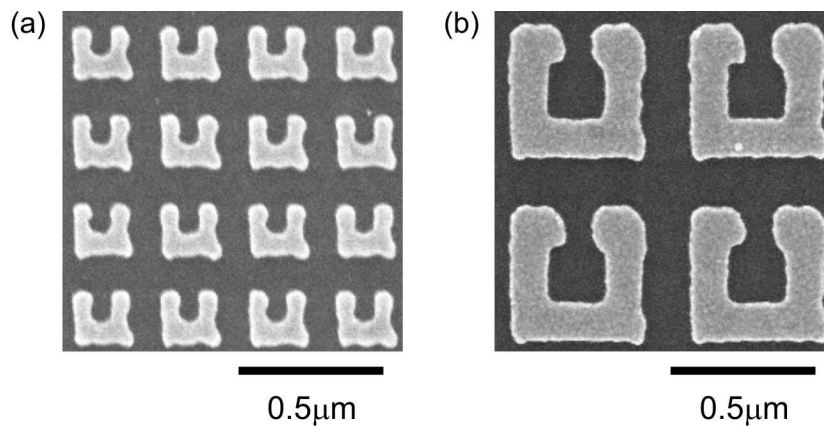
Figure 9.1: Scanning electron micrographs of samples (a) META-*A* and (b) META-*B*. Each sample consists of gold Split-Ring Resonators (thickness 25 nm) arranged in a 2D square lattice which covers a total area of $(100\,\mu m)^2$. The SRRs have been designed such that they exhibit a resonance at the aim wavelength of $1.5\,\mu m$ in linear optics (see text).

For frequencies far below the metal plasma frequency, the SRR resonance wavelengths are simply proportional to the SRR size [85]. Using this relation, the geometrical parameters of our principal samples are tailored such that the magnetic resonance of sample META-*A* and the horizontal and vertical electric resonances of META-*B* are tuned to an aim wavelength of $1.5\,\mu m$. We employ this "lithographic tuning" in order to use the laser setup of section 3.3.2 exclusively at this aim wavelength, for resonant excitation of the samples. If, in contrast, we tuned the wavelength of the laser (the OPO, cf. section 3.3.2) to excite different resonances of the same sample at different wavelengths (which would hardly be possible for the presented samples), the gold optical nonlinearities would likely change considerably, and even interband transitions in gold would come into play at short wavelengths (cf. section 2.3). We avoid these systematic but inestimable changes by applying the "lithographic tuning." Additionally, we fabricate all samples, which we want to compare later, in one fabrication run on the same glass substrate. These aspects ensure that it is really meaningful to compare the nonlinear-optical signal strengths of different samples.

9.2   Experiments with normal incidence

We start our description of experiments with the configuration in which the samples are excited by light at normal incidence. Here, only few parameters of the optical setups have to be adjusted, making results highly reproducible.

9.2.1   Linear-optical properties

Figure 9.2 shows transmittance spectra of samples META-*A* and META-*B*, measured with the optical setup described in section 3.2.1. The various observed transmittance dips correspond to the resonances excited by the electric field of the incident light, causing resonantly enhanced local fields. By counting the resonances from the long-wavelength side, and by
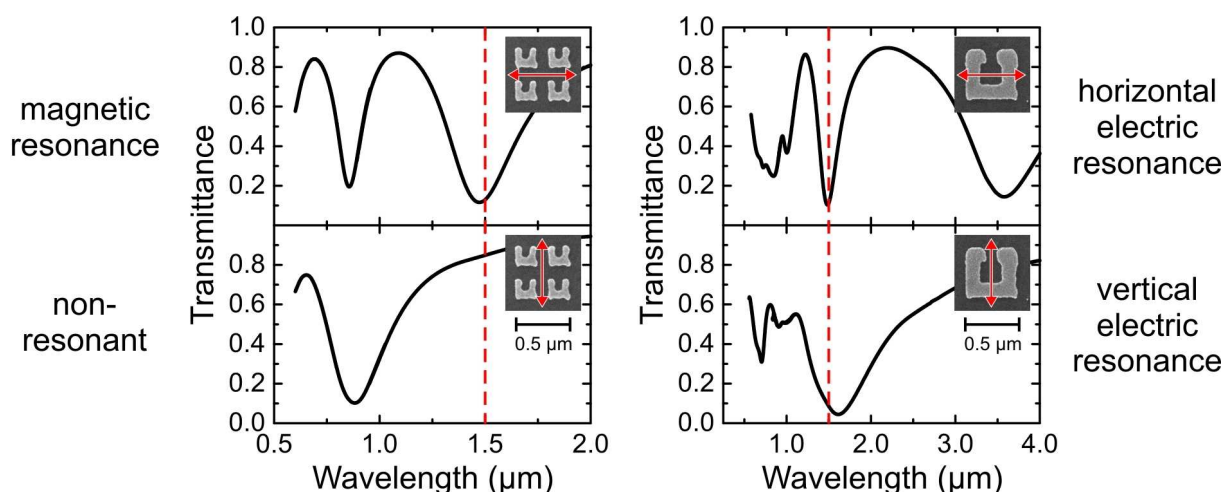
Figure 9.2: Measured linear-optical transmittance spectra of samples META-*A* (left column) and META-*B* (right column) located on the same substrate. Spectra are shown for horizontal (top row) and vertical (bottom row) incident polarization and normal incidence. The insets repeat corresponding electron micrographs and the incident polarization (red arrows). Because of the character of the resonances (not) appearing at the laser (OPO) wavelength of $1.5\,\mu m$ (dashed red line), we call the four cases, as denoted, the magnetic resonance, the nonresonant case, the horizontal electric resonance, and the vertical electric resonance, respectively. Compare to the corresponding calculations (Fig. 8.2).

comparing the transmittance spectra for horizontal and vertical incident polarization, we are able to relate the dips at the aim wavelength of $1.5\,\mu m$ to the magnetic, horizontal electric, and vertical electric resonances, respectively, as labelled next to the spectra. One case (sample META-*A* and vertical incident polarization) does not exhibit a dip at this wavelength and is consequently labelled nonresonant. Our measured spectra (Fig. 9.2) are in excellent agreement with corresponding calculations (Fig. 8.2), further supporting our interpretation of the resonances.

9.2.2 Second-Harmonic Generation for different resonances

Since the linear-optical electromagnetic fields of these resonances differ in character, one also expects a differing behavior in nonlinear optics. Here, we present results for Second-Harmonic Generation. The setup for measuring SHG and THG at the fixed excitation wavelength of $1.5\,\mu m$ has been described in section 3.3.2. Figure 9.3 shows corresponding SHG signals measured for samples META-*A* and META-*B* and horizontal and vertical incident polarization (i.e., the four cases of which the linear-optical properties are depicted in Fig. 9.2). While the linear-optical response of different resonances is similarly strong, we observe that the SHG signal drastically depends on which resonance is excited. It is evident from Fig. 9.3 that the magnetic resonance (associated with a large magnetic-dipole moment) clearly leads to the strongest SHG signal. We normalize this signal to $100\,\%$ and describe all other SHG signals correspondingly (the noise level corresponds to about $0.3\,\%$). This normalization must not be confused with the absolute conversion efficiencies (see below).

In Fig. 9.3, the second strongest SHG signal strength of only $4\,\%$ is obtained from the
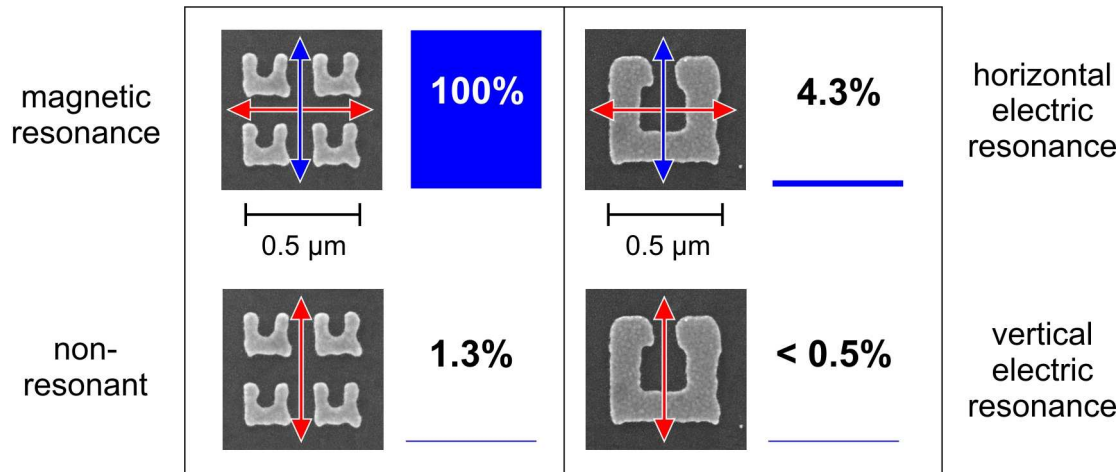
Figure 9.3: Measured Second-Harmonic signal strength (represented by the blue bars) for the four cases (cp. Fig. 9.2) under normal-incidence excitation, with a linear-optical polarization indicated by the red arrows in the electron micrographs. The SHG signal strengths are normalized to 100% for the strongest SHG signal obtained from the magnetic resonance. The detection noise is about 0.2%. The approximate polarization of the SHG emission is indicated by the blue arrows, for the cases with appreciable signal strengths [see also Fig. 9.4(b)]. Compare to the corresponding calculations (Fig. 8.8).

horizontal electric resonance. Interestingly, this resonance is also associated with a small magnetic-dipole moment (see section 2.5.1). The SHG signal is much lower than for the magnetic resonance despite the fact that their oscillator strengths in the linear spectra are comparable. For the vertical electric resonance, we find a small SHG signal just above the noise level. For completeness, Fig. 9.3 also shows the nonresonant case for sample META-*A* and vertical incident polarization.

As expected from Eq. (2.26), the SHG signal (e.g., from the magnetic resonance) closely scales with the square of the incident power [see Fig. 9.4(a)]. The polarization of the SHG emission from the magnetic resonance is nearly vertical [see Fig. 9.4(b)]. The small tilt angle (about $15°$) of the SHG polarization with respect to the vertical direction is due to deviations from perfect mirror symmetry of the SRRs [see electron micrographs in Fig. 9.1(a)], as confirmed by the experiments described in the next section. For the horizontal electric resonance, the SHG emission is again polarized nearly vertically.

For the SHG signal obtained from the magnetic resonance, we roughly estimate an absolute conversion efficiency of 2×10^{-6}, taking into account the measured signal, the specified photomultiplier quantum efficiency, a correction for all optical components in the optical pathway, and a typical average power of $50\,\text{mW}$ (see section 3.3.2). A corresponding 25-nm-thin film of a standard nonlinear-optical material would deliver a yet much smaller SHG signal. For example, for potassium dideuterium phosphate (KDP) with $\chi^{(2)}=1.0\times10^{-12}$ m/V [4], we estimate a SHG conversion efficiency on the order of 10^{-11} under these conditions. From a closed gold film of the same thickness on the identical glass substrate we find no SHG (as expected from symmetry). For the gold film, also no measurable SHG signal is found for oblique incidence in P-polarization for angles up to $60°$ with respect to the surface normal. For the latter case, symmetry would allow for SHG.
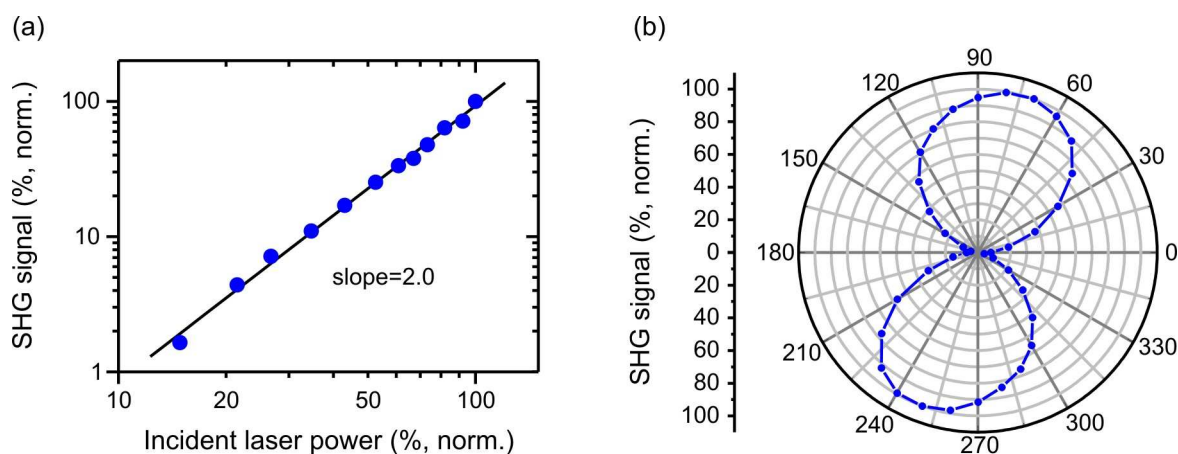
Figure 9.4: (a) Normalized SHG signal strength versus normalized incident laser power on a log-log scale (for the magnetic resonance in Fig. 9.3). The straight line has a slope of two, as expected for SHG. (b) Measured polarization of the SHG emission from the magnetic resonance, represented in a polar diagram which is oriented as the electron micrographs in Fig. 9.3.

Thus, much larger SHG signals are detected from our Metamaterials when magnetic-dipole resonances are excited, as compared with purely electric-dipole resonances. These experiments are consistent with our calculations (see Fig. 8.8) based on the magnetic component of the Lorentz force exerted on metal electrons. However, these experiments are no definite proof that our theory describes the dominating contribution. Hence, further experimental data (e.g., angle-resolved investigations, see section 9.3.2) are required for the comparison with theory.

9.2.3 Second-Harmonic Generation: Symmetry investigations

From the selection rules of SHG [32] and our symmetry considerations of section 8.2.1, the SHG emission of our Metamaterials based on (ideally mirror-symmetric) SRRs should be strictly vertical. Consequently, the reason of the polarization tilt angle [see Fig. 9.4(b)] of the SHG radiation emitted by the magnetic-resonance SRRs was a persisting puzzle for some time. Here, we present further experiments to clarify the origin of this tilt angle.

In Fig. 9.5, we show data for three additional Metamaterial samples, again located on one substrate. These samples consist of SRRs which are fabricated such that they contain designed asymmetries (see the top-row electron micrographs in Fig. 9.5): In (a), the lower-left sides of the SRRs are thicker than on their lower right, in (b), the SRRs are highly symmetric, and in (c), the lower-right sides of the SRRs are systematically thicker. The SHG polarizations (see second row) for parts (a) and (c) are tilted to opposite sides from the vertical direction, and the polarization of part (b) is between those of (a) and (c) and is closest to the vertical direction. Thus, we can expect an exactly vertical SHG polarization for exactly symmetric SRRs. However, it is obvious that the SHG polarization tilt angle delicately depends on details of the SRR geometry.

For completeness, the bottom row of Fig. 9.5 depicts the corresponding linear transmittance spectra of the samples, confirming that these are equally resonant to the excitation at
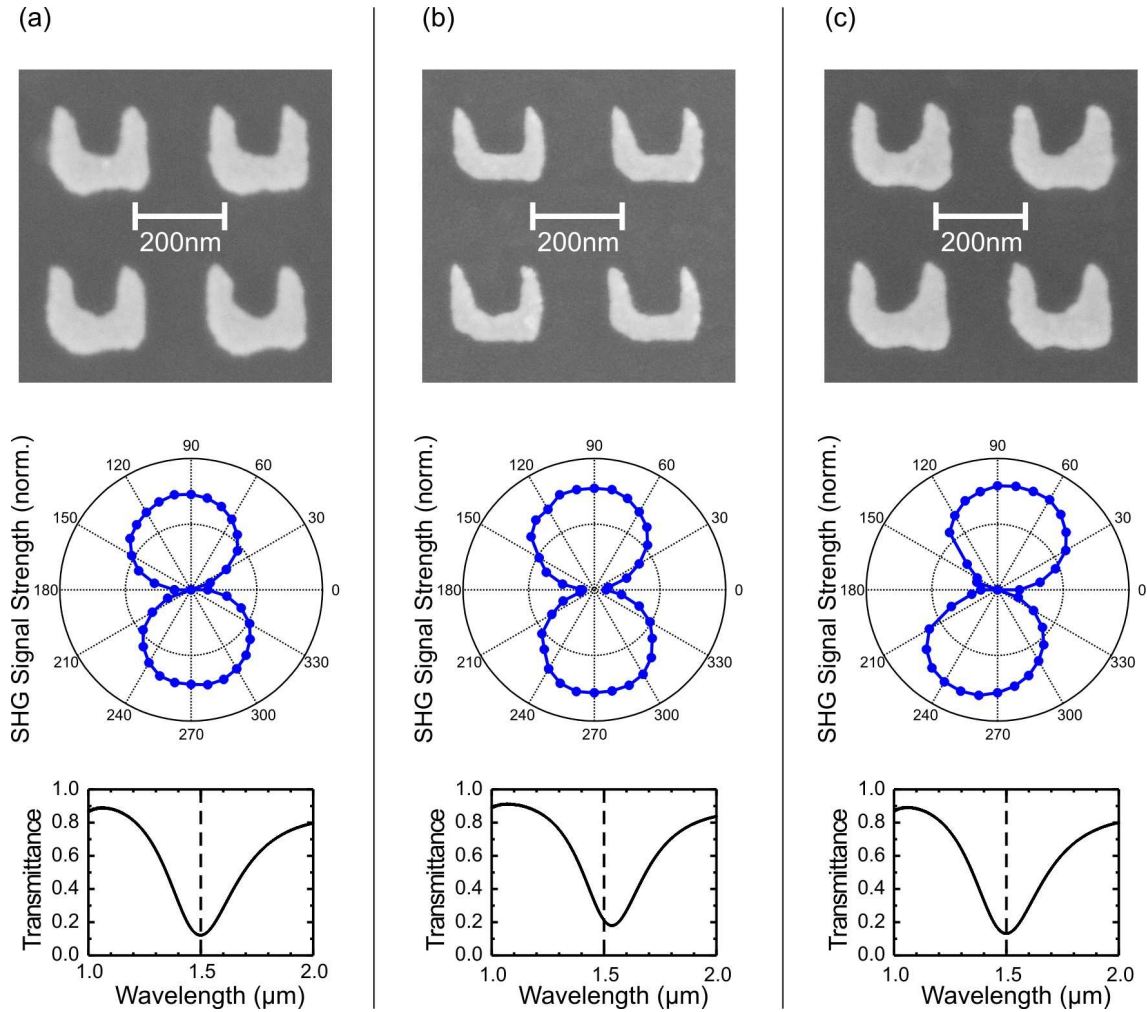
Figure 9.5: Depencence of the SHG polarization tilt [cp. Fig. 9.4(b)] on details of the Split-Ring Resonator geometry. The three scanning electron micrographs in the top row show arrays of SRRs (a) of which the lower-left sides are systematically thicker, (b) which are highly symmetric, and (c) of which the lower-right sides are systematically thicker. The middle row shows the polarization of the SHG emission from the corresponding magnetic resonances, in analogy to Fig. 9.4(b). The linear transmittance spectra in the bottom row confirm that all these magnetic resonances are equally resonant to the excitation at 1.5 μm wavelength.
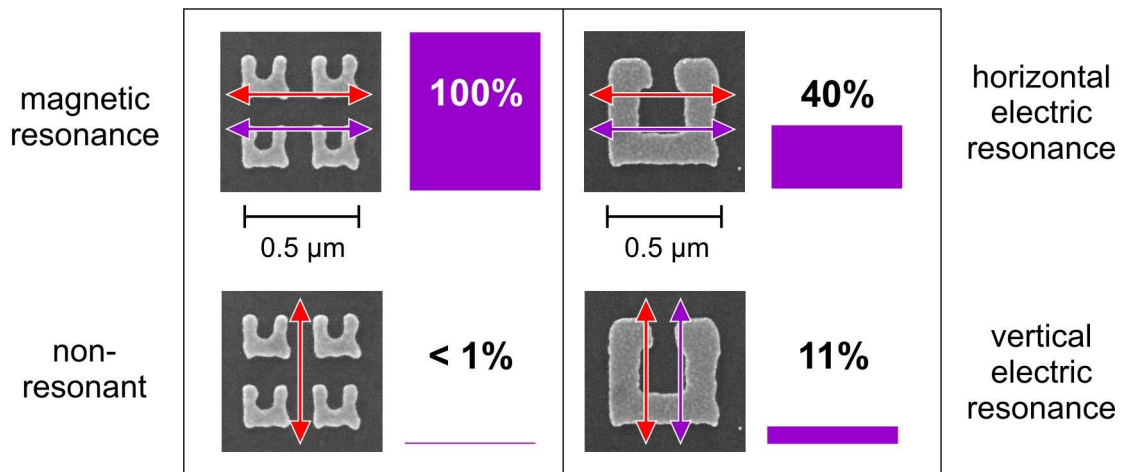
Figure 9.6: Measured Third-Harmonic signal strength (represented by the purple bars) for the four cases (cf. Figs. 9.2 and 9.3) under normal-incidence excitation, with a linear-optical polarization indicated by the red arrows in the electron micrographs. The THG signal strengths are normalized to 100 % for the strongest THG signal obtained from the magnetic resonance. The detection noise is about 0.4 %. The approximate polarization of the THG emission is indicated by the purple arrows, for the cases with appreciable signal strengths.

$1.5 \, \mu m$ wavelength.

9.2.4 Third-Harmonic Generation

In analogy to the SHG experiments described in section 9.2.2, we also perform THG investigations. Corresponding THG signal strengths are summarized in Fig. 9.6 for the four cases related to our principal samples. Evidently, the magnetic resonance also leads to the strongest THG signals. We normalize this THG signal strength to 100 % and relate other THG signals to it (the noise level for THG then corresponds to about 0.4 %). We confirm that the THG signal actually scales with the third power of the incident laser intensity (see Fig. 9.7). For the THG signal obtained from the magnetic resonance and for the conditions described in section 9.2.2, we estimate an absolute conversion efficiency of 3×10^{-7}.

In Fig. 9.6, the second strongest THG signal strength of 40 % is obtained for the horizontal electric resonance. For the vertical electric resonance (for which we observe no significant SHG), a THG signal strength of 11 % is obtained. From the nonresonant case, as well as from a closed gold film of the same thickness on the identical glass substrate, we find no transmitted THG signal. Thus, THG is favored by the cases of resonant character and, among these, by resonances associated with magnetic dipole moments.

9.2.5 Control experiments

This section is devoted to shed more light onto the remaining question about the reasons for the enhancement of SHG and THG observed for particular Metamaterials.

We first discuss a sample (see Fig. 9.8) which is similar to sample META-*A*, but its corresponding magnetic resonance of the SRRs is effectively detuned with respect to sample
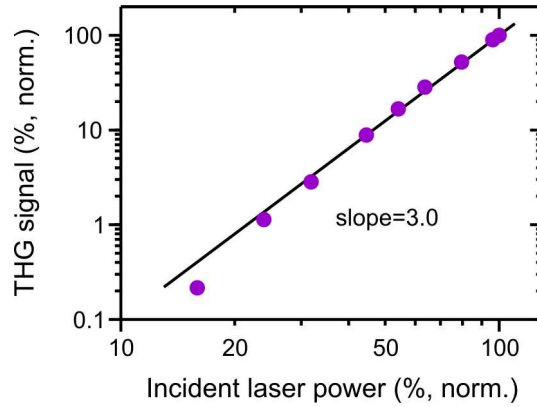
Figure 9.7: Normalized THG signal strength versus normalized incident laser power on a log-log scale. The straight line has a slope of three, as expected for THG.
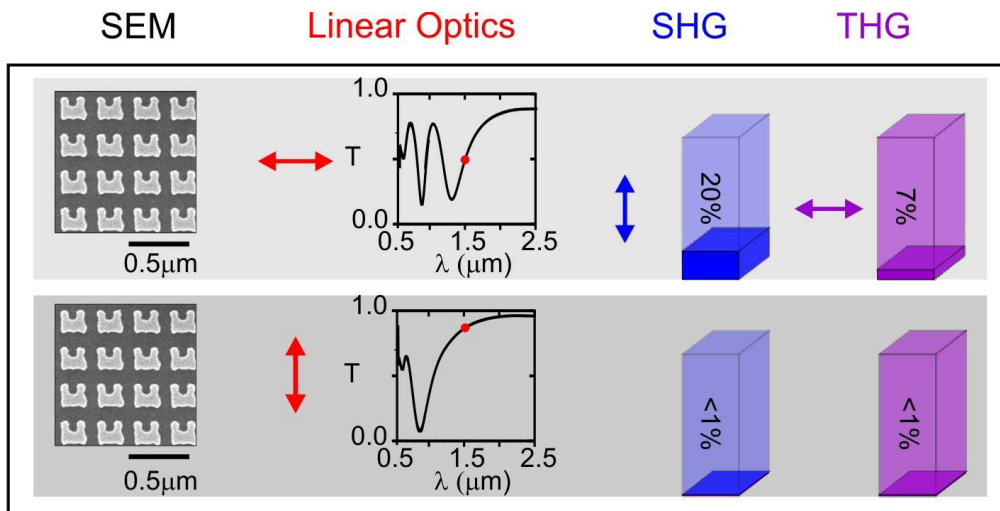
Figure 9.8: Nonlinear response of the detuned SRR control sample, for horizontal (top row) and vertical (bottom row) incident linear polarization. The different columns (from left to right) show the electron micrograph, the measured linear transmittance spectra, the measured SHG signal strength for excitation centered at $1.5\,\mu\text{m}$ wavelength, and the corresponding THG signal strength. The arrows indicate the incident linear polarization (red), the polarization of the SHG emission (blue), and that of the THG emission (purple), if sufficiently large. The nonlinear signals are again normalized to those of the magnetic resonance shown in Figs. 9.3 and 9.6.

META-*A* by $0.25\,\mu$m in wavelength. This sample is also located on the same substrate as the principal samples and compared correspondingly. It is clear from Fig. 9.8 that the detuning leads to a decrease of the SHG signal from $100\,\%$ to $20\,\%$ for excitation with horizontal incident polarization. Correspondingly, the THG signal decreases from $100\,\%$ to $7\,\%$. This comparison shows that the nonlinear signals are resonantly enhanced as expected. Again, no significant SHG and THG signals are found for vertical incident polarization.

Is the observed enhancement of SHG and THG related to the magnetic-dipole character of particular resonances? To address this question, we have fabricated an additional set of samples (again, all fabricated in one run on one substrate), the results of which are summarized in Fig. 9.9. Here, we compare excitation of an array of SRRs closely similar to sample META-*A* (see Figs. 9.1, 9.2, 9.3, and 9.6) with two other structures. One control structure [see Fig. 9.9(b)] consists of "T"-shaped structures without centrosymmetry, in principle allowing for SHG. Nevertheless, the measured SHG signal is within the noise, even though a resonance is excited. The second control sample [see Fig. 9.9(c)] is an array of straight cut wires, which can be viewed as stretched-out versions of the SRRs in (a). From centrosymmetry, no SHG is expected, and indeed no significant SHG is found. This observation indicates that the measured nonlinear signals from our high-quality samples are not dominated by extrinsic effects (see, e.g., our discussion in section 3.1.3). Clearly, both the "T"-structures and the cut wires exhibit zero magnetic-dipole moment. The combination of these observations suggests that the measured large SHG signals from particular resonances of the SRRs are connected to the magnetic-dipole character of these resonances. The THG signals from these control samples are also shown in Fig. 9.9 for completeness.

9.3 Angle-resolved experiments

While our investigations with normally incident light already show many fundamental aspects of nonlinear Metamaterials, corresponding optical experiments with samples illuminated under oblique incidence often provide additional information depending on the underlying physical processes, and thus deliver more input for a comparison with theory.

Here, we restrict our studies to the three resonant cases of the principal samples META-*A* and META-*B* and omit the nonresonant case (cf. Fig. 9.2). We continue to call these three cases the magnetic, horizontal electric, and vertical electric resonance, respectively (although the resonant character may only be present for normal incidence).

Also, it is clear that positive and negative angles α with respect to the surface normal are not always necessarily equivalent. This follows on one hand from our theoretical consideration of section 8.1 concerning the change of sign of the normal component of the magnetic field in S-polarization. On the other hand, positive and negative angles α can lead to different experimental results simply because of a low symmetry of the SRRs. Thus, we perform all measurements for both positive and negative angles.
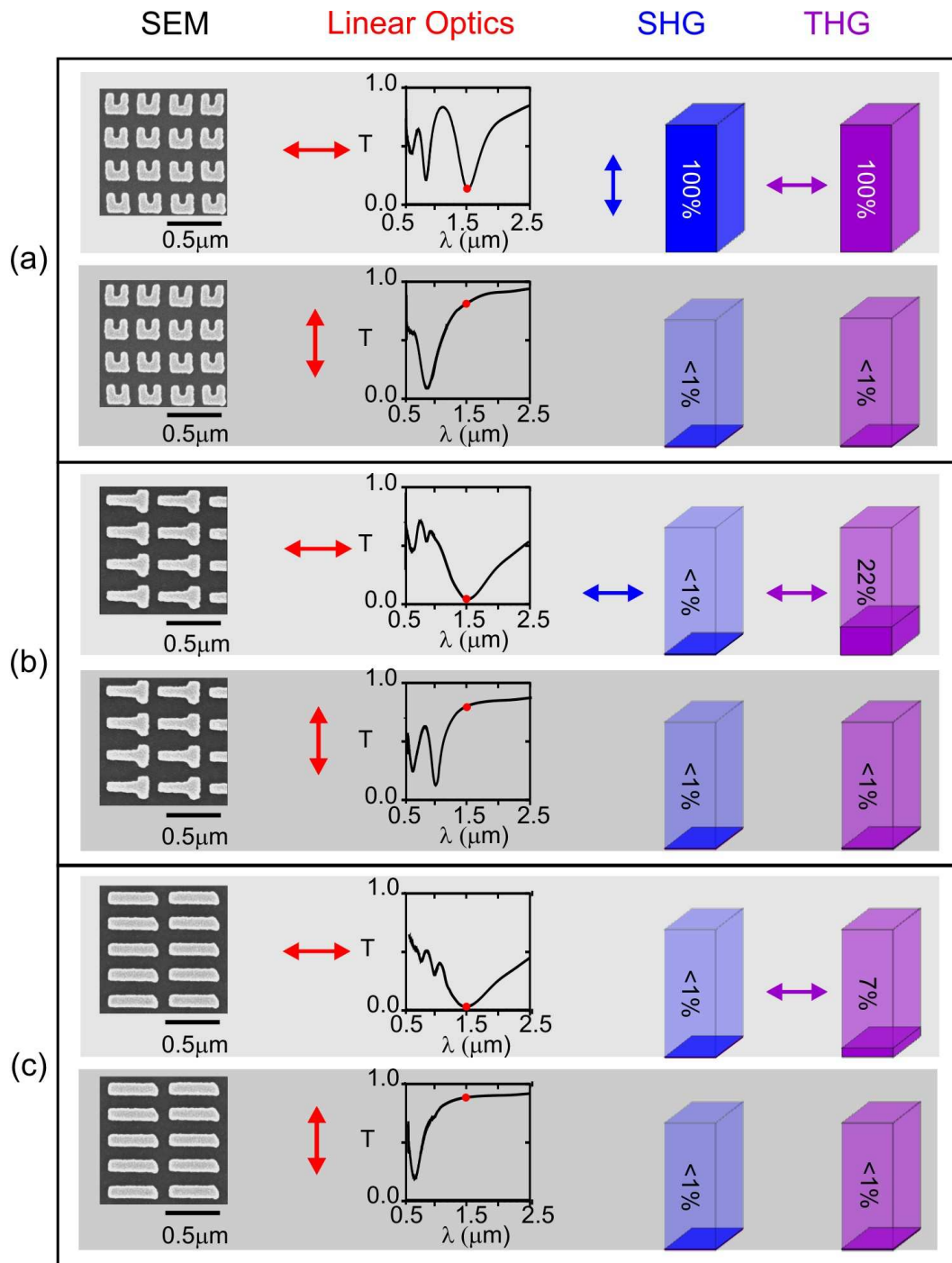
Figure 9.9: Experiments on additional control samples, for a Metamaterial composed of (a) Split-Ring Resonators closely similar (but not identical) to sample META-*A* (see Figs. 9.1, 9.2, 9.3, and 9.6), (b) "T"-shaped structures, and (c) single cut wires. The representation for each sample is as in Fig. 9.8, the nonlinear signals presented here are normalized to the SRRs in (a), top row, here.
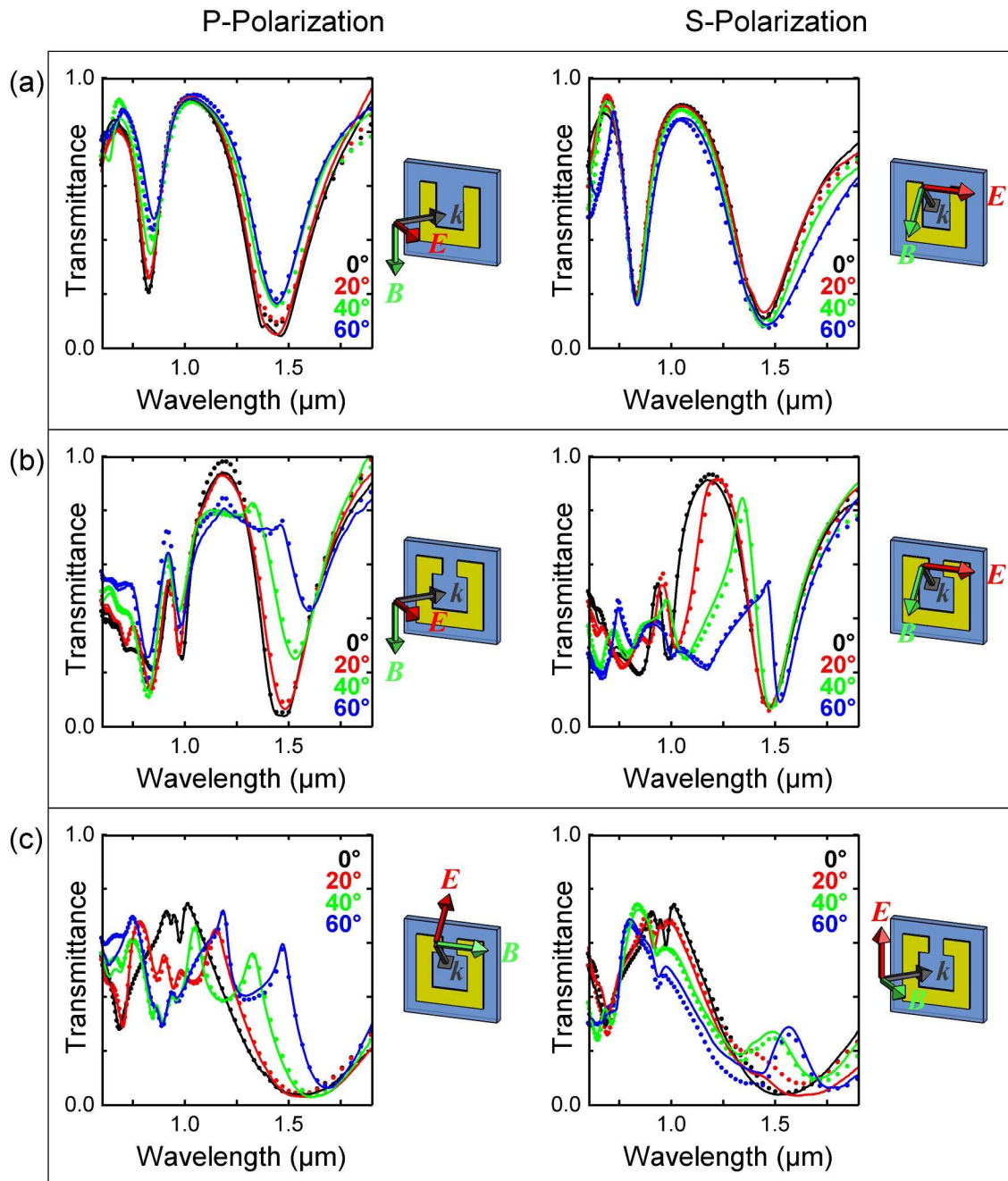
Figure 9.10: Measured linear-optical transmittance spectra for oblique incidence, for the cases with a resonance near 1.5 μm wavelength: (a) magnetic resonance (sample META-*A* and horizontal polarization), (b) horizontal electric resonance (sample META-*B* and horizontal polarization), (c) vertical electric resonance (sample META-*B* and vertical polarization). The left column is for P-polarization, the right column for S-polarization. Transmittance spectra for positive angles (solid curves) and negative angles (dots) are shown, the angle of incidence with respect to the surface normal is indicated by the color. The schemes adjacent to the spectra show the configuration of the incident fields for positive angles of incidence. The difference between the 0°-curves here and the corresponding normal-incidence measurements of Fig. 9.2 is explained in the text. Compare to the corresponding calculations (Fig. 8.5).

9.3.1   Linear-optical properties

The transmittance spectra of the three cases are summarized in Fig. 9.10. The geometries and field directions are illustrated by the nearby schemes. These spectra are measured with the first setup described in section 3.2.2, allowing for oblique-incidence spectroscopy at an opening angle of the incident light of about $5°$ (whereas the normal-incidence transmittance spectra in Figs. 9.2, 9.5, 9.8, and 9.9 are recorded with the setup of section 3.2.1 with a numerical aperture of 0.5, yielding broader spectral features). The spectra are normalized with respect to the bare substrate for the same angle of incidence. The underlying physics has been discussed in section 8.1 and [89]. Importantly, the linear-optical transmittance spectra (Fig. 9.10) show no significant differences between positive and negative angles, respectively.

9.3.2   Angle-resolved Second-Harmonic Generation

We now discuss the SHG signals obtained for the three resonances excited under oblique incidence (using the same setup as for nonlinear normal-incidence experiments). Clearly, the spot size on the sample increases with increasing angle α with respect to the surface normal. Due to the finite sample size of $(100\mu m)^2$, this effect limits the experimentally accessible angles to a maximum of about $|\alpha|=60°$. At $60°$, the Gaussian spot diameter increases from $60\,\mu m$ to $120\,\mu m$, but for the SHG, the relevant squared Gaussian profile ($120\,\mu m/\sqrt{2}\approx85\,\mu m$, as the $1/e$-diameter of the SHG electric field) is still smaller than the sample size. Hence, the neglected Gaussian tails of the SHG *intensity* profile can safely be ignored.

   Results regarding SHG are summarized in Fig. 9.11. Obviously, the data are quite complex and we are presently unable to explain them in detail. However, a few aspects are clear:

  (i) The SHG signal from the magnetic resonance [see Fig. 9.11(a)] yielding the $100\,\%$ signal at normal incidence, decreases with increasing angle $|\alpha|$, while the resonance can still be excited, as apparent from the linear transmittance spectra [see Fig. 9.10(a)]. In contrast, the SHG signals for the other two cases (b) and (c) increase with increasing angle $|\alpha|$ up to about $40°$ and decrease only for yet larger angles.

 (ii) The SHG signal from the magnetic resonance in Fig. 9.11(a) is, even for each angle, always larger than the SHG signals for the resonances (geometries) in (b) and (c).

(iii) We do observe significant differences between positive and negative angles for the SHG signals (Fig. 9.11) in some geometries, while for the corresponding linear transmittance spectra (Fig. 9.10) we do not. However, only small deviations appear for S-polarization, the largest deviations appear for P-polarization in Fig. 9.11(b). This can only be explained by a low symmetry of the corresponding SRR sample.

(iv) Beyond this, a detailed interpretation of the SHG signals from the cases in (b) and (c) is complicated by the fact that the resonance positions (see Fig. 9.10) shift and split with increasing angle $|\alpha|$ with respect to the fixed excitation wavelength.
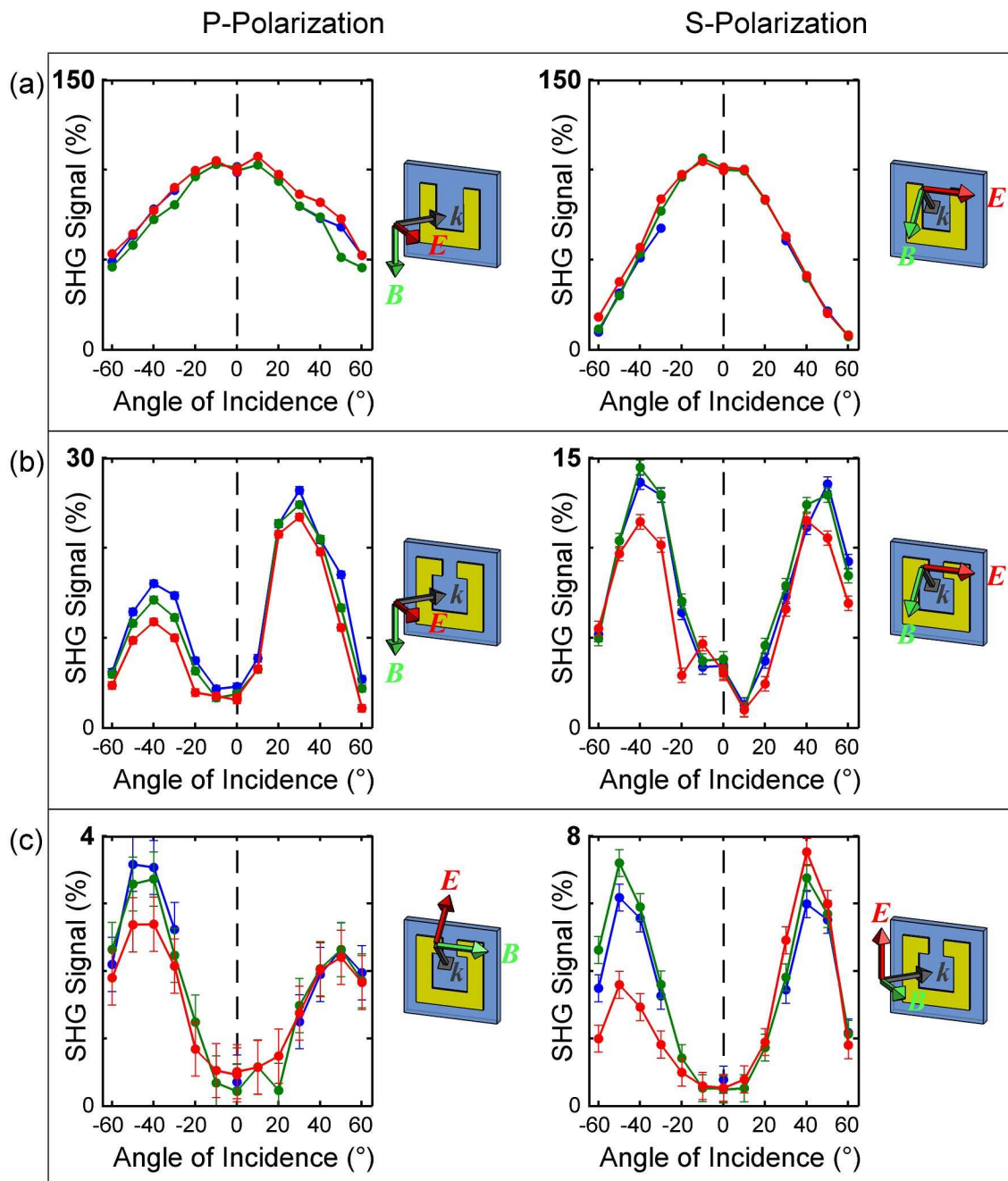
Figure 9.11: Measured SHG signal strengths resulting from oblique-incidence excitation, for the cases with a resonance near $1.5\,\mu m$ wavelength (cf. transmittance spectra in Fig. 9.10). The signal strength of the SHG transmitted through the Metamaterial and the substrate into the forward direction is shown for different angles of incidence. Signal strengths are normalized to $100\,\%$ for the magnetic resonance in (a) at normal incidence ($0°$). Note the different signal scales (bold numbers). The blue, green, and red curves show the SHG signal strengths obtained in three independent experimental runs, the error bars depict the noise level ($0.4\,\%$ here) of the lock-in signal read-out. The schemes adjacent to the spectra show the configuration of the incident fields for positive angles of incidence. Compare to the corresponding calculations (Fig. 8.9).

In general, the angle dependencies of the SHG experiments (Fig. 9.11) are only vaguely similar to our corresponding theory (Fig. 8.9). This means that at least one of our two assumptions for the theory, which is based on the magnetic part of the Lorentz force and the Driven-Dipole Approximation, becomes questionable for oblique incidence (whereas the normal-incidence data are well reproduced). Beyond this aspect, however, our angle-resolved SHG measurements again emphasize the outstanding role of the magnetic resonance in connection with the most dominant SHG signal strengths.

Chapter 10

Conclusions

In this thesis, we have investigated the nonlinear-optical properties of lithographically fabricated metallic nanostructures, in particular, of Metallic Photonic Crystal Slabs and planar photonic Metamaterials, in both experiment and theory. In either of the two materials, the electromagnetic field of a focussed laser light beam interacts significantly with the designed metallic nanostructures, and gives rise to Second-Harmonic Generation (SHG) and Third-Harmonic Generation (THG).

For all discussed experiments, corresponding high-quality samples with structured gold particles have been fabricated by standard electron-beam lithography in which a polymer mask with holes is created prior to the evaporation of gold. The deposition of metallic and dielectric thin films has been performed by electron-beam evaporation.

In a Metallic Photonic Crystal Slab (MPCS), the periodic arrangement of thin wires lying on top of a slab waveguide leads to the coupling of a photonic resonance with an electronic resonance. The photonic resonance arises because the lattice constant of the wires only allows light of a certain wavelength or frequency to be coupled to the waveguide mode. Hence, as usual for Photonic Crystals, the lattice constant must be on the order of the wavelength (about $1\,\mu m$ or less). The electronic resonance stems from the particle plasmon, a collective oscillation of the conduction electrons within each metallic nanostructure, driven by the light field and the restoring force of the surface charges appearing on the metal surface. In a MPCS, these two resonances are coupled due to the overlap of their field distributions. Thus, this system is an ideal candidate to study the strong coupling of two resonances by optical methods.

In order to interpret nonlinear-optical effects, the linear-optical properties of a system usually have to be understood first. For MPCSs, we have shown that the anti-crossing and the Fano lineshapes appearing in measured extinction (=absorption+scattering) spectra can very well be described by our model based on two coupled Lorentz oscillators. Our simple classical model even outperforms earlier models based on phenomenological parameters or a description inspired from quantum mechanics. Extending our model to nonlinear optics, we have identified the regime of "moderate coupling" in which corresponding THG spectra provide information on the underlying source of the optical nonlinearity. Furthermore, the nonlinear spectra calculated for excitation with two time-delayed pulses reveal a beating

in the spectral mixing products of the two peaks from linear optics, but not in the third harmonics of the latter peaks.

For corresponding experiments, we have used 5-femtosecond laser pulses from a titanium-sapphire oscillator and an interferometer to study the THG of our MPCS samples. Our experiments go beyond previous work regarding an improved temporal resolution and the fact that we spectrally resolve the interferometric third-harmonic signal. The spectra reveal a distinct behavior of the various spectral components versus time delay. Some spectral components exhibit a beating, others do not, as in our theory. Furthermore, the decay times of the envelopes strongly depend on the spectral component. The measured spectra agree qualitatively very well with the predictions of our simple theoretical model. The comparison has allowed us to identify the particle plasmon oscillation as the main source of nonlinearity.

In general, for metal nanoparticle ensembles, we have clarified a historical misunderstanding: We have shown analytically and numerically that the comparison of time-resolved femtosecond SHG or THG experiments in combination with extinction measurements does not allow one to distinguish between homogeneous and inhomogeneous contributions to the linewidth, in sharp contrast to the claim of previous work. We have unambiguously traced back this discrepancy to a technical mistake in that previous work. As a result, the plasmon decay time related to the homogeneous linewidth can not be determined from the comparison of linear-optical and SHG or THG data.

In the other part of our work, we investigate photonic Metamaterials which are also artificial optical materials, however, with responsive building blocks ("atoms") smaller than relevant wavelengths of light. A breakthrough in the young field of photonic Metamaterials has been the recent demonstration of materials with a magnetization oscillating at optical frequencies and even materials with a negative index of refraction. The most prominent "atom" appearing in this field is the Split-Ring Resonator (SRR), which can be considered in simplification as a small LC-resonance circuit with the ring forming a coil (with one winding) and the gap in the ring forming a capacitor. Incident light can excite oscillating currents flowing in this ring, corresponding to the fundamental LC mode, or higher modes. Particular modes of a SRR are known to possess oscillating magnetic dipole moments. Thus, Metamaterials are ideally suited for studies of materials (possibly) reacting to the magnetic field component of light.

This is especially interesting in nonlinear optics, in which the magnetic field can come into play by means of the magnetic part of the Lorentz force. When exciting SRRs with light, the local magnetic field near or in a SRR can point into a completely different direction compared to the magnetic field of the exciting wave. Hence, we have explained that SHG radiation, based on the magnetic part of the Lorentz force and detected in the forward direction, can be possible in Metamaterials. In contrast, this radiation is impossible for many natural materials because of the direction of this force. This new possibility has been the motivation for our nonlinear-optical investigations on Metamaterials.

Our experiments on SHG and THG are the first systematic study of the nonlinear optics of Metamaterials at all. Using 170-fs optical pulses from an optical parametric oscillator, we have compared nonlinear signals from planar arrays of different SRRs associated with different modes (resonances). These modes have been excited at the fixed wavelength of

1.5 μm with light at normal incidence onto the samples. We have obtained by far the strongest SHG and THG signals from those resonances associated with the strongest magnetic dipole moments. For small detuning from resonance (i.e., for a sample with parameters slightly different from those of a resonant sample) as well as for nonresonant excitation, the nonlinear signals decrease in strength as expected. Additionally, other photonic Metamaterials without magnetic dipole moments serving as resonant "control samples" have revealed no detectable SHG signal within the noise and a very low THG signal strength.

In order to shed more light onto the nature of the nonlinear signals observed for our Metamaterial samples with resonant SRRs, we have also performed SHG experiments at oblique incidence of the exciting light. We have obtained a complex behavior of the SHG signal strengths for increasing angle of incidence (with respect to the sample surface normal). The strongest signal is still obtained for the resonance with strongest magnetic dipole moment and normal incidence, but also the monotonically decreasing signal for this sample at increasing angle is larger than from the other investigated samples with weaker magnetic dipole moments. These samples, in turn, show a non-monotonic behavior for increasing angle of incidence. Small asymmetries of the SHG signal are observed with respect to tilting the sample in one or the opposite direction. These asymmetries must be attributed to small deviations from perfect mirror symmetry of our fabricated SRRs.

The linear-optical transmittance spectra of the SRR samples have been reproduced very well by corresponding numerical simulations. For these simulations, we have employed a commercial software package and have adapted it to the case of Metamaterials. A finite-element method is used to calculate the spatially resolved electromagnetic fields in and around the SRRs for linear optics. We have chosen the finite elements and have implemented the boundary conditions such that the simulation of normal-incidence and oblique-incidence scenarios has been made possible and simple.

Unfortunately, we are presently not in the position to compare the results of our nonlinear-optical experiments to a complete microscopic nonlinear theory for photonic Metamaterials. Under our conditions, quantum effects of metal electrons are not expected to be relevant. Thus, one can assume that a classical description of plasma nonlinearities is an adequate starting point: One has to solve self-consistently Newton's law for metal electrons with an electric and a magnetic component of the Lorentz force and the Maxwell equations for the metallic nanostructure. A corresponding theory has been formulated by the collaborating groups of S. W. Koch and J. V. Moloney, and has also been repeated in this thesis. The same groups also investigate corresponding numerical (finite-difference time-domain) simulations with Metamaterials consisting of SRRs, however, stability and convergence issues have not permitted final results so far. In this theory, the magnetic component of the Lorentz force is a term which appears in the volume of the metal. In contrast, SHG associated with the electric component of light is always exclusively from the metal surface, since the first-order charge density does not change in the volume of the metal. Especially the surface terms are critical in numerical evaluations.

Thus, we have developed an approximation for the above theory allowing for simple estimates. In our Driven-Dipole Approximation (DDA), the forces acting on the conduction electrons of each SRR are summed into a net force and the electrons are contracted into

a single mobile charge on which the net force is exerted. Using this approximation and assuming exclusively the magnetic part of the Lorentz force as the nonlinearity, we have been able to reuse numerical data from linear-optical simulations and have obtained results which are consistent with our experimental SHG data for normal incidence. However, this is no definite proof that these assumptions describe the dominating contribution. Hence, we have compared the additional experimental SHG data from our angle-resolved investigations with results derived from analog calculations for oblique SHG radiation. Here, the DDA leads to an ambiguity allowing for two differing results. However, neither of the two results completely matches the experiments, which allows to conclude that at least one of our two assumptions for the theory, which is based on the magnetic part of the Lorentz force and the DDA, becomes questionable for oblique incidence. Thus, especially more theoretical work in the field of nonlinear-optical Metamaterials will be necessary. The experimental data which we have presented here can provide a sensitive testground for such theories.

Broadly speaking, the spirit of the emerging field of photonic Metamaterials is to design and fabricate artificial tailored optical materials exhibiting linear- and/or nonlinear-optical properties that simply do not occur in natural substances. Regarding nonlinear optics, one obvious concrete goal is to increase effective nonlinear-optical coefficients by orders of magnitude. For very thin films, the magnetic-dipole Metamaterials which we have presented in this thesis already outperform standard SHG materials by several orders of magnitude with respect to conversion efficiency. Clearly, one of the future challenges is to extend this success to larger and especially to thicker Metamaterial structures in order to become meaningful for applications. Such three-dimensional (rather than planar) photonic Metamaterials are elusive to date, while first steps in this direction have been taken [139]. In that context, the problems of absorption and phase-matching would have to be solved.

Bibliography

[1] T. H. Maiman, *Stimulated optical radiation in ruby*, Nature **187**, 493 (1960).

[2] P. A. Franken, A. E. Hill, C. W. Peters, and G. Weinreich, *Generation of optical harmonics*, Phys. Rev. Lett. **7**, 118 (1961).

[3] N. Bloembergen, *Nonlinear optics* (Benjamin, New York, 1965).

[4] R. W. Boyd, *Nonlinear optics* (Academic Press, New York, 1992).

[5] Y. R. Shen, *The principles of nonlinear optics* (Wiley, New York, 1984).

[6] M. Wegener, *Extreme nonlinear optics* (Springer, Berlin, 2004).

[7] M. Scalora, J. P. Dowling, C. M. Bowden, and M. J. Bloemer, *Optical limiting and switching of ultrashort pulses in nonlinear photonic band gap materials*, Phys. Rev. Lett. **73**, 1368 (1994).

[8] National Research Council, *Harnessing light: Optical science and engineering for the 21ˢᵗ century* (National Academies Press, Washington, 1998).

[9] VDI-Technologiezentrum, Düsseldorf; gefördert vom Bundesministerium für Bildung und Forschung, *Deutsche Agenda – Optische Technologien für das 21. Jahrhundert* (WAZ-Druck, Duisburg, 2000).

[10] U. Kreibig and M. Vollmer, *Optical properties of metal clusters* (Springer, Berlin, 1995).

[11] E. Yablonovitch, *Inhibited spontaneous emission in solid-state physics and electronics*, Phys. Rev. Lett. **58**, 2059 (1987).

[12] S. John, *Strong localization of photons in certain disordered dielectric superlattices*, Phys. Rev. Lett. **58**, 2486 (1987).

[13] S. Linden, C. Enrich, G. Dolling, M. W. Klein, J. F. Zhou, T. Koschny, C. M. Soukoulis, S. Burger, F. Schmidt, and M. Wegener, *Photonic metamaterials: Magnetism at optical frequencies*, IEEE J. Sel. Top. Quant. **12**, 1097 (2006).

[14] S. Linden, C. Enrich, M. Wegener, J. F. Zhou, T. Koschny, and C. M. Soukoulis, *Magnetic response of metamaterials at 100 terahertz*, Science **306**, 1351 (2004).

[15] J. D. Jackson, *Classical electrodynamics,* 3rd edition (Wiley, New York, 1999).

[16] T. Tritschler, *Extreme nonlinear optics and carrier-envelope phase effects in semiconductors*, Ph.D. thesis, Universität Karlsruhe (TH) (2005).

[17] S.-Y. Chen, M. Maksimchuk, and D. Umstadter, *Experimental observation of relativistic nonlinear Thomson scattering*, Nature **396**, 653 (1998).

[18] P. B. Johnson and R. W. Christy, *Optical constants of the noble metals*, Phys. Rev. B **6**, 4370 (1972).

[19] N. W. Ashcroft and N. D. Mermin, *Solid state physics* (Saunders, New York, 1976).

[20] C. Kittel, *Introduction to solid state physics,* 7th edition (Wiley, New York, 1996).

[21] G. Mie, *Beiträge zur Optik trüber Medien, speziell kolloidaler Metallösungen.*, Ann. Phys. **25**, 377 (1908).

[22] C. Enkrich, *Magnetic metamaterials for photonics*, Ph.D. thesis, Universität Karlsruhe (TH) (2006).

[23] C. Sönnichsen, T. Franzl, T. Wilk, G. von Plessen, J. Feldmann, O. Wilson, and P. Mulvaney, *Drastic reduction of plasmon damping in gold nanorods*, Phys. Rev. Lett. **88**, 077402 (2002).

[24] B. Lamprecht, J. R. Krenn, A. Leitner, and F. R. Aussenegg, *Particle-plasmon decay-time determination by measuring the optical near-field's autocorrelation: Influence of inhomogeneous line broadening*, Appl. Phys. B **69**, 223 (1999).

[25] B. Lamprecht, G. Schider, R. T. Lechner, H. Ditlbacher, J. R. Krenn, A. Leitner, and F. R. Aussenegg, *Metal nanoparticle gratings: Influence of dipolar particle interaction on the plasmon resonance*, Phys. Rev. Lett. **84**, 4721 (2000).

[26] G. Schider, J. R. Krenn, A. Hohenau, H. Ditlbacher, A. Leitner, F. R. Aussenegg, W. L. Schaich, I. Puscasu, B. Monacelli, and G. Boreman, *Plasmon dispersion relation of Au and Ag nanowires*, Phys. Rev. B **68**, 155427 (2003).

[27] T. Vartanyan, M. Simon, and F. Träger, *Femtosecond optical second harmonic generation by metal clusters: The influence of inhomogeneous line broadening on the dephasing time of surface plasmon excitation*, Appl. Phys. B **68**, 425 (1999).

[28] F. Stietz, J. Bosbach, T. Wenzel, T. Vartanyan, A. Goldmann, and F. Träger, *Decay times of surface plasmon excitation in metal nanoparticles by persistent spectral hole burning*, Phys. Rev. Lett. **84**, 5644 (2000).

[29] M. J. Weida, S. Ogawa, H. Nagano, and H. Petek, *Ultrafast interferometric pumpprobe correlation measurements in systems with broadened bands or continua*, J. Opt. Soc. Am. B **17**, 1443 (2000).

[30] T. Zentgraf, A. Christ, J. Kuhl, and H. Giessen, *Tailoring the ultrafast dephasing of quasiparticles in metallic photonic crystals*, Phys. Rev. Lett. **93**, 243901 (2004).

[31] M. W. Klein, T. Tritschler, M. Wegener, and S. Linden, *Lineshape of harmonic generation by metallic nanoparticles and metallic photonic crystal slabs*, Phys. Rev. B **72**, 115113 (2005).

[32] P. Guyot-Sionnest, W. Chen, and Y. R. Shen, *General considerations on optical second-harmonic generation from surfaces and interfaces*, Phys. Rev. B **33**, 8254 (1986).

[33] F. Brown, R. E. Parks, and A. M. Sleeper, *Nonlinear optical reflection from a metallic boundary*, Phys. Rev. Lett. **14**, 1029 (1965).

[34] F. Brown and R. E. Parks, *Magnetic-dipole contribution to optical harmonics in silver*, Phys. Rev. Lett. **16**, 507 (1966).

[35] S. Janz and H. M. van Driel, *Second-harmonic generation from metal surfaces*, Int. J. Nonlin. Opt. Phys. **2**, 1 (1993).

[36] J. F. McGilp, *Second-harmonic generation at semiconductor and metal surfaces*, Surf. Rev. Lett. **6**, 529 (1999).

[37] S. S. Jha, *Nonlinear optical reflection from a metal surface*, Phys. Rev. Lett. **15**, 412 (1965).

[38] N. Bloembergen and Y. R. Shen, *Optical nonlinearities of a plasma*, Phys. Rev. **141**, 298 (1966).

[39] J. Rudnick and E. A. Stern, *Second-harmonic radiation from metal surfaces*, Phys. Rev. B **4**, 4274 (1971).

[40] A. Popa, M. F. Lazarescu, R. Dabu, and A. Stratan, *A model of the metallic surface-emitting second harmonic generator*, IEEE J. Quantum Electron. **33**, 1474 (1997).

[41] J. I. Dadap, J. Shan, and T. F. Heinz, *Theory of optical second-harmonic generation from a sphere of centrosymmetric material: small-particle limit*, J. Opt. Soc. Am. B **21**, 1328 (2004).

[42] J. D. Joannopoulos, R. D. Meade, and J. N. Winn, *Photonic crystals: Molding the flow of light* (Princeton University Press, Princeton, 1995).

[43] K. Sakoda, *Optical properties of photonic crystals*, Springer Series in Optical Sciences, vol. 80 (Springer, Berlin, 2005).

[44] K. Busch, S. Lölkes, R. B. Wehrspohn, and H. Föll (eds.), *Photonic Crystals: Advances in Design, Fabrication, and Characterization* (Wiley, Weinheim, 2004).

[45] K. Inoue and K. Ohtaka (eds.), *Photonic crystals: Physics, fabrication and applications*, Springer Series in Optical Sciences, vol. 94 (Springer, Berlin, 2004).

[46] J. D. Joannopoulos, P. R. Villeneuve, and S. Fan, *Photonic crystals: putting a new twist on light*, Nature **386**, 143 (1997).

[47] E. Hecht, *Optics,* 3rd edition (Addison-Wesley Longman, New York, 1998).

[48] M. Deubel, *Three-dimensional photonic crystals via direct laser writing: Fabrication and characterization*, Ph.D. thesis, Universität Karlsruhe (TH) (2006).

[49] D. C. Meisel, *Herstellung dreidimensionaler photonischer Kristalle mittels holographischer Lithographie und deren Charakterisierung*, Ph.D. thesis, Universität Karlsruhe (TH) (2006).

[50] K. Busch, G. von Freymann, S. Linden, L. Tkeshelashvili, S. Mingaleev, and M. Wegener, *Periodic nanostructures for photonics*, Phys. Rep. (2006).

[51] P. K. Tien, *Light waves in thin films and integrated optics*, Appl. Optics **10**, 2395 (1971).

[52] P. K. Tien, R. Ulrich, and R. J. Martin, *Modes of propagating light waves in thin deposited semiconductor films*, Appl. Phys. Lett. **14**, 291 (1969).

[53] R. E. Collin, *Field theory of guided waves* (McGraw-Hill, New York, 1960).

[54] M. L. Dakks, L. Kuhn, P. F. Heidrich, and B. A. Scott, *Grating coupler for efficient excitation of optical guided waves in thin films*, Appl. Phys. Lett. **16**, 523 (1970).

[55] H. Kogelnik and T. P. Sosnowski, *Holographic thin-film couplers*, Bell. Syst. Tech. J. **49**, 1602 (1970).

[56] M. Nevière, *Electromagnetic Theory of Gratings*, chapter 5 (Springer, Berlin, 1980), 123–157.

[57] H. Kogelnik and V. Ramaswamy, *Scaling rules for thin-film optical waveguides*, Appl. Optics **13**, 1857 (1974).

[58] S. Linden, J. Kuhl, and H. Giessen, *Controlling the interaction between light and gold nanoparticles: Selective suppression of extinction*, Phys. Rev. Lett. **86**, 4688 (2001).

[59] A. Christ, S. G. Tikhodeev, N. A. Gippius, J. Kuhl, and H. Giessen, *Waveguide-plasmon polaritons: Strong coupling of photonic and electronic resonances in a metallic photonic crystal slab*, Phys. Rev. Lett. **91**, 183901 (2003).

[60] S. Linden, *Kontrolle der Wechselwirkung zwischen Licht und Partikelplasmonen durch selektive Unterdrückung der Extinktion*, Ph.D. thesis, Universität Marburg (2001).

[61] A. Christ, *Optical properties of metallic photonic crystal structures*, Ph.D. thesis, Universität Marburg (2005).

[62] D. M. Whittaker and I. S. Culshaw, *Scattering-matrix treatment of patterned multilayer photonic structures*, Phys. Rev. B **60**, 2610 (1999).

[63] S. G. Tikhodeev, A. L. Yablonskii, E. A. Muljarov, N. A. Gippius, and T. Ishihara, *Quasiguided modes and optical properties of photonic crystal slabs*, Phys. Rev. B **66**, 045102 (2002).

[64] J. B. Pendry, A. J. Holden, D. J. Robbins, and W. J. Stewart, *Magnetism from conductors and enhanced nonlinear phenomena*, IEEE Trans. Microw. Theory Tech. **47**, 2075 (1999).

[65] N. Feth, *Herstellung metallischer Metamaterialien mittels holographischer Laserlithographie und deren Charakterisierung*, Master's thesis, Universität Karlsruhe (TH) (2006).

[66] G. Dolling, *Herstellung und Charakterisierung von magnetodielektrischen Metamaterialien*, Master's thesis, Universität Karlsruhe (TH) (2006).

[67] V. G. Veselago, *The electrodynamics of substances with simultaneously negative values of ϵ and μ*, Sov. Phys. Usp. **10**, 509 (1968).

[68] R. A. Shelby, D. R. Smith, and S. Schultz, *Experimental verification of a negative index of refraction*, Science **292**, 77 (2001).

[69] J. B. Pendry, *Negative refraction makes a perfect lens*, Phys. Rev. Lett. **85**, 3966 (2000).

[70] N. Fang, H. Lee, C. Sun, and X. Zhang, *Sub–diffraction-limited optical imaging with a silver superlens*, Science **308**, 534 (2005).

[71] J. B. Pendry, D. Schurig, and D. R. Smith, *Controlling electromagnetic fields*, Science **312**, 1780 (2006).

[72] D. Schurig, J. J. Mock, B. J. Justice, S. A. Cummer, J. B. Pendry, A. F. Starr, and D. R. Smith, *Metamaterial electromagnetic cloak at microwave frequencies*, Science **314**, 977 (2006).

[73] U. Leonhardt, *Optical conformal mapping*, Science **312**, 1777 (2006).

[74] M. W. Klein, C. Enkrich, M. Wegener, and S. Linden, *Second-harmonic generation from magnetic metamaterials*, Science **313**, 502 (2006).

[75] A. A. Zharov, I. V. Shadrivov, and Y. S. Kivshar, *Nonlinear properties of left-handed metamaterials*, Phys. Rev. Lett. **91**, 037401 (2003).

[76] N. A. Zharova, I. V. Shadrivov, A. A. Zharov, and Y. S. Kivshar, *Nonlinear transmission and spatiotemporal solitons in metamaterials with negative refraction*, Opt. Ex. **13**, 1291 (2005).

[77] A. K. Popov and V. M. Shalaev, *Negative-index metamaterials: Second-harmonic generation, Manley-Rowe relations and parametric amplification*, Appl. Phys. B **84**, 131 (2006).

[78] H. J. Schneider and P. Dullenkopf, *Slotted tube resonator: A new NMR probe head at high observing frequencies*, Rev. Sci. Instrum. **48**, 68 (1977).

[79] W. N. Hardy and L. A. Whitehead, *Split-ring resonator for use in magnetic resonance from 200-2000 MHz*, Rev. Sci. Instrum. **52**, 213 (1981).

[80] B. T. Ghim, G. A. Rinard, W. Quine, S. S. Eaton, and G. R. Eaton, *Design and fabrication of copper-film loop–gap resonators*, J. of Magn. Res. A **120**, 72 (1996).

[81] S. O'Brien and J. B. Pendry, *Magnetic activity at infrared frequencies in structured metallic photonic crystals*, J. Phys.: Condens. Matter **14**, 6383 (2002).

[82] S. O'Brien, D. McPeake, S. A. Ramakrishna, and J. B. Pendry, *Near-infrared photonic band gaps and nonlinear effects in negative magnetic metamaterials*, Phys. Rev. B **69**, 241101 (2004).

[83] J. F. Zhou, Th. Koschny, M. Kafesaki, E. N. Economou, J. B. Pendry, and C. M. Soukoulis, *Saturation of the magnetic response of split-ring resonators at optical frequencies*, Phys. Rev. Lett. **95**, 223902 (2005).

[84] A. Ishikawa, T. Tanaka, and S. Kawata, *Negative magnetic permeability in the visible light region*, Phys. Rev. Lett. **95**, 237401 (2005).

[85] M. W. Klein, C. Enrich, M. Wegener, C. M. Soukoulis, and S. Linden, *Single-slit split-ring resonators at optical frequencies: Limits of size scaling*, Opt. Lett. **31**, 1259 (2006).

[86] T. J. Yen, W. J. Padilla, N. Fang, D. C. Vier, D. R. Smith, J. B. Pendry, D. N. Basov, and X. Zhang, *Terahertz magnetic response from artificial materials*, Science **303**, 1494 (2004).

[87] N. Katsarakis, G. Konstantinidis, R. S. Penciu A. Kostopoulos and, T. F. Gundogdu, M. Kafesaki, E. N. Economou, T. Koschny, and C. M. Soukoulis, *Magnetic response of split-ring resonators in the far-infrared frequency regime*, Opt. Lett. **30**, 1348 (2005).

[88] C. Enrich, F. Pérez-Willard, D. Gerthsen, J. F. Zhou, C. M. Soukoulis, M. Wegener, and S. Linden, *Focused-ion-beam nanofabrication of near-infrared magnetic metamaterials*, Adv. Mater. **17**, 2547 (2005).

[89] C. Enrich, M. Wegener, S. Linden, S. Burger, L. Zschiedrich, F. Schmidt, J. F. Zhou, T. Koschny, and C. M. Soukoulis, *Magnetic metamaterials at telecommunication and visible frequencies*, Phys. Rev. Lett. **95**, 203901 (2005).

[90] H. G. Craighead and G. A. Niklasson, *Characterization and optical properties of arrays of small gold particles*, Appl. Phys. Lett. **44**, 1134 (1984).

[91] B. Lamprecht, J. R. Krenn, A. Leitner, and F. R. Aussenegg, *Femtosecond decay-time measurement of electron-plasma oscillation in nanolithographically designed silver particles*, Appl. Phys. B **64**, 269 (1997).

[92] C. Becker, *Experimente zur nichtlinearen Optik photonischer Kristalle*, Ph.D. thesis, Universität Karlsruhe (TH) (2006).

[93] B. Bhushan (ed.), *Springer handbook of nanotechnology* (Springer, Berlin, 2004).

[94] Z. L. Wang, Y. Liu, and Z. Zhang (eds.), *Handbook of nanophase and nanostructured materials* (Kluwer Academic/Plenum Publishers, New York, 2003).

[95] S. Zhang, W. Fan, B. K. Minhas, A. Frauenglass, K. J. Malloy, and S. R. J. Brueck, *Midinfrared resonant magnetic nanostructures exhibiting a negative permeability*, Phys. Rev. Lett. **94**, 037402 (2005).

[96] G. R. Brewer, *Electron-beam technology in microelectronic fabrication* (Academic Press, New York, 1980).

[97] A. E. Siegman, *Lasers* (University Science Books, Mill Valley, 1986).

[98] O. D. Mücke, *Extreme nonlinear optics in semiconductors with intense few-cycle laser pulses*, Ph.D. thesis, Universität Karlsruhe (TH) (2003).

[99] P. P. Silvester and R. L. Ferrari, *Finite elements for electrical engineers* (Cambridge University Press, Cambridge, 1996).

[100] J. Jin, *The finite element method in electromagnetics* (Wiley, New York, 2002).

[101] P. Monk, *Finite element methods for Maxwell's equations* (Oxford Science Publications, Oxford, 2003).

[102] R. Courant, *Variational methods for the solution of problems of equilibrium and vibrations*, Bull. Amer. Math. Soc. **49**, 1 (1943).

[103] M. J. Turner, R. W. Clough, H. C. Martin, and L. J. Topp, *Stiffness and deflection analysis of complex structures*, J. Aer. Sci. **23**, 805 (1956).

[104] FEMLAB documentation is provided with the software, (2006).

[105] K. S. Yee, *Numerical solution of initial boundary value problems involving Maxwell's equations in isotropic media*, IEEE Trans. Antennas Propag. **14**, 302 (1966).

[106] A. Taflove and S. C. Hagness, *Computational electrodynamics: The finite-difference time-domain method* (Artech House, Norwood, 2005).

[107] H. Whitney, *Geometric integration theory* (Princeton University Press, Princeton, 1957).

[108] J. C. Nédélec, *Mixed finite elements in* $\mathbb{R}^3$, Numer. Math. **35**, 315 (1980).

[109] J. C. Nédélec, *A new family of mixed finite elements in* $\mathbb{R}^3$, Numer. Math. **50**, 57 (1986).

[110] P. D. Ledger and K. Morgan, *The application of the hp–finite element method to electromagnetic problems*, Arch. of Computat. Meth. Eng. **12**, 235 (2005).

[111] S. Burger, L. Zschiedrich, R. Klose, A. Schädle, F. Schmidt, C. Enkrich, S. Linden, M. Wegener, and C. M. Soukoulis, *Numerical Investigation of Light Scattering off Split-Ring Resonators*, Proc. SPIE Int. Soc. Opt. Eng. **5955**, 595503 (2005).

[112] L. Zschiedrich, S. Burger, B. Kettner, and F. Schmidt, *Advanced finite element method for nano-resonators*, available at http://arxiv.org/abs/physics/0601025 (2006).

[113] J.-P. Bérenger, *A perfectly matched layer for the absorption of electromagnetic waves*, J. Comput. Phys. **114**, 185 (1994).

[114] Z. S. Sacks, D. M. Kingsland, R. Lee, and J.-F. Lee, *A perfectly matched anisotropic absorber for use as an absorbing boundary condition*, IEEE Trans. Antennas Propagat. **43**, 1460 (1995).

[115] W. C. Chew and W. H. Weedon, *A 3D perfectly matched medium from modified Maxwell's equations with stretched coordinates*, Microwave Opt. Technol. Lett. **7**, 599 (1994).

[116] W. Gotschy, K. Vonmetz, A. Leitner, and F. R. Aussenegg, *Thin films by regular patterns of metal nanoparticles: Tailoring the optical properties by nanodesign*, Appl. Phys. B **63**, 381 (1996).

[117] J.-H. Klein-Wiele, P. Simon, and H.-G. Rubahn, *Size-dependent plasmon lifetimes and electron-phonon coupling time constants for surface-bound Na clusters*, Phys. Rev. Lett. **80**, 45 (1998).

[118] T. Klar, M. Perner, S. Grosse, G. von Plessen, W. Spirkl, and J. Feldmann, *Surface-plasmon resonances in single metallic nanoparticles*, Phys. Rev. Lett. **80**, 4249 (1998).

[119] V. Halté, J.-Y. Bigot, B. Palpant, M. Broyer, B. Prével, and A. Pérez, *Size dependence of the energy relaxation in silver nanoparticles embedded in dielectric matrices*, Appl. Phys. Lett. **75**, 3799 (1999).

[120] H. Ditlbacher, J. R. Krenn, B. Lamprecht, A. Leitner, and F. R. Aussenegg, *Spectrally coded optical data storage by metal nanoparticles*, Opt. Lett. **25**, 563 (2000).

[121] B. K. Canfield, S. Kujala, K. Laiho, K. Jefimovs, J. Turunen, and M. Kauranen, *Chirality arising from small defects in gold nanoparticle arrays*, Opt. Ex. **14**, 950 (2006).

[122] M. Volmer and A. Weber, *Keimbildung in übersättigten Gebilden*, Z. Phys. Chem. (Leipzig) **119**, 277 (1926).

[123] B. Lamprecht, J. R. Krenn, A. Leitner, and F. R. Aussenegg, *Resonant and off-resonant light-driven plasmons in metal nanoparticles studied by femtosecond-resolution third-harmonic generation*, Phys. Rev. Lett. **83**, 4421 (1999).

[124] J.-C. Diels and W. Rudolph, *Ultrashort laser pulse phenomena,* Chap. 8 (Academic Press, London, 1996).

[125] M. Wegener, D. S. Chemla, S. Schmitt–Rink, and W. Schäfer, *Line shape of time-resolved four-wave mixing*, Phys. Rev. A **42**, 5675 (1990).

[126] MATLAB documentation is provided with the software or available online, *http://www.mathworks.com/access/helpdesk/help/techdoc/* (2006).

[127] A. Sharon, D. Rosenblatt, and A. A. Friesem, *Resonant grating–waveguide structures for visible and near-infrared radiation*, J. Opt. Soc. Am. A **14**, 2985 (1997).

[128] U. Fano, *Effects of configuration interaction on intensities and phase shifts*, Phys. Rev. **124**, 1866 (1961).

[129] H. Giessen, S. Linden, A. Christ, J. Kuhl, D. Nau, T. Meier, P. Thomas, and S. W. Koch, *Fano resonances in metallic photonic crystals*, International Quantum Electronics Conference (IQEC), IFC5, San Francisco (U.S.A.) (May 16-21, 2004).

[130] A. Christ, T. Zentgraf, J. Kuhl, S. G. Tikhodeev, N. A. Gippius, and H. Giessen, *Optical properties of planar metallic photonic crystal structures: Experiment and theory*, Phys. Rev. B **70**, 125113 (2004).

[131] A. K. Popov, V. V. Slabko, and V. M. Shalaev, *Second harmonic generation in left-handed metamaterials*, Laser Phys. Lett. **3**, 293 (2006).

[132] A. K. Popov and V. M. Shalaev, *Compensating losses in negative-index metamaterials by optical parametric amplification*, Opt. Lett. **31**, 2169 (2006).

[133] M. V. Gorkunov, I. V. Shadrivov, and Y. S. Kivshar, *Enhanced parametric processes in binary metamaterials*, Appl. Phys. Lett. **88**, 71912 (2006).

[134] A. A. Zharov, N. A. Zharova, I. V. Shadrivov, and Y. S. Kivshar, *Subwavelength imaging with opaque nonlinear left-handed lenses*, Appl. Phys. Lett. **87**, 91104 (2005).

[135] W. Hoyer, T. Stroucken, T. Meier, and S. W. Koch, private communication (2005-2007).

[136] J. Förstner and J. V. Moloney, private communication (2005-2007).

[137] T. J. M. Boyd and J. J. Sanderson, *The physics of plasmas* (Cambridge University Press, Cambridge, 2003).

[138] N. Bloembergen and P. S. Pershan, *Light waves at the boundary of nonlinear media*, Phys. Rev. **128**, 606 (1962).

[139] G. Dolling, M. Wegener, and S. Linden, *Realization of a three-functional-layer negative-index photonic metamaterial*, Opt. Lett. **32**, in press (2007).

Acknowledgements